National Technical University of Athens
School of Mechanical Engineering
Fluids Section
Lab. of Thermal Turbomachines
Parallel CFD & Optimization Unit

Parametric Effectiveness and its Role in Aerodynamic Shape Optimization

Diploma Thesis
by
Kleanthis Kleanthous

Supervisor: Kyriakos C. Giannakoglou, Professor
NTUA

Athens, February 2023

Acknowledgements

Regarding the completion of this thesis, I would like to express my gratitude to my professor Dr. K.C.Giannakoglou for giving me the opportunity to work in a very interesting subject. Also, the time he spend for my guidance, his corrections and his advises have been significantly important for me.

Moreover, I would like to express my sincere thanks to Dr. E.M.Papoutsis-Kiachagias for his technical advises and the knowledge he provided. Without his valuable support, the completion of this dissertation would have been impossible.

Last but not least, I would like to thank my family and all people stood by my side through the entire duration of my studies. My deepest gratitude goes to my parents, without their sacrifices and support the dream to follow Mechanical Engineering studies could not be possible. I would also like to express my thanks to all my close friends for their encouragement and company during the entire duration of my academic path, having a particular impact on my journey. Finally a big thanks goes to M. for her unlimited support and patience which had been a huge influence on me and a part of my success.

National Technical University of Athens
School of Mechanical Engineering
Fluids Section
Lab. of Thermal Turbomachines
Parallel CFD & Optimization Unit

Parametric Effectiveness and its Role in Aerodynamic Shape Optimization

Diploma Thesis
by
Kleanthis Kleanthous

Supervisor: Kyriakos C. Giannakoglou, Professor NTUA

Abstract

Gradient-based optimization using CAD-based parameterizations is widely used in shape optimization in internal and external aerodynamics, where the CAD-models parameters are used as design variables. Parametric Effectiveness is introduced as a quantity used to compare the CAD-based parameterization's optimization potential to the potential of an optimization in which all surface nodes are allowed to move and which corresponds to the maximum possible flexibility.

The purpose of this diploma thesis is the formulation and development of the Parametric Effectiveness, the investigation of its behaviour when different parameterizations are used and its association with shape optimization results. This is done by using three applications, an isolated airfoil, an S-bend duct and a 2D compressor cascade. Firstly, the Parametric Effectiveness behaviour is investigated through parametric studies which involve different parameterizations and parameterization methods such as NURBS Bezier-Bernstein and volumetric B-splines. Furthermore, its association with the optimization results as well as its evolution during the optimization procedure are evaluated. The Individual Parametric Effectiveness of each design variable is also computed and involved in the design variable's selection, the results of which are also examined through certain optimization runs. In this thesis, the gradient of any objective function is computed using the continuous adjoint method in OpenFOAM as developed by the Parallel CFD & Optimization Unit (PCOpt) of NTUA.

Εθνικό Μετσόβιο Πολυτεχνείο
Σχολή Μηχανολόγων Μηχανικών
Τομέας Ρευστών
Εργαστήριο Θερμικών Στροβιλομηχανών
Μονάδα Παράλληλης Υπολογιστικής Ρευστοδυναμικής & Βελτιστοποίησης

Η Παραμετρική Αποδοτικότητα και ο Ρόλος της στην Αεροδυναμική Βελτιστοποίηση Μορφής

Διπλωματική εργασία
Κλεάνθης Κλεάνθους

Επιβλέπων: Κυριάκος Χ. Γιαννάκογλου, Καθηγητής ΕΜΠ

Περίληψη

Οι αιτιοκρατικές μέθοδοι βελτιστοποίησης, με τη χρήση μοντέλων CAD, οι παράμετροι των οποίων αποτελούν τις μεταβλητές σχεδιασμού, βρίσκουν μεγάλη εφαρμογή στα προβλήματα βελτιστοποίησης μορφής, τόσο στην εξωτερική όσο και στην εσωτερική αεροδυναμική. Για την υποστήριξη τους, εισάγεται η έννοια της Παραμετρικής Αποτελεσματικότητας για την αξιολόγηση της δυναμικής των μοντέλων CAD στην βελτιστοποίηση, σε σύγκριση με αυτήν της ελεύθερης μετακίνησης κόμβων, η οποία μπορεί να επιτύχει το καλύτερο δυνατό αποτελέσμα.

Σκοπός της διπλωματικής εργασίας είναι η διατύπωση και ανάπτυξη της μεθόδου υπολογισμού της Παραμετρικής Αποτελεσματικότητας, η διερεύνηση της συμπεριφοράς της σε διάφορες παραμετροποιήσεις καθώς και η συσχέτιση της με τα αποτελέσματα της βελτιστοποίησης, μέσω τριών εφαρμογών: μίας μεμονωμένης αεροτομής ενός αγωγού με διαμόρφωση τύπου S και μιας 2Δ πτερύγωσης συμπιεστή. Η συμπεριφορά της εξετάζεται αρχικά μέσω παραμετρικών μελετών με τη χρήση διαφορετικών παραμετροποιήσεων αλλά και μεθόδων παραμετροποίησης όπως, καμπύλες NURBS & Bezier-Bernstein, και volumetric B-splines. Επιπλέον, μελετάται η συσχέτιση των τιμών της με τα αποτελέσματα της βελτιστοποίησης βάσηει των συμπερασμάτων της προηγούμενης μελέτης. Ταυτόχρονα, υπολογίζεται η Παραμετρική Αποτελεσματικότητα για κάθε μεταβλητή σχεδιασμού και διερευνάται η συνεισφορά της στην επιλογή των μεταβλητών σχεδιασμού, η οποία επικυρώνεται μέσω των αποτελεσμάτων της βελτιστοποίησης. Τέλος, για τη βελτιστοποίηση χρησιμοποιείται η συνεχής συζυγής μέθοδος όπως έχει αναπτυχθεί από την Μονάδα Παράλληλης Ρευστοδυναμικής και Βελτιστοποίσης (ΜΠΥΡ & Β) του ΕΜΠ.

Acronyms

CFD	Computational Fluid Dynamics
SOO	Single Objective Optimization
MOO	Multi Objective Optimization
RANS	Reynolds Averaged Navier Stokes
BC	Boundary Conditions
FAE	Field Adjoint Equations
ABC	Adjoint Boundary Conditions
NTUA	National Technical University of Athens
PCOpt	Parallel CFD & Optimization Unit
PE	Parametric Effectiveness
IPE	Individual Parametric Effectiveness
CP	Control Points
CAD	Computer Aided Design
NURBS	Non-Uniform Rational Basis Spline
PDE	Partial Differential Equation
EA	Evolutionary Algorithms
ΕΜΠ	Εθνικό Μετσόβιο Πολυτεχνείο
ΕΘΣ	Εργαστήριο Θερμικών Στροβιλομηχανών
ΜΠΥΡ&Β	Μονάδα Παράλληλης Υπολογιστικής Ρευστοδυναμικής & Βελτιστοποίησης
ΥΡΔ	Υπολογιστική Ρευστοδυναμική

Contents

Chapter 1

Introduction

The evolution of computers and the enhancement of their computational power have increased the involvement of CAD models, CFD and optimization methods in aerodynamic shape design. Particularly, the integration of CFD algorithms in the design procedure provides a relatively fast and suitable frame for the aerodynamic performance evaluation, by reducing the use of expensive and time-consuming experimental methods. Therefore, it contributed in the development of various optimization methods and their integration in the design process of aerodynamic shapes.

1.1 Shape Optimization

Shape optimization in aerodynamics aims at increasing the aerodynamic performance of a certain application's shape heading gradually to the optimum (or improved) shape. In general, optimization problems can be found as maximization or minimization problems. Without loss in generality, in this diploma thesis, all optimization problems will be cast in the form of minimizing the cost function.

Optimization methods can be categorized by the number of objectives or by the mathematical approach of the problem([1]). Firstly, they can be classified to SOO (Single-Objective Optimization) or MOO (Multi-Objective Optimization) problems. The first category uses a single objective function to formulate the aerodynamic performance, whereas the second one combines two or more objective functions. The second classification refers to the mathematical formulation. The two general optimization categories are classified as, stochastic and deterministic. The first category evaluates the aerodynamic performance of multiple geometries, generated by different design variables combinations. The optimized shapes are achieved through a targeted exploration of different parameters heading to the total minimum. The deterministic or gradient-based optimization methods are based in the differentiation of the objective function w.r.t. to the parameters defining the shape, so that the sensitivity derivatives are extracted in order to update the design variables and gradually reaching a local or a total minimum.

The interest of this thesis, is in the gradient-based optimization of SOO minimization applications. More particular, the adjoint optimization method([1]) is used to compute sensitivity derivatives. In order to proceed in an optimization loop, the geometry must be expressed using parameters that define its shape, which can be even the discretized surface's boundary coordinates. More details are provided in the next sections of this chapter.

1.2 CAD Models in Shape Optimization

Nowadays, optimization methods are part of any design process. Prior to any implementation of the optimization algorithms, the initial geometry is designed or/and parameterized using CAD models, the parameters of which are used as the design variables ($\vec{b} \in \mathbb{R}^n$). However in some cases, the boundary nodes of the geometry are used as the problem's design variables. The main advantage of utilizing CAD parameterizations, compared to the free-moving of the shape's boundary, is the manufacturability of the model.

1.3 Shape Parameterization Methods

The shape parameterization methods that are used in this diploma thesis, are NURBS curves, Bezier-Bernstein curves and volumetric B-splines. The first two methods parameterize the contours of the geometries, where their parameters (CPs) define the shape of each geometry through the optimization loop. However, volumetric B-splines parameterize, not only the contour of the geometry, but also the case's internal grid. Moreover, an advantage of shape parameterization is the fact that they produce (by definition) smooth shapes during the whole optimization process, unlike the free-moving approach which requires surface smoothing algorithms.

However, the formulation of those shape parameterizations, impose a limitation in the complexity of the generated shapes due to their formulation, which limits their optimization potential. For that reason Parametric Effectiveness (PE) is introduced in order to evaluate the optimization potential of a shape parameterization. Specifically, PE compares the performance gains of using a shape parameterization with the maximum performance gain that can be achieved when the boundary's nodes are free to move one by one.

1.4 Purpose of This Thesis

Firstly, this thesis aims to provide a formulation of the PE metric in gradient based optimization. Using the same formulation, the Individual Parametric Effectiveness value is also introduced as a measure to identify the importance of each parameter in the optimization.

PE is programmed and tested using three applications of 2D internal and external aerodynamics, an isolated airfoil, an S-bend duct and a compressor stator's cascade([2]). The PE behaviour is investigated through various studies for different shape parameterizations and parameterization methods. Also, it aims to study the correlation of PE values and the optimization results of the three applications by utilizing different shape parameterizations. In addition, PE values are also computed for different cycles of the optimization loop in order to investigate its evolution.

The contribution of the IPE in selecting the most effective parameters as design variables is also tested, by performing optimization loops with selected design variables based on the computed IPE values of certain cases.

1.5 Literature Survey - Previous Works

The work of this thesis was inspired by the works of [3] and [4]. The motivation of [3] was to introduce a method that rates the CAD parameterization of a model in terms of its optimization potential. It provides the definition and a formulation of the PE, as a measure to rate the quality of the CAD models parameters as the design variables of the adjoint optimization procedure. [3] suggests that PE can be used to select the design variables from a given CAD model, by evaluating the PE of different parameters sets as design variables. However, the selection of design variables is based on engineering judgement, which requires a considerable amount of time and experience. Finally, the computation of PE is demonstrated using different applications of structural mechanics and aerodynamics.

Furthermore, [4] adopted the same approach for PE computation, and its work is based on the findings of [3]. Specifically, [4] introduces an automated approach in selecting the parameters of a CAD model with the highest PE, which is the main focus of this work. The ultimate objective is the reduction of time needed for the update of design variables of the CAD model, which is claimed by [4] that in complex applications it can be the same or even more than the primal and adjoint fields due to the available equipment and software of an industrial environment. The suggested method is studied and demonstrated in 3D applications in internal and external aerodynamics where the computational cost of the parameters update is significant.

Both papers utilize the same formulation for PE. The performance gains of the CAD parameterization and the free-moving of the boundary are computed using the sensitivity derivatives computed on every node of the surface, where the gains of CAD sensitivity derivatives are computed based on steepest descent. The formulation of PE, aims in favoring the parameters that impact the regions of higher sensitivity regardless of the area that they affect. The latter is achieved by introducing a fair comparison condition for the evaluation of different parameterizations, where, the gains of both (CAD and free-move) are normalized with a predefined small number of total deformation, by setting the root mean square of the total boundary deformation (V) equal to that value(dv). As a result, the normalized gains of both CAD and free-move favor the CAD parameterizations (or sets of parameters of a given CAD model), that affect the areas of higher sensitivities, regardless of the amount of area they may displace.

The computation of the performance gains for CAD parameterization or free-move, require the computation of the boundary displacement due to every parameter change. Practically, this measure is the geometric derivatives of CAD parameters which, in these papers are computed through finite differences by perturbing each parameter by ϵ and compute the displacement of all the surface's nodes for each parameters perturbation.

In this diploma thesis, a different approach is proposed for the computation of the PE. The formulation of the performance gains of CAD parameterization and the free-move (nodal parameterization), are both based on the steepest descent method. Also, the fair comparison condition is implemented to compare the CAD and the nodal parameterizations, rather than the comparison between different CAD parameterizations. Specifically, the fair comparison condition aims at a correlation between the steepest descent steps (η) of CAD parameterization and the boundary's free-move. In addition, the boundary displacement due to change in the parameter's value i.e. the geometric derivatives, are computed through the differentiation of the CAD parameterizations mathematical expressions, which is significantly faster.

Finally, the expression of PE as used in this thesis, does not favour the deformation of the areas of high sensitivities. In fact, PE focuses on the total improvement in performance, even if the latter may be achieved by large deformation of areas with lower sensitives.

1.6 Thesis Layout

The thesis structure and layout is briefly presented as follows:

- **Chapter 2:** The primal and adjoint problems are presented and explained, along with their boundary conditions, for the sensitivity derivatives computation. The optimization algorithm is presented as well.
- **Chapter 3:** The definition of PE is given. Also, an extensive presentation and elaboration regarding the PE theory and formulation are presented.
- **Chapter 4:** In this chapter, the behaviour of PE is investigated through parametric studies, where PE is computed w.r.t. the number of CPs for different parameterizations and parameterization methods. Also the definition and formulation of IPE is presented for the quantification of the design variable's impact in the optimization. For the PE behaviour study, three different applications are used, an isolated airfoil, ans S-bend type duct and a compressor cascade (all applications are 2D), the objective functions of which are given and explained.
- **Chapter 5:** In this chapter, PE is studied through the performance of various optimization loops based on the previous chapter's results. The PE results are associated and compared to the optimization results, for the PE validation.
- **Chapter 6:** The Summary and conclusions are presented, along with a suggestions for future work.

Chapter 2

Primal and Adjoint Problems

2.1 Primal Problem

All the applications of this thesis are dealing with 2D steady state incompressible flows. The state equations of the primal problem are the RANS equations ([5], [6], [7]). All equations of the primal problem are given in the form of residuals.

The Navier-Stokes equations govern steady or unsteady, turbulent or laminar viscous flows, in differential form. They are used to simulate the flow of an aerodynamic problem, by computing the flow fields inside a control volume. The equations are solved with the SIMPLE algorithm([8]), using finite volumes([9]) of the OpenFOAM([10],[11])software.

2.1.1 The RANS Equations

The RANS equations, is an alternative formulation of the Navier Stokes equations, proposed by Reynolds to include the effects of turbulence, using the Boussinesq hypothesis([5]) in order to avoid the utilization of DNS (Direct Numerical Simulation) which requires very dense grids and extensive amount of computational power. The final form of the primal equations ([7]), are presented as:

The mass conservation equation, a.k.a the continuity equation, is given as:

$$R^p = -\frac{\partial v_j}{\partial x_j} = 0 \tag{2.1}$$

The momentum conservation equation is given as:

$$R_i^v = v_j \frac{\partial v_i}{\partial x_j} - \frac{\partial}{\partial x_j}\left[(\nu + \nu_t)\left(\frac{\partial v_i}{\partial x_j} + \frac{\partial v_j}{\partial x_i}\right)\right] + \frac{\partial p}{\partial x_i} = 0, \quad i = 1, 2(, 3) \quad (2.2)$$

where:

v_i are the mean velocity components,

p is the mean pressure,

ν is the fluid's kinematic viscosity,

ν_t is the turbulent viscosity (eddy viscosity).

$\tilde{\nu}$ is the turbulence model's variable

The turbulence viscosity field is computed using the so called turbulence models. Turbulence models are classified into three categories. The Algebraic models, which are the most primitive models, utilizing only algebraic equations for ν_t computation, the first order models, where ν_t field is computed by solving one PDE and the Second order models, solving two PDE. In this thesis, the first order low-Re Spalart-Allmaras model is used in cases where turbulence is applied.

2.1.2 Spalart-Allmaras turbulence model

Spalart-Allmaras is a first order turbulence model used to compute the ν_t. However the turbulent viscosity in this model is not directly computed by solving the PDE equation. A new variable $\tilde{\nu}$ is introduced, which is considered to be the turbulence model's variable. The model's PDE ([7],[12]) is written as:

$$R^{\tilde{\nu}} = v_j \frac{\partial \tilde{\nu}}{\partial x_j} - \frac{\partial}{\partial x_j}\left[\left(\nu + \frac{\tilde{\nu}}{\sigma}\right)\frac{\partial \tilde{\nu}}{\partial x_j}\right] - \frac{C_{b_2}}{\sigma}\left(\frac{\partial \tilde{\nu}}{\partial x_j}\right)^2 - \tilde{\nu}P(\tilde{\nu}) + \tilde{\nu}D(\tilde{\nu}) = 0 \quad (2.3)$$

Where ν_t is expressed as a function of $\tilde{\nu}$ as follows:

$$\nu_t = \tilde{\nu} f_{v1} \quad (2.4)$$

The production and dissipation terms are given by:

$$P(\tilde{\nu}) = C_{b1}\tilde{Y}, \quad D(\tilde{\nu}) = C_{w1} f_w(\tilde{Y}) \frac{\tilde{\nu}}{\Delta^2} \quad (2.5)$$

Term Y is derived from:

$$\tilde{Y} = Y f_{v3} + \frac{\tilde{\nu}}{\Delta^2 \kappa^2} f_{v2}, \quad Y = \left| e_{ijk} \frac{\partial v_k}{\partial x_j} \right| \tag{2.6}$$

where, Y is the vorticity magnitude and Δ is the distance of cell centres (cell centred-finite volume scheme is employed) from the wall. The model functions are written as:

$$f_{v1} = \frac{X^3}{X^3 + C_{v1}^3}, \quad f_{v2} = \frac{1}{\left(1 + \frac{X}{C_{v2}}\right)^3} \tag{2.7}$$

$$f_{v3} = \frac{1 + X f_{v1}}{C_v 2} \left[3\left(1 + \frac{X}{C_{v2}}\right) + \left(\frac{X}{C_{v2}}\right)^2 \right] \left(1 + \frac{X}{C_{v2}}\right)^{-3} \tag{2.8}$$

$$X = \frac{\tilde{\nu}}{\nu}, \quad f_w = g \left(\frac{1 + C_{w3}^6}{g^6 + C_{w3}^6} \right)^{\frac{1}{6}} \tag{2.9}$$

$$g = r + C_{w2} \left(r^6 - r \right), \quad r = \frac{\tilde{\nu}}{\tilde{Y} \kappa^2 \Delta^2} \tag{2.10}$$

The models Constants are:

$$C_{b1} = 0.1355 \qquad C_{b2} = 0.622 \qquad \kappa = 0.41$$

$$\sigma = \tfrac{2}{3} \qquad C_{w1} = \tfrac{C_{b1}}{\kappa^2} + \tfrac{1 + C_{b2}}{\sigma} \qquad C_{w2} = 0.3$$

$$C_{w3} = 2 \qquad C_{v1} = 7.1 \qquad C_{v2} = 5$$

The Levi-Civita symbol e_{ijk} used in the vorticity magnitude:

$$e_{ijk} = \begin{cases} +1, & (i,j,k) \in (1,2,3), (2,3,1), (3,1,2) \\ -1, & (i,j,k) \in (1,3,2), (3,2,1), (2,1,3) \\ 0, & \quad i = j, \quad j = k, \quad k = i \end{cases} \tag{2.11}$$

At this point, it is useful to introduce the terms y^+, v^+ and friciton velocity(v_τ). y^+, and v^+ are defined as:

$$y^+ = \frac{v_\tau \Delta^p}{\nu}, \quad v^+ = \frac{v}{v_\tau} \tag{2.12}$$

where Δ^p is the distance of the p cell centre to the wall, ν the kinematic viscosity of the fluid and v_τ the shear velocity. The latter is not a physical flow quantity, and is defined as:

$$v_\tau = \sqrt{\frac{\tau_w}{\rho}} \tag{2.13}$$

where, τ_w is the wall shear stress and ρ is the fluid's density.

As already mentioned, a low-Re turbulence model is implemented. As a result, y^+ must satisfy $y^+ < 1$ (practically $y^+ < 5$) in every case where turbulence is applied. Alternatively, the first cell centres (normal to the solid walls) must be in the viscous sub-layer, where the viscous shear stresses dominate. Using the terms of eq.(2.12), the following condition must be satisfied:

$$y^+ = u^+ \tag{2.14}$$

where the condition is only used as a measure to check whether the first cell centres around the walls are located in the viscous sub-layer ([13]), with the ultimate purpose to check the compatibility of the grid with the low-Re model. Note that in all turbulent cases of this thesis, always $y^+ < 1$.

The system of eqs.(2.1) to (2.3) is solved by introducing proper boundary conditions. A synoptic presentation of each patches boundary conditions on different patches follows:

Inlet

At the inlet patch of each case, a Dirichlet condition is imposed for the v_i and $\tilde{\nu}$(when turbulence is applied). Also a zero Neumann condition is used for the p.

Outlet

A zero Dirichlet condition is imposed on p, and zero Neumann condition on v_i and $\tilde{\nu}$.

Solid Boundaries

The walls of the domain are simulated as no slip walls. It means that a zero Dirichlet condition is used for v_i and $\tilde{\nu}$. Moreover, a zero Neumann condition is imposed on the normal (to the walls) pressure (p) gradient.

2.2 The Adjoint Problem

The optimization problems studied in this diploma thesis are SOO, minimization problems. As can be seen in chapter 4, each problem has a different objective function and constraints. In this chapter, a general approach regarding the handling of the objective function is presented.

Although the first two applications involve laminar flows, for demonstration purposes, the formulation of the continuous adjoint problem as presented in this chapter, includes also the turbulence viscosity terms. The laminar equations are developed in the same way, excluding the turbulence terms and turbulence equations.

2.2.1 Overview of the Adjoint Method

The idea of introducing the adjoint method in aerodynamics shape optimization problems, is to avoid the computation of the derivatives of flow field variables w.r.t. the design variables. Thus, the Adjoint method is considered to be extremely efficient, as the computational cost is relatively independent from the size of the design space, in contrast with other methods such as Direct Differentiation e.t.c. ([1]), where the cost is proportional to the number of design variables. In particular, it requires only the computation of the primal and adjoint fields, once in every optimization cycle, followed by the computation of the sensitivity derivatives.

Considering that the design space is composed by the vector $\vec{b} \in \mathbb{R}^n$, and assume that vector $\vec{U}$ (comprising velocity components v_i, pressure p and $\tilde{\nu}$) includes the state variables. The objective function is of the following form:

$$F = F\left(\vec{b}, \vec{U}(\vec{b})\right), \quad \vec{b} \in \mathbb{R}^n.$$

2.2.2 Adjoint Problem Formulation

In order to avoid the computation of the flow fields derivatives w.r.t. each design variable the augmented objective function is introduced as suggested by [7] where the analysis is drawn from. As a result, the next paragraphs follow the notations of [7]. The augmented objective function including the mean flow equations and the adjoint fields can be written as:

$$F_{aug} = F + \int_\Omega u_i R_i^v d\Omega + \int_\Omega q R^p d\Omega + \int_\Omega \tilde{\nu_a} R^{\tilde{\nu}} d\Omega \tag{2.15}$$

where u_i is the adjoint velocity, q the adjoint pressure and $\tilde{\nu_a}$ the adjoint variable of the turbulence model. As the residuals equal to zero ($R^k = 0$), the sensitivity derivatives of the augmented objective function are equal to those of the initial one $\frac{\delta F_{aug}}{\delta b_n} = \frac{\delta F}{\delta b_n}$:

The differentiation of eq.(2.15), using the Leibniz theorem for the differentiation of volume integrals with variable boundaries (S=S($\vec{b}$)=$\partial\Omega$),

$$\frac{\delta F_{aug}}{\delta b_n} = \frac{\delta F}{\delta b_n} + \int_\Omega u_i \frac{\partial R_i^v}{\partial b_n} d\Omega + \int_\Omega q \frac{\partial R^p}{n} d\Omega + \int_\Omega \tilde{\nu_a} \frac{\partial R^{\tilde{\nu}}}{\partial b_n} d\Omega \tag{2.16}$$

$$+ \int_{S_{W_p}} \left(u_i R_i^v + q R^p + \tilde{\nu_a} R^{\tilde{\nu}}\right) n_k \frac{\delta x_k}{\delta b_n} dS \tag{2.17}$$

where, S_{W_p} denotes the controlled-parameterized surfaces and the n_k stands for the unit vector which is normal to the surface. The boundaries of the domain are expressed as $S = S_I \cup S_O \cup S_W \cup S_{Wp}$, standing for the Inlet, Outlet, fixed and controlled walls respectively.

2.2.3 Field Adjoint Equations Formulation

The final form of FAE are written as:

$$R^q = -\frac{\partial u_j}{\partial x_j} = 0 \tag{2.18}$$

$$\begin{aligned} R_i^u &= u_j \frac{\partial v_j}{\partial x_i} - \frac{\partial (v_j u_i)}{\partial x_j} - \frac{\partial}{\partial x_j}\left[(\nu + \nu_t)\left(\frac{\partial u_i}{\partial x_j} + \frac{\partial u_j}{\partial x_i}\right)\right] + \frac{\partial q}{\partial x_i} \\ &+ \tilde{\nu_a} \frac{\partial \tilde{\nu}}{\partial x_i} - \frac{\partial}{\partial x_l}\left(\tilde{\nu_a} \tilde{\nu} \frac{C_Y}{Y} e_{mjk} \frac{\partial v_k}{\partial x_j} e_{mli}\right) = 0, \quad i = 1, 2(, 3) \end{aligned} \tag{2.19}$$

$$\begin{aligned} R^{\tilde{\nu_a}} &= -\frac{\partial (v_j \tilde{\nu_a})}{\partial x_j} - \frac{\partial}{\partial x_j}\left[\left(\nu + \frac{\tilde{\nu}}{\sigma}\right)\frac{\partial \tilde{\nu_a}}{\partial x_j}\right] + \frac{1}{\sigma}\frac{\partial \tilde{\nu_a}}{\partial x_j}\frac{\partial \tilde{\nu}}{\partial x_j} + 2\frac{C_{b_2}}{\sigma}\frac{\partial}{\partial x_j}\left(\tilde{\nu_a}\frac{\partial \tilde{\nu}}{\partial x_j}\right) + \tilde{\nu_a}\tilde{\nu}C_{\tilde{\nu}} \\ &+ \frac{\partial \nu_t}{\partial \tilde{\nu}}\frac{\partial u_i}{\partial x_j}\left(\frac{\partial v_i}{\partial x_j} + \frac{\partial u_j}{\partial x_i}\right) + (-P + D)\tilde{\nu_a} = 0 \end{aligned} \tag{2.20}$$

After the satisfaction of the FAE, the sensitivity derivatives are given as:

$$
\begin{aligned}
\frac{\delta F_{aug}}{\delta b_n} = & \int_S BC_i^u \frac{\partial v_i}{\partial b_n} dS + \int_S \left(u_j n_j + \frac{\partial F_{S_i}}{\partial p} n_i + \right) \frac{\partial p}{\partial b_n} dS + \int_S BC^{\tilde{\nu_a}} \frac{\partial \tilde{\nu}}{\partial b_n} dS \\
& + \int_S \left(-u_i n_j + \frac{\partial F_{S_k}}{\partial \tau_{ij}} n_k \right) \frac{\partial \tau_{ij}}{\partial b_n} dS - \int_S \tilde{\nu_a} \left(\nu + \frac{\tilde{\nu}}{\sigma} \right) \frac{\partial}{\partial b_n} \left(\frac{\partial \tilde{\nu}}{\partial x_j} \right) n_j dS \\
& + \int_{S_{W_p}} n_i \frac{\partial F_{S_{W_p,i}}}{\partial x_m} n_m \frac{\delta x_k}{\delta b_n} n_k dS + \int_{S_{W_p,i}} \frac{\delta n_i}{\delta b_n} dS + \int_{S_{W_p}} F_{S_{W_p,i}} n_i \frac{\delta (dS)}{\delta b_n} \\
& + \int_{S_{W_p}} (u_i R_i^v + q R^p) + \tilde{\nu_a} R^{\tilde{\nu}}) \frac{\delta x_k}{\delta b_n} n_k dS + \int_{\Omega} \tilde{\nu} \tilde{\nu_a} C_{\Delta} \frac{\partial \Delta}{\partial b_n} d\Omega \qquad (2.21)
\end{aligned}
$$

where:

$$
BC_i^u = u_i v_j n_j + (\nu + \nu_t) \left(\frac{\partial u_i}{\partial x_j} + \frac{\partial u_j}{\partial x_i} \right) n_j - q n_i + \tilde{\nu_a} \tilde{\nu} \frac{C_Y}{Y} e_{mjk} \frac{\partial v_k}{\partial x_j} e_{mli} n_l + \frac{\partial F_{S_k}}{\partial v_i} n_k \qquad (2.22)
$$

$$
BC^{\tilde{\nu_a}} = \tilde{\nu_a} v_j n_j + \left(\nu + \frac{\nu}{\sigma} \right) \frac{\partial \tilde{\nu_a}}{\partial x_j} n_j - \frac{\tilde{\nu_a}}{\sigma} (1 + 2C_{b_2}) \frac{\partial \tilde{\nu}}{\partial x_j} n_j + \frac{\partial F_{S_k}}{\partial \tilde{\nu}} n_k \qquad (2.23)
$$

The eq.(2.21) is used to identify the boundary conditions of the FAE, which are formulated by properly treating the integrals containing the variations in the state variables.

2.2.4 Adjoint Boundary Conditions

Inlet Boundaries, S_I

The boundary conditions imposed at the inlet, is zero Dirichlet condition on $\tilde{\nu_a}$ and zero Neumann condition on q. The inlet conditions imposed on the adjoint velocity are given as:

$$
u_j n_j = u_{<n>} = -\frac{\partial F_{S_{I,i}}}{\partial p} n_i \qquad (2.24)
$$

$$
u_{<t>}^I = \frac{\partial F_{S_{I,k}}}{\partial \tau_{ij}} n_k t_i^I n_j + \frac{\partial F_{S_{I,k}}}{\partial \tau_{ij}} n_k t_j^I n_i \qquad (2.25)
$$

$$
u_{<t>}^{II} = \frac{\partial F_{S_{I,k}}}{\partial \tau_{ij}} n_k t_i^{II} n_j + \frac{\partial F_{S_{I,k}}}{\partial \tau_{ij}} n_k t_j^{II} n_i \qquad (2.26)
$$

$$
\qquad (2.27)
$$

where $u_{<n>}$ is the velocity normal to the inlet and $u^{I}_{<t>}$ & $u^{II}_{<t>}$ are the tangential velocity components to the t^I & t^{II} directions respectively. t^I_i is a vector parallel to the velocity vector, and $t^{II} = e_{ijk} n_j t^I_k$.

Outlet Boundaries, S_O

For the $\tilde{\nu_a}$, in order to eliminate the multiplier of $\partial\tilde{\nu}/\partial b_n$, a Robin-type condition is applied as:

$$BC^{\tilde{\nu_a}} = \tilde{\nu_a} v_j n_j + \left(\nu + \frac{\nu}{\sigma}\right) \frac{\partial \tilde{\nu_a}}{\partial x_j} n_j + \frac{\partial F_{S_O,k}}{\partial \tilde{\nu}} n_k = 0 \tag{2.28}$$

To eliminate term $\partial v_i/\partial b_n$, the following condition is imposed:

$$\begin{aligned} BC^u_i &= u_i v_j n_j + (\nu + \nu_t) \left(\frac{\partial u_i}{\partial x_j} + \frac{\partial u_j}{\partial x_i}\right) n_j - q n_i \\ &+ \tilde{\nu_a}\tilde{\nu} \frac{C_Y}{Y} e_{mjk} \frac{\partial v_k}{\partial x_j} e_{mli} n_l + \frac{\partial F_{S_O,k}}{\partial v_i} n_k \end{aligned} \tag{2.29}$$

Finally, for $u_j n_j$ a zero Neumann condition is imposed.

Fixed/Unparameterized wall Boundaries

Firstly as the walls are fixed all terms of $\frac{\partial}{\partial b_n}$ and $\frac{\delta}{\delta b_n}$ are equal to zero. In order to eliminate the term $\frac{\partial}{\partial b_n}\left(\frac{\partial \tilde{\nu}}{\partial x_j}\right) n_j$, a zero Dirichlet condition is applied for the $\tilde{\nu_a}$. The normal adjoint velocity is imposed to be:

$$u_{<n>} = -\frac{\partial F_{S_{W,i}}}{\partial p}, \tag{2.30}$$

and the tangential adjoint velocity (in II direction):

$$u^{II}_{<t>} = \frac{\partial F_{S_{W,k}}}{\partial \tau_{ij}} n_k t^{II}_i n_j + \frac{\partial F_{S_{W,k}}}{\partial \tau_{ij}} n_k t^{II}_j n_i \tag{2.31}$$

Parameterized/Controlled Boundaries, S_{W_p}

The primal and adjoint boundary conditions imposed along the controlled boundaries S_{W_p} are identical to those imposed for S_w.

2.2.5 Sensitivity derivatives

After satisfying the FAE, subject to ABC, the sensitivity derivatives final expression is written as:

$$
\begin{aligned}
\frac{\delta F_{aug}}{\delta b_n} = T_{SD}^{WF} &- \int_{S_{W_p}} SD_1 \frac{\partial \tau_{ij}}{\partial x_m} n_j t_i^I n_m n_k \frac{\delta x_k}{\delta b_n} dS - \int_{S_{W_p}} SD_1 \tau_{ij} \frac{\delta (n_j t_i^I)}{\delta b_n} \frac{\delta x_k}{\delta b_n} dS \\
&+ \int_{S_{W_p}} SD_{2,i} v_{<t>}^I \frac{\delta t_i^I}{\delta b_n} dS - \int_{S_{w_p}} SD_{2,i} \frac{\partial v_i}{\partial x_m} n_m n_k \frac{\delta x_k}{\delta b_n} dS \\
&- \int_{S_{W_p}} \left[\left(\nu + \frac{\tilde{\nu}}{\sigma} \right) \frac{\partial \tilde{\nu_a}}{\partial x_j} n_j + \frac{\partial F_{S_k}}{\partial \tilde{\nu}} \right] \frac{\partial \tilde{\nu}}{\partial x_m} n_m n_k \frac{\delta x_k}{\delta b_n} dS \\
&- \int_{S_{W_p}} (-u_{<n>} + \phi_{<n><n>}) \left(\tau_{ij} \frac{\delta (n_i n_j)}{\delta b_n} + \frac{\partial \tau_{ij}}{\partial x_m} n_m \frac{\delta x_k}{\delta b_n} n_k n_i n_j \right) dS \\
&- \int_{S_{W_p}} \phi_{<t^I><t^I>} \left(\tau_{ij} \frac{\delta (t_i^I t_j^I)}{\delta b_n} + \frac{\partial \tau_{ij}}{\partial x_m} n_m \frac{\delta x_k}{\delta b_n} n_k t_i^I t_j^I \right) dS \\
&- \int_{S_{W_p}} (\phi_{<t^{II}><t^I>} + \phi_{<t^I><t^{II}>} \left(\tau_{ij} \frac{\delta (t_i^{II} t_j^I)}{\delta b_n} + \frac{\partial \tau_{ij}}{\partial x_m} n_m \frac{\delta x_k}{\delta b_n} n_k t_i^{II} t_j^I \right) dS \\
&- \int_{S_{W_p}} \phi_{<t^{II}><t^{II}>} \left(\tau_{ij} \frac{\delta (t_i^{II} t_j^{II})}{\delta b_n} + \frac{\partial t_{ij}}{\partial x_m} n_m \frac{\delta x_k}{\delta b_n} n_k t_i^{II} t_j^{II} \right) dS \\
&+ \int_{S_{W_p}} n_i \frac{\partial F_{S_{W_p,i}}}{\partial x_m} n_m \frac{\delta x_k}{\delta b_n} n_k dS + \int_{S_{W_p}} F_{S_{W_p,i}} \frac{\delta n_i}{\delta b_n} dS + \int_{S_{W_p}} F_{S_{W_p,i}} n_i \frac{\delta (dS)}{\delta b_n} \\
&+ \int_{S_{W_p}} (u_i R_i^v + q R^p + \tilde{\nu_a} R^{\tilde{\nu}} + \Delta_a R^{\Delta}) \frac{\delta x_k}{\delta b_n} n_k dS \\
&- \int_{S_{w_p}} 2 \Delta_a \frac{\partial \Delta}{\partial x_j} n_j \frac{\partial \Delta}{\partial x_m} n_m n_k \frac{\delta x_k}{\delta b_n} dS
\end{aligned}
\tag{2.32}
$$

where:

$$
SD_1 = -u_{<t>}^I + \phi_{<t^I><n>} + \phi_{<n><t^I>} \tag{2.33}
$$

$$
SD_{2,i} = (\nu + \nu_t) \left(\frac{\partial u_i}{\partial x_j} + \frac{\partial u_j}{x_i} \right) n_j - q n_i + \frac{\partial F_{S_{W_p,k}}}{\partial v_i} n_k \tag{2.34}
$$

$$
\phi_{ij} = \frac{\partial F_{S_{W_p,k}}}{\partial \tau_{ij}} n_k \tag{2.35}
$$

Due to the non-zero variations in the normal and tangential vectors to the S_{W_p} boundaries, some additional terms are included in eq.(2.32). The terms of eq.(2.35) and T_{SD}^{WF} summarize the contribution of the wall functions differentiation. Specifically, term T_{SD}^{WF} results from the differentiation of the wall low. The 6^{th} integral results from the differentiation of turbulence, where the last integral is the contribution of the distance variation included to the turbulence model.

2.3 Optimization Algorithm

The optimization algorithm is briefly presented as follows:

1. Parameterization of the geometry and selection of the deisgn variables ($\vec{b} \in \mathbb{R}^n$).
2. Solving the primal problem for the computation of $v_i, p, \tilde{\nu}$.
3. Evaluation of the aerodynamic performance (F). The first convergence criterion: If the relative difference w.r.t. the previous cycle's value is less than the predefined threshholds, the optimization loop ends.
4. Solving the FAE for the $u_i, q, \tilde{\nu_a}$ fields.
5. Compute the sensitivity derivatives $\delta F/\delta b_n$. The second convergence criterion: If all sensitivity derivatives are lower than the predefined values, the optimization loop converges.
6. Update the design variables(b_n^{new}).
7. Update the grid.
8. Steps 2 to 7 are repeated until the convergence of the optimization loop or completing the maximum number of optimization cycles.

Chapter 3

Parametric Effectiveness - Definitions

3.1 Generalities

PE is a quality metric characterizing the parameterization of the shape to be designed and, as such, can become very useful in supporting gradient-based shape optimization runs in case any parameterization scheme, other than nodal parameterization, is involved. In this diploma thesis, PE is computed and used in aerodynamic shape optimization problems that are solved using continuous adjoint method. However, the PE can equally be used with discrete adjoint. In general, computing the PE is a way to understand the effectiveness of this parameterization which, in turn, helps the designer making decisions on the number and quality of design variables. As such, it can definitely be exploited in an attempt to reduce the computational cost of the optimization loop.

PE is described as the ratio of the optimization potential of a NURBS curves or volumetric B-splines parameterization to the gain expected if a nodal parameterization was used instead. The latter corresponds to the optimization of the shape by individually displacing all nodes over the contour or surface of the body to be designed, an action that gives the richest possible design space. In this diploma thesis, both NURBS curves and volumetric B-splines parameterization will be referred as CAD parameterizations, (in the sense that corresponding quantities will be indexed by "CAD", even though volumetric schemes a.k.a. free-form deformation techniques, are the exact opposite to CAD). Quantities computed by using nodal parameterization will be referred to as “NODAL”.

3.2 PE Definition

PE is defined as the ratio of objective function’s gains using a CAD parameterization of the geometry to the corresponding gain of objective function by using nodal parameterization, during a gradient-based shape optimization loop. It must be noted that definition and computation of PE in this diploma thesis differs from the original work of [3], even if this work was practically inspired our developments.

PE is defined as:

$$PE = \frac{\Delta J^{CAD}}{\Delta J^{NODAL}} \tag{3.1}$$

where:

J is the objective function value of the aerodynamic shape optimization under consideration,

ΔJ^{CAD} is the expected gain in J using CAD parameterization (see comment on index “CAD” in the previous subsection),

ΔJ^{NODAL} is the expected gain in J using nodal parameterization.

In this work and without loss in generality, it is assumed that the optimization will be performed using the steepest descent method. Both ΔJ gains can be derived using first-order Taylor-linearisation as follows:

$$\Delta J^{CAD} = \left(J^{new} - J^{old}\right)^{CAD} = \frac{dJ}{d\vec{b}}\Delta\vec{b} \tag{3.2}$$

$$\Delta J^{NODAL} = \left(J^{new} - J^{old}\right)^{NODAL} = \frac{dJ}{d\vec{X}_s}\Delta\vec{X}_s \tag{3.3}$$

where:

$\vec{b}$ is the vector of the design variables of the CAD parameterization,

$\vec{X}_s$ is the vector of the coordinates of the nodes on the body surface,

$\Delta\vec{b}$ is the change in the values of design variables in an optimization step using CAD parameterization,

$\Delta\vec{X}_s$ is the displacement of the surface nodes in an optimization step using nodal parameterization,

$\frac{dJ}{d\vec{b}}$ is the vector of the derivatives of J w.r.t. $\vec{b}$,

$\frac{dJ}{d\vec{X}_s}$ is the vector of the derivatives of J w.r.t. $\vec{X}_s$

If steepest descent is used to compute $\Delta\vec{b}$ & $\Delta\vec{X}_s$, in a minimization problem, these are given by:

$$\Delta\vec{b} = -\eta_{CAD}\left(\frac{dJ}{d\vec{b}}\right)^T \tag{3.4}$$

$$\Delta\vec{X}_s = -\eta_{NODAL}\left(\frac{dJ}{d\vec{X}_s}\right)^T \tag{3.5}$$

where η_i is the steepest descent step for each method. The final forms of ΔJ for the two parameterizations becomes:

$$\Delta J^{CAD} = -\eta_{CAD}\left(\frac{dJ}{d\vec{b}}\right)^2 \tag{3.6}$$

$$\Delta J^{NODAL} = -\eta_{NODAL}\left(\frac{dJ}{d\vec{X}_s}\right)^2 \tag{3.7}$$

The steepest descent assumption made above does not imply that this is the method to be used in the optimization loop, but provides an easy way to define, compute and use PE.

Steepest descent is strongly dependent on the η value since this value determines the magnitude of change either in the design variables or node's coordinates. As the design variables sensitivity derivatives have different order of magnitude than nodal's sensitivity derivatives, η values for the two cases (NODAL and CAD) generally differ. In PE, the interest is not on the actual value of the two η; instead, it is their ratio that matters in order to have a fair comparison of the two methods.

For a fair comparison of CAD and nodal parameterization, a constraint of "total surface deformation" is introduced. The constraint demands equal magnitude of geometry's total deformation after an optimization cycle for both approaches. For the nodal optimization, deformation is directly linked with $\Delta\vec{X}_s$. For CAD parameterization, $\Delta\vec{X}_s$ emerges indirectly from the computed $\Delta\vec{b}$. A surface integral of the squared normal displacement of the surface nodes of each method, must be computed. This is a working assumption and, of course, different constraints can be implemented.

The above constraint is written as:

$$\int_S \left(\Delta\vec{X}_s^{\,NODAL} \cdot \vec{n}\right)^2 dS = \int_S \left(\Delta\vec{X}_s^{\,CAD} \cdot \vec{n}\right)^2 dS \tag{3.8}$$

where:

$\vec{n}$ is the normal unit outward vector over the surface to be optimized,

$\Delta\vec{X}_s^{\,NODAL}$ is the surface deformation when using nodal parameterization,

$\Delta\vec{X}_s^{\,CAD}$ is the surface deformation when using a CAD parameterization.

The surface deformation if nodal parameterization is used is computed by eq.(3.5).

In CAD parameterization, the displacement of the surface nodes is connected with changes of the design variables as follows:

$$\Delta\vec{X}_s^{\,CAD} = \left(\frac{d\vec{X}_s}{d\vec{b}}\right)^{CAD} \Delta\vec{b} \tag{3.9}$$

where:

$\left(\frac{d\vec{X}_s}{d\vec{b}}\right)^{CAD}$ is the derivative of surface nodes coordinates w.r.t. the design variables of CAD parameterization.

By replacing $\Delta\vec{b}$ as computed by eq.(3.4), the above equation can be written as:

$$\Delta\vec{X}_s^{\,CAD} = -\eta_{CAD}\frac{d\vec{X}_s}{d\vec{b}}\left(\frac{dJ}{d\vec{b}}\right)^T_{CAD} \tag{3.10}$$

The final integral form of the constraint of eq. (3.8), after replacing equations (3.5) and (3.10) is given by:

$$\int_S \eta^2_{NODAL}\left(\frac{dJ}{d\vec{X}_S} \cdot \vec{n}\right)^2_{NODAL} dS = \int_S \eta^2_{CAD}\left(\frac{d\vec{X}_s}{d\vec{b}}\frac{dJ^T}{d\vec{b}} \cdot \vec{n}\right)^2_{CAD} dS \tag{3.11}$$

Since the two η values are constant, they can be used as multipliers outside of the integrals. Following a re-arrangement of eq.(C.2), the ratio of η for a fair comparison (according to the criterion/constraint defined above) is:

$$\frac{\eta_{CAD}}{\eta_{NODAL}} = \sqrt{\frac{\int_s \left(\frac{dJ}{d\vec{X}_s} \cdot \vec{n}\right)^2_{NODAL} dS}{\int_s \left(\frac{d\vec{X}_s}{d\vec{b}} \frac{dJ}{d\vec{b}}^T \cdot \vec{n}\right)^2_{CAD} dS}} \tag{3.12}$$

By means of eqs. (C), (3.6). (3.7) and (3.12), the mathematical expression of PE takes the form:

$$PE = \sqrt{\frac{\int_s \left(\frac{dJ}{d\vec{X}_s} \cdot \vec{n}\right)^2_{NODAL} dS}{\int_s \left(\frac{d\vec{X}_s}{d\vec{b}} \frac{dJ}{d\vec{b}}^T \cdot \vec{n}\right)^2_{CAD} dS} \quad \frac{\left(\frac{dJ}{d\vec{b}}\right)^2_{CAD}}{\left(\frac{dJ}{d\vec{X}_s}\right)^2_{NODAL}}} \tag{3.13}$$

The above equation comprises the following four terms (numerators or denominators in eq.(3.13))

$$Term1 = \int_s \left(\frac{d\vec{X}_s}{d\vec{b}} \frac{dJ}{d\vec{b}}^T \cdot \vec{n}\right)^2_{CAD} dS \tag{3.14}$$

$$Term2 = \int_s \left(\frac{dJ}{d\vec{X}_s} \cdot \vec{n}\right)^2_{NODAL} dS \tag{3.15}$$

$$Term3 = \left(\frac{dJ}{d\vec{b}}\right)^2_{CAD} \tag{3.16}$$

$$Term4 = \left(\frac{dJ}{d\vec{X}_s}\right)^2_{NODAL} \tag{3.17}$$

Thus, overall, we may rewrite eq.(3.13) in the symbolic form:

$$PE = \sqrt{\frac{Term2}{Term1} \quad \frac{Term3}{Term4}} \tag{3.18}$$

3.3 Computation of PE

In this section, basic information regarding PE computation, such as the management of the adjoint optimization solver results and the presentation of PE terms in discrete form are given.

3.3.1 Prerequisites of PE

This paragraph presents all the prerequisites for the PE computation, including sensitivity derivatives, normal unit vectors and section areas regarding the geometry to be optimized. In whatever follows, N_b symbolizes the number of design variables and N_s the number of surface nodes.

Nodal sensitivity derivatives

Nodal sensitivity derivatives $\frac{dJ}{d\vec{X_s}}$ are computed directly from the (continuous) adjoint code for every surface node.

In this diploma thesis, this is used in tensor form as follows:

$$\frac{dJ}{dx_{ij}} \tag{3.19}$$

where, $\mathbf{i} = \mathbf{1}, \ldots, \mathbf{N_s}$ defines node's ID and $\mathbf{j} = \mathbf{1}, \mathbf{2}$ defines the coordinates in the Cartesian Space. The tensor consist of N_s lines each of which containing the corresponding node's sensitivity derivatives in all directions of the domain (x and y). This tensor is used directly in the computation of the PE terms that refer to the nodal optimization (Term 2 & Term 4), and also for the computation of CAD parameterization's sensitivity derivatives.

Sensitivity derivatives w.r.t. $\vec{b}$

The sensitivity derivatives vector $\frac{dJ}{d\vec{b}}$ can be re-written as, $\frac{dJ}{db_k}$. Indicator k is the ID of the corresponding design variable. In $\vec{b}$, the design variables can follow a suitable arrangement specified by the user. According to (3.19), this is computed using Einstein's convention as:

$$\frac{dJ}{db_k} = \frac{dJ}{dx_{ij}} \frac{dx_{ij}}{db_k} \tag{3.20}$$

Geometrical Data

Geometrical data refer to normal unit vectors as well as section's area around nodes. Normal unit vector is provided as a tensor $\mathbf{n}_{ij}$, where i,j indicators follow the same convention as in x_{ij} of (3.19). Section areas are provided as an array, where each component of ΔS_i refers to the corresponding node's ID.

3.4 PE Terms in Discrete form

The PE terms are written in discrete form, in the same order as computed by the PE algorithm, as follows:

$$Term1 = \sum_{i=1}^{N_s} \left[\sum_{j=1}^{2} \left[\sum_{k=1}^{N_b} \left(\frac{dx_{ij}}{db_k} \frac{dJ}{db_k} \right) \right] n_{ij} \right]^2 \Delta S_i \tag{3.21}$$

$$Term2 = \sum_{i=1}^{N_s} \left[\sum_{j=1}^{2} \left(\frac{dJ}{d_{ij}} n_{ij} \right)^2 \right] \Delta S_i \tag{3.22}$$

$$Term3 = \sum_{k=1}^{N_b} \left(\frac{dJ}{db_k} \right)^2 \tag{3.23}$$

$$Term4 = \sum_{i=1}^{N_s} \left[\sum_{j=1}^{2} \left(\frac{dJ}{dx_i j} \right)^2 \right] \tag{3.24}$$

The PE value finally results from eq.(3.18).

Although the PE theory is developed and presented for 2D applications, its generalization in 3D applications is straight forward and can be obtained simply adapting the above sums.

3.5 PE evaluation details

As mentioned above, PE is a relative efficiency of the selected parameterization w.r.t. the efficiency of the nodal parameterization. We expect it's values to range from zero to one. As the PE value tends to 1, the potential of a

CAD parameterization's optimization tends to that of the nodal optimization which is considered to be the richest possible way to solve the problem.

The PE evaluation can be implemented regardless of whether a geometry is designed using specific CAD software's features. The geometry's initial design can be done using any CAD software. In this work, for geometries that are not initially designed using a specific CAD parameterization, prior to their shape optimization, a CAD parameterization can be generated by best-fit procedures. All applications in this diploma thesis utilize NURBS curves or Volumetric B-splines as CAD parameterization.

As an optimization loop goes on, the value of PE changes due to the simultaneously updated design variables. Changing their values during the optimization leads to the deformation of the geometry to be optimized at the end of each optimization cycle. In the following chapters, the latter will be observed by evaluating the PE of different parameterizations that produce different geometries for the same application.

Chapter 4

PE-studies-Understanding PE

This chapter elaborates on the computation of PE (as defined in chapter 3) in applications of 2D external and internal aerodynamics. The purpose of this chapter is to implement the PE theory in practice, study the PE behaviour and provide the PE values of each application. To better understand the PE behaviour, parametric studies regarding the PE value w.r.t. the number of control points is conducted to evaluate the PE as parameterization gets richer. This is examined in three different applications, an isolated airfoil, an S-bend duct and a stator blading of an axial compressor.

4.1 The isolated airfoil case

The objective function for all studies related to the isolated airfoil is drag. The drag force D is defined as the integral of viscous and pressure stresses over the surface of the airfoil. The drag due to the airfoil's shape is expressed as a non-dimensional quantity, instead of the drag itself the drag coefficient (C_D) is used as the objective function:

$$J = C_D = \frac{D}{\frac{1}{2}\rho A U_\infty^2} = \frac{\int_S \rho \left(-\tau_{ij} n_j + p n_i\right) r_i dS}{\frac{1}{2}\rho A U_\infty^2} \tag{4.1}$$

where:

A is the reference area. In any case is the airfoil chord, which is unit.

U_∞ is the far-field velocity magnitude ($6m/s$ in an angle of attack of $2\,\mathrm{deg}$),

τ_{ij} is the stress tensor,

p is the "kinematic pressure" i.e. the pressure divided by the fluid's density,

n_k is the normal (to the airfoil walls) unit vector (pointing towards the solid),

r_i is the unit vector in the direction of the force, which coincides with the direction of the far-field velocity.

The flow is decided to be laminar with Reynolds number equal to 1000; though it would be more realistic to have a turbulent flow, this has nothing to add regarding the studies on PE. For the primal and adjoint fields computations, as well as the sensitivity derivatives extraction, the OpenFOAM software, is used. More information regarding the application's CFD setup and results (from the point of view of the fluid flow) can be found in section B.1.

The selected geometry is the NACA 0012 symmetrical airfoil which will be referred as the "reference" airfoil for the rest of this section. The airfoils of this study are parameterized using two distinct NURBS curves per airfoil side, generated based on the reference airfoil by a best-fit algorithm. In the following tables and figures the number of CPs given per case is always for the total CPs of the airfoil (i.e. twice as high as the number of CPs per airfoil side). The leading and trailing CPs of each side are fixed. More details regarding the parameterization of the airfoils can be found in Appendix A. An example of the airfoil parameterization produced by the best fit algorithm is displayed in Figure 4.1.

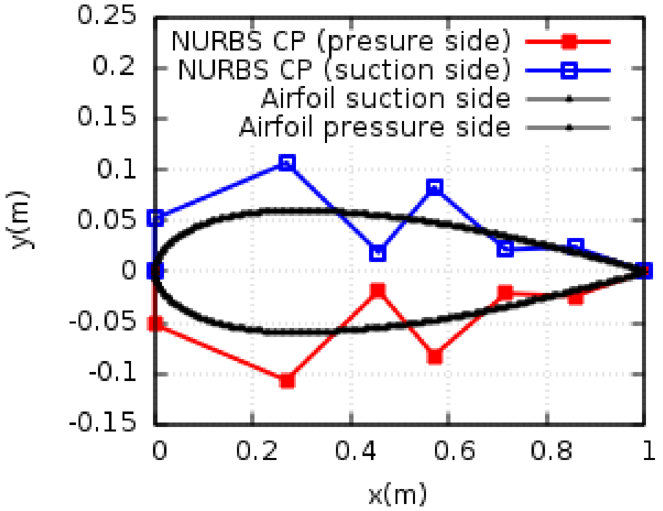

Figure 4.1: *NURBS parameterization of the reference airfoil using 16 CPs in total.*

The design variables in all cases are the x,y coordinates of the CPs that are allowed to displace, i.e. excluding the first and last CP on each side.

Therefore, the total number of design variables is $N_b = 2N_{CP} - 8$, where N_{CP} is the total number of CPs. The same applies for the surface nodes in nodal parameterization.

Below, three parametric studies are presented:

- **Study 1:** The PE values are computed and compared on the exact same airfoil, with 14 to 24 CPs (through enrichment which keeps the airfoil shape intact (see subsection A.2.1)). The shape of the studied airfoil is produced from the best-fit procedure of the reference airfoil utilizing 14 CPs in total which is the minimum number of the above, so as to, then, create all the other parametrizations through enrichment. These shapes differ slightly from the reference airfoil.

- **Study 2:** It is a similar study as the previous one. The only difference is that the primal and adjoint codes run on the reference airfoil, even if geometric sensitivities are computed on a slightly changed airfoil (that of Study 1). This speeds up the computation but introduces a certain incosistency.

- **Study 3:** In this study, PE values, in the range of 12 to 24 CPs, are also computed and compared. However, for each different number of CPs, a different best-fit of the reference airfoil has been performed. As a result airfoils are (slightly) different from each other.

- **Study 4:** In this study, the Individual PE of design variables is computed for Cases 3 and 5 of Study 3.

The parameterizations used in Studies 1 and 2 are presented in figures 4.2 and 4.3. As it can be observed, the distribution of CPs when enrichment is used is different compared to the corresponding parameterizations where best-fit is performed so as to compute the best shape (i.e. the closest to the reference airfoil) with each number of control nodes.

Study 1

Results are presented in Table 4.1 and Figure 4.4. It is observed that, as CAD parameterization becomes richer, the PE value is monotonically increasing. Particularly, the PE curve asymptotically converges to a maximum PE value. Also, as expected, Terms 2 and 4, take on the exact same values in all cases since the airfoil's shape is identical and these two refer to the nodal parameterization (same nodes).

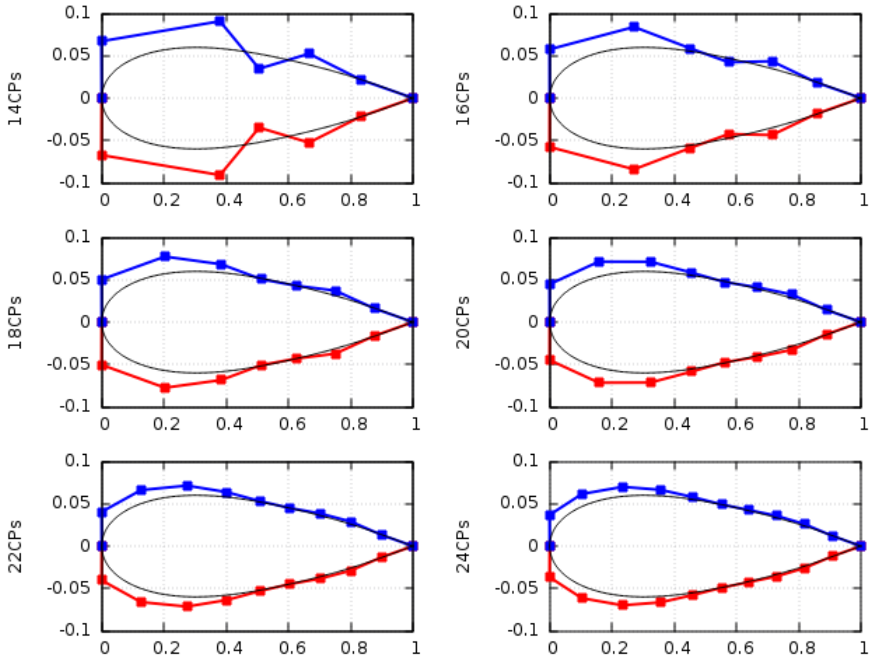

Figure 4.2: *Parameterizations of Study 1 using enrichment. The horizontal axis of each plot refers to the x direction whereas the vertical to to y direction. All dimensions are scaled with the chord-length.*

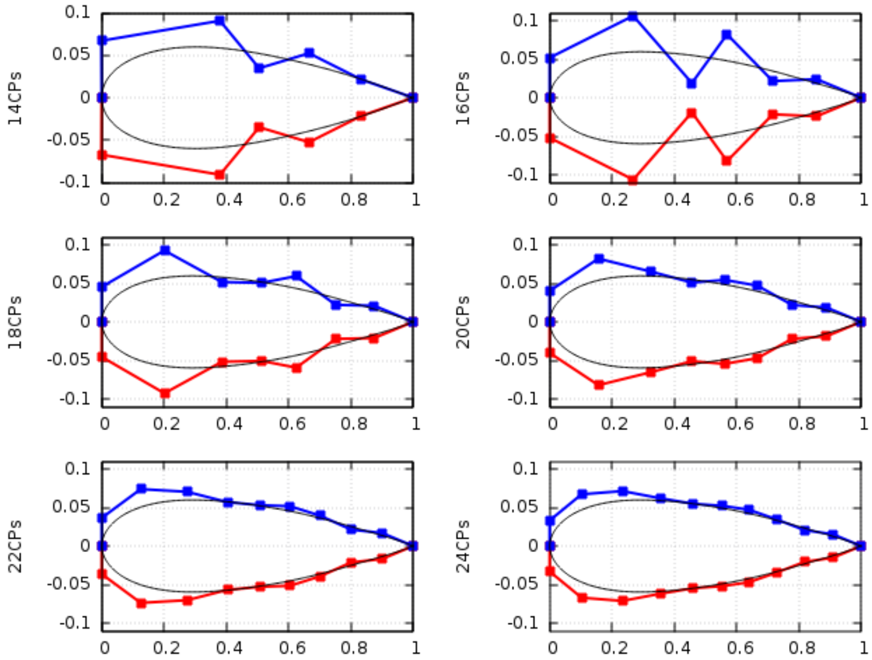

Figure 4.3: *Parameterizations of Study 2 using the best fit for each case's parameterization. The horizontal axis of each plot refers to the x direction whereas the vertical to to y direction. All dimensions are scaled with the chord-length.*

Case ID	N_{CP}	PE	Term1	Term2	Term3	Term 4
1	14	0.7706	4.6838	0.003256	9.6668	0.3307
2	16	0.7808	3.9360	0.003256	8.9784	0.3307
3	18	0.7891	3.3322	0.003256	8.3491	0.3307
4	20	0.7960	2.8468	0.003256	7.7843	0.3307
5	22	0.8017	2.4545	0.003256	7.2805	0.3307
6	24	0.8066	2.1348	0.003256	6.8312	0.3307

Table 4.1: *Study 1: Evolution of the PE values w.r.t the number of CPs.*

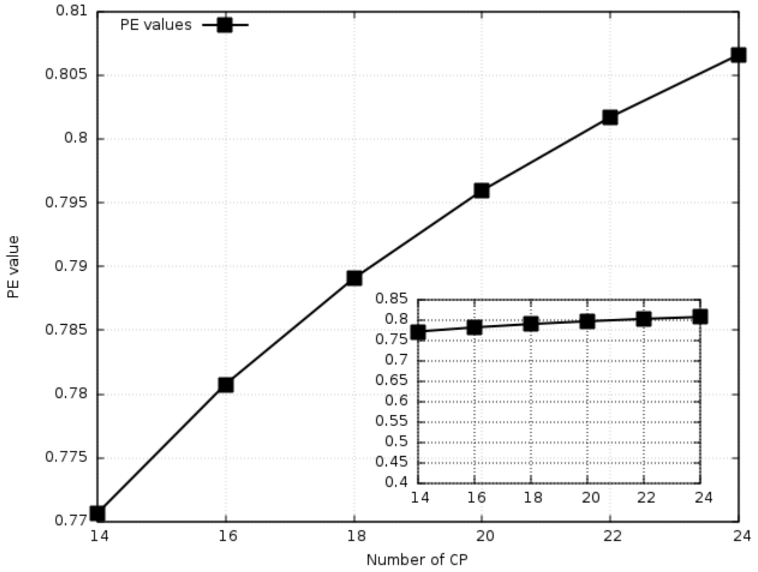

Figure 4.4: *Study 1: Results of the PE values w.r.t. the number of CPs.*

Study 2

This study has a lower computational cost and, strictly speaking, is less meaningful than Study 1. In fact, in this study, there is an inconsistency regarding the computation of nodal sensitivity derivatives and basis functions. Specifically, the $i^{th'}$ and i^{th} node of the parameterized and reference airfoil respectively, are different. Since CAD sensitivity derivatives are computed as $\frac{dJ}{dx_i}\frac{dx_i^{'}}{db_k}$, the chain rule is inconsistent as the two derivatives are computed on different nodes. The value of this study comes from the lower computational cost it has and the fact that there is no need to implement a method that adapts the internal grid to slightly changed boundaries.

In Table 4.2 and Figure 4.5 the results of the study are presented. The PE curve has a similar form to that of Study 1, however with greater (though ”less accurate”) PE values.

Case ID	N_{CP}	PE	Term1	Term2	Term3	Term4
1	14	0.7823	4.6815	0.003262	9.6715	0.32632
2	16	0.7928	3.9351	0.003262	8.9859	0.32632
3	18	0.8014	3.3703	0.003262	8.9288	0.32626
4	20	0.8085	2.8467	0.003256	7.7840	0.33072
5	22	0.8144	2.4560	0.003262	7.2920	0.32630
6	24	0.8194	2.1360	0.003262	6.8430	0.32630

Table 4.2: *Study 2: Evolution of the PE values w.r.t the number of CPs.*

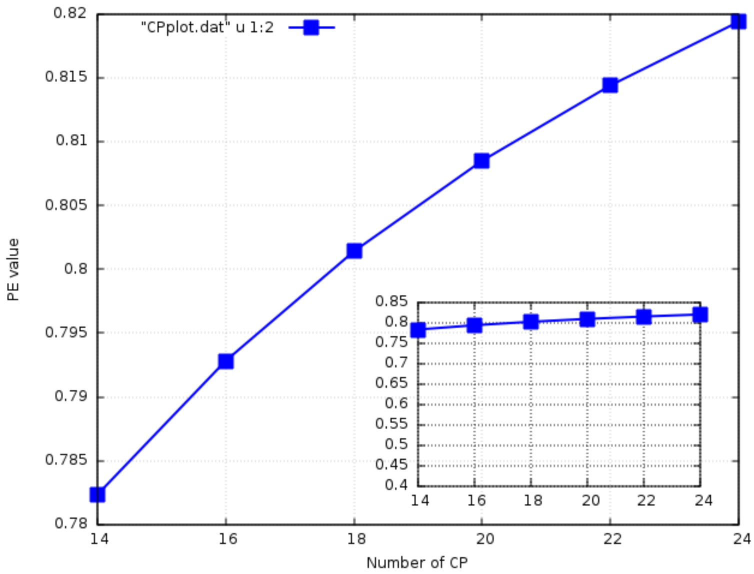

Figure 4.5: *Study 2: Results of the PE values w.r.t. the number of CPs.*

Study 3

In Table 4.3 and Figure 4.6 the results of this parametric study are presented. Each row of Table 4.3 corresponds to a different airfoil. For this reason, Term 2 and Term 4 get different values in every case. However, for the NURBS parameterizations with a total number of CPs greater than 14, the differences in Terms 2 and 4 are minor. Moreover, as it can be observed in Term 1 to Term 4 columns of Table 4.3, as NURBS parameterization becomes richer, these four terms (constituents of the PE) are constantly decreasing. Despite the decrease in Terms 1 and 3, their corresponding ratio becomes higher, thus leading to higher PE values. Finally, by observing the last two columns of Table 4.3, Term 3 values are greater than the corresponding Term 4 values in all cases. However, this does not invalidate the working hypothesis that nodal parameterization is considered to provide the greatest optimization potential.

The PE curve is monotonically increasing, converging to a maximum PE value, similarly to the curves of Studies 1 and 2 in Figure 4.4 and Figure 4.5 respectively. In addition, the Figure 4.6 indicates that, the increase in the PE value between Studies 1 and 2 is significant. The latter is due to the inability of the Case 1 parameterization to produce such a detailed airfoil shape compared to the other cases of Study 3, due to its relatively poor parameterization.

Case ID	CPs No	PE value	Term1	Term2	Term3	Term4
1	12	0.5548	0.61697	0.0041706	1.14712	0.053753
2	14	0.7706	0.46838	0.0032556	0.99968	0.053072
3	16	0.7928	0.43725	0.0036246	0.99848	0.036260
4	18	0.8014	0.37028	0.0036246	0.92878	0.036260
5	20	0.8085	0.31641	0.0036246	0.86616	0.036260
6	22	0.8144	0.27287	0.0036246	0.81024	0.036260
7	24	0.8194	0.23735	0.0036244	0.76030	0.036258

Table 4.3: *Study 3: Evolution of the PE values w.r.t the number of control points. Each row corresponds to a slightly different airfoil.*

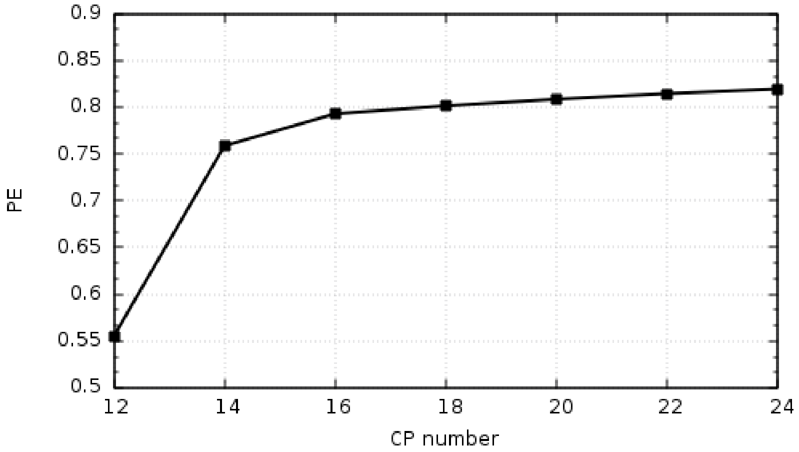

Figure 4.6: *Study 3: Results of the PE values w.r.t. the number of CPs.*

Study 4

So far, there was a single PE value characterizing the whole shape. This time, an attempt is made to define a new metric (IPE-Individual Parametric Effectiveness) that characterizes the effect of its design variable, rather than all of them as a whole. To be more precise, the new metric will be denoted by IPE_k, where k is the design variable's ID.

The IPE computation requires two modifications in Terms 1 and 3 given in eq.(3.21) and eq.(3.23), respectively. The first modification is the substitution of the sum of the squared values of design variables sensitivity derivatives in Term 3, with the squared value of the k^{th} sensitivity derivative of each design variable. The second modification is the subtraction of the sum corresponding to the design variables from eq.(3.21). The modified terms can be written as:

$$Term1_k = \sum_{i=1}^{N_s} \sum_{j=1}^{2} \left(\frac{dx_{ij}}{db_k} \frac{dJ}{db_k} \right)^2 \Delta S_i \tag{4.2}$$

$$Term3_k = \left(\frac{dJ}{db_k} \right)^2 \tag{4.3}$$

where all indices are the same as in eqs.(3.21)-(3.24). Then, the IPE of each design variable is computed as:

$$IPE_k = \sqrt{\frac{Term2}{Term1_k} \frac{Term3_k}{Term4}} \tag{4.4}$$

For demonstration purposes, it was decided to present the IPE of design variables of the Cases 3 (16CPs) and 5 (20 CPs) of Study 3 (Table 4.3). The IPE values for both cases are presented in Table 4.4. Note that, as the x and y coordinates of each control point are considered to be design variables, each row of the Table 4.4 refers to a certain CP, containing the IPE values for its x and y coordinates in separate columns. The CPs IDs range from 0 to $N_{CP} - 1$, where N_{CP} is the total number of CPs, starting from the pressure side's first CP, to the suction side's last CP. The first half of the CPs of each parameterization refers to the pressure side and the other half to its suction side. Table 4.4 includes only the CPs the coordinates of which are considered as design variables (i.e. are free to be displaced).

The IPE values in Table 4.4 regarding the y coordinates are greater than those of the x coordinates in both cases. Therefore, the distributions of the IPE values regarding x and y coordinates are plotted separately in Figure 4.7 and Figure 4.8 respectively. The blue/continuous lines refer to Case 3, whereas the red/dashed line to Case 5. Horizontal axis refers to the CPs ID and vertical axis to the IPE values.

Both figures 4.7 and 4.8 indicate that the peak IPE values for the x and y coordinates appear at the second CP of the suction side of each airfoil. The peak value of Case 3 corresponds to the 9^{th} CP, whereas in Case 5 to the 11^{th} CP. The distribution of the IPE values w.r.t. the CPs number in both cases is similar, except from the sections of their peak values in Figure 4.8. The latter, is due to the most dense distribution of CPs in Case 5 compared to Case 3, as the 2nd and 3rd CPs of the suction side in Case 5 are closer to the leading edge of the airfoils(which is the area with the greatest optimization potential) than the corresponding CPs of Case 3.

16CPs parameterization			20CPs parameterization		
CP's ID	IPE_X	IPE_Y	CP's ID	IPE_X	IPE_Y
1	0.05345	0.34812	1	0.06279	0.32848
2	0.01995	0.34176	2	0.03408	0.32820
3	0.00418	0.33494	3	0.00947	0.31698
4	0.01965	0.34069	4	0.00688	0.31264
5	0.03080	0.35829	5	0.01812	0.31776
6	0.04037	0.39817	6	0.02672	0.32979
9	0.10015	0.59191	7	0.03403	0.34909
10	0.03857	0.55107	8	0.04119	0.39236
11	0.00184	0.45896	11	0.11841	0.56133
12	0.01389	0.35699	12	0.06191	0.56042
13	0.01739	0.25916	13	0.01975	0.50145
14	0.01332	0.17282	14	0.00371	0.42385
-	-		15	0.01443	0.34381
-	-		16	0.01751	0.26694
-	-		17	0.01593	0.19561
-	-		18	0.01030	0.13499

Table 4.4: *Study 4: IPE values of the design variables of Cases 3 and 5 of Study 3 (see Table 4.3).*

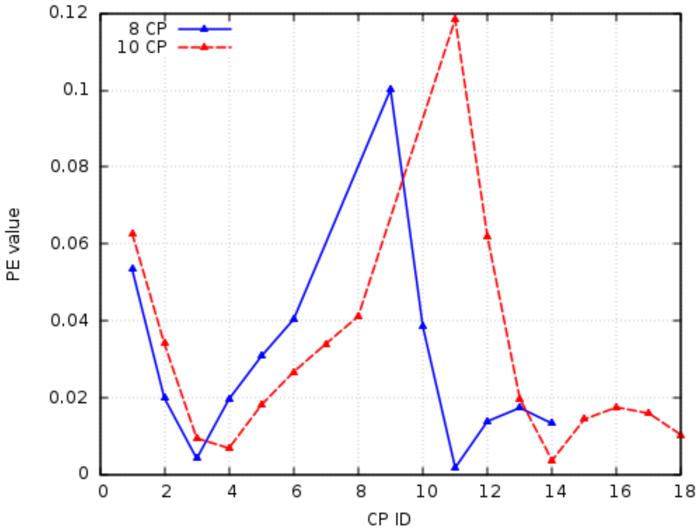

Figure 4.7: *Study 4: IPE values of the x coordinates of all CPs in Cases 3 and 5 of Study 3.*

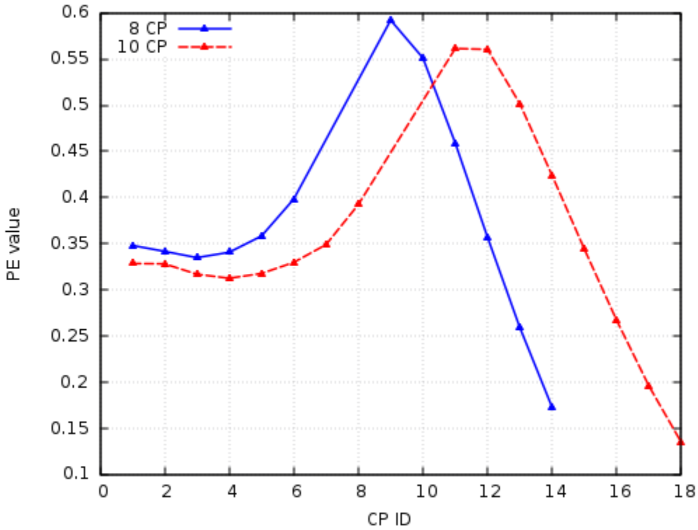

Figure 4.8: *Study 4: IPE values of the y coordinates of all CPs in Cases 3 and 5 of Study 3.*

Finally, a comparison between the IPE and the CAD sensitivity derivatives is made in figures 4.9 and 4.10 of Case 5. In these figures, the absolute values of sensitivity derivatives are presented in both plots for better visualization. Figure 4.9 refers to the x coordinates whereas the Figure 4.10 to the y coordinates of CPs. The blue/continuous lines refer to the sensitivity derivatives, whereas the red/dashed lines to the IPE values. As it can be seen, both the IPEs and sensitivity derivatives curves follow a similar distribution and communicate the same message regarding the optimization potential(i.e the potential) of each design variable.

From the previous parametric studies we conclude that, as the NURBS parameterization becomes richer, the PE value is monotonically becoming higher. Therefore, as the number of CPs tends to the number of surface nodes, the PE value should tend to 1. Consequently, if the NURBS curves parameterization consist of, as many CPs as the nodes of the surface to be optimized, the PE value should be equal to 1. In order to examine the aforementioned, a simple case is introduced and explained in Appendix C. The geometry to be optimizez in that case consists of as many CPs as the number of surface nodes, resulting to a PE value which is practically equal to 1. This case was introduced because the airfoil used in this chapter consists of 400 nodes, and it was unrealistic to generate a NURBS curves parameterization having 400 CPs.

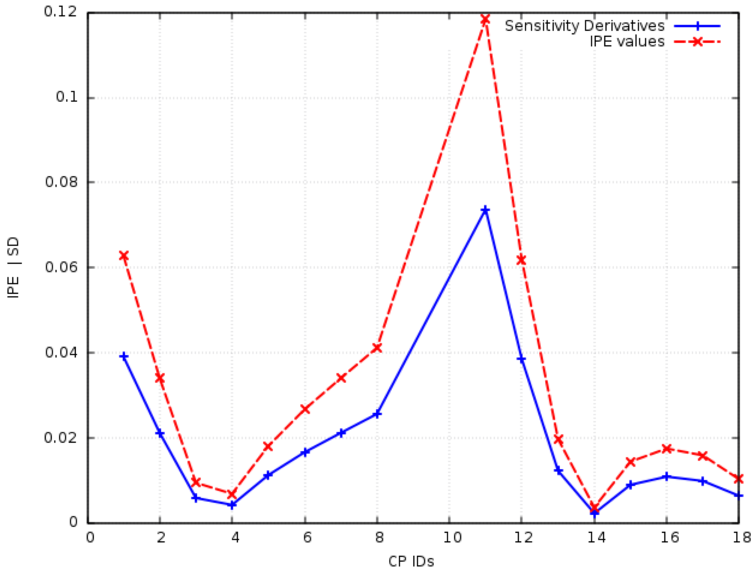

Figure 4.9: *Study 4: Comparison of the IPE values of x coordinates of CPs for Case 5 to the absolute of the corresponding sensitivity derivatives.*

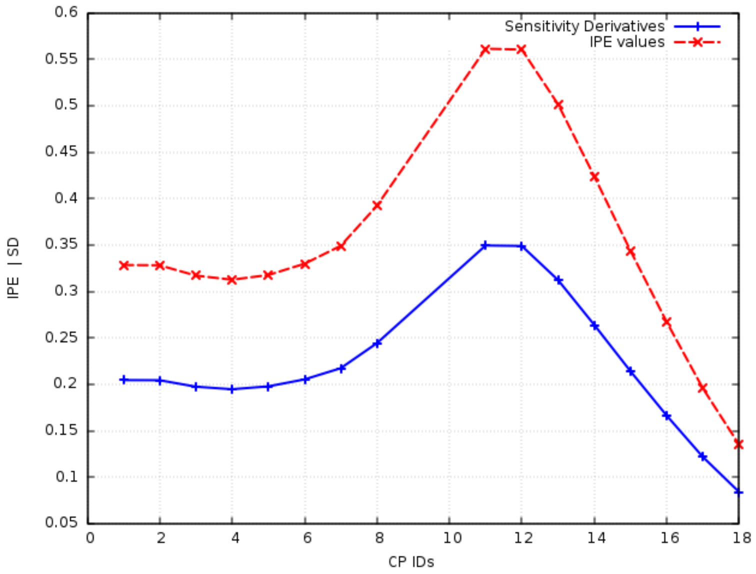

Figure 4.10: *Study 4: Comparison of the IPE values of y coordinates of CPs for Case 5 to the absolute value of the corresponding sensitivity derivatives.*

4.2 The S-bend type duct case

The duct used in this application is composed by two non-aligned straight sections, connected with a S-bend type section, which is the geometry to be optimized.

The objective function for all studies related to the S-bend type duct is the total pressure loss of the incompressible flow between the inlet and the outlet of the entire duct (not just the S-bend section). The total pressure loss is defined as the integral of the total pressures of the inlet and the outlet patches of the duct, so it is practically the difference of the two integrals. Given the different sign of the normal velocities at the inlet and the outlet, this can be written as:

$$J = -\int_{S_{i,o}} \left(p + \frac{1}{2}v_k^2\right) v_i n_i dS \tag{4.5}$$

where:

$S_{i,o}$ are the inlet and the outlet patches respectively,

p is the “kinematic pressure” (i.e.the pressure divided by the fluid’s density),

v_i is the velocity vector,

n_i is the normal unit vector (pointing outwards the inlet and outlet patch).

The flow is laminar at a Reynolds number equal to 1000. More information regarding the CFD setup and results (from the point of view of the fluid flow) can be found in section B.2. In this application, the parametric studies will be conducted using two different ways for parameterizing the S-bend section: Bezier curves and volumetric B-splines.

When Bezier parameterization is used, the upper and lower side of the S-bend section are parameterized by the best-fit algorithm based on the existing duct’s geometry (reference duct). For the purpose of this chapter’s studies, it was decided to use equal number of CPs in both sides of the duct (upper and lower), keeping the first and last CPs of each curve fixed. It must be noted that, in the following tables and figures, the number of CPs given per case is always the total number of CPs used. An example of the S-bend’s Bezier parameterization is presented in Figure 4.11. More details regarding the parameterization can be found in Appendix A.

The design variables are the x,y coordinates of the CPs that are allowed to be displaced i.e. excluding the first and last CP on each side, resulting to the total number of design variables $N_b = 2N_{CP} - 8$, where N_{CP} is the total number of CPs used per case.

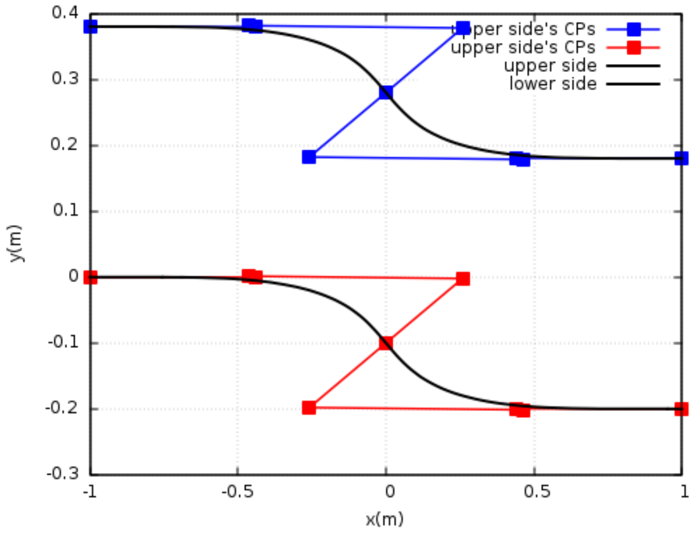

Figure 4.11: *Bezier parameterization of the S-bend curved walls using 18 CPs.*

When volumetric B-splines parameterization is used, a morphing box (which is formed by the CPs grid) is introduced, the boundaries of which enclose the S-bend section's geometry. The design variables of this application are the x,y coordinates of the morphing box's CPs, excluding the two frontmost and two rearmost morphing box's planes in the x direction which are considered fixed. Therefore, the total number of design variables is, $2N_{CP_y}\left(N_{CP_x}-4\right)$, where N_{CP_x} and N_{CP_y} are the numbers of CPs in x and y direction respectively. More information regarding the volumetric B-splines parameterization of this application can be found in Appendix A. In the following tables and figures the total number of CPs per case will be given.

Below five parametric studies are presented.

- **Study 1:** The PE values are computed and compared on the exact same geometry with 22 to 32 CPs (through enrichment) using Bezier curves. The shape is produced by the best-fit algorithm applied to the reference S-bend section's existing geometry utilizing 22 CPs. It is obvious that this shape is slightly different than the reference duct.
- **Study 2:** The PE values are computed and compared in the range of 18 to 40 CPs using Bezier curves. For each different number of CPs, a different best-fit is performed resulting to a slightly different duct.
- **Study 3:** The IPE of the design variables is computed and compared for the Cases 4 and 10 of study 2.
- **Study 4:** Computation and comparison of PE values in the range of 25 to 45 CPs by increasing the number of CPs in the x direction, using

volumetric B-splines.

- **Study 5:** Computation and comparison of PE values in the range of 25 to 45 CPs by increasing the number of CPs in the y direction, using volumetric B-splines.

Study 1

The results of the study are presented in Table 4.5 and Figure 4.12. The ”usual” increase in the PE value can be observed as CAD parameterization becomes richer. Moreover, since the geometry in all cases is identical, the values of Terms 2 and 4 remain the same since they refer to the (same) nodal parameterization. It must be noted that, the curve of Figure 4.12, although it appears to be almost linear, it has a minor curvature which leads to asymptotic convergence of the curve to a maximum PE value when a large number of CPs is used.

Case ID	CPs No	PE	Term1	Term2	Term3	Term4
1	22	0.8175	2.6683E-14	3.0362E-16	5.3993E-13	7.0457E-14
2	24	0.8234	2.3645E-14	3.0362E-16	5.1198E-13	7.0457E-14
3	26	0.8293	2.1086E-14	3.0362E-16	4.8694E-13	7.0457E-14
4	28	0.8351	1.8919E-14	3.0362E-16	4.6443E-13	7.0457E-14
5	30	0.8406	1.7072E-14	3.0362E-16	4.4410E-13	7.0457E-14
6	32	0.8459	1.5487E-14	3.0362E-16	4.2566E-13	7.0457E-14

Table 4.5: *Study 1: PE values by increasing the number of CPs.*

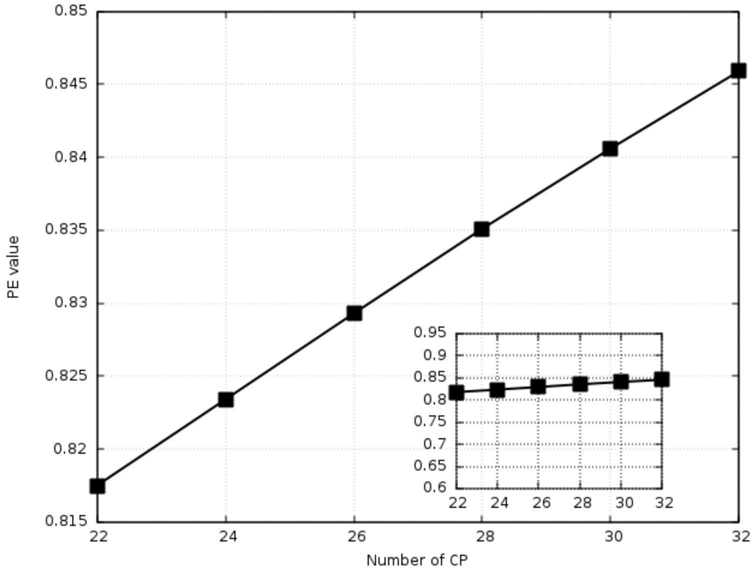

Figure 4.12: *Study 1: Results of PE values w.r.t. the number of CPs.*

Study 2

Table 4.6 and Figure 4.13 contain the results of this study. Each row of Table 4.6, corresponds to a slightly different shape of the S-bend duct. As a result the values of Terms 2 and 4 are different in every case. One may notice that with more than 18 CPs, differences are too small. In addition, despite the reduction in the values of Terms 1 and 3 as the parameterization becomes richer, their ratio becomes higher, resulting to higher PE values as well.

Case ID	CPs No	PE	Term1	Term2	Term3	Term4
1	18	0.8056	3.2619E-14	2.8521E-16	5.7074E-13	6.6246E-14
2	20	0.8133	2.8477E-14	2.8465E-16	5.3633E-13	6.5931E-14
3	22	0.8193	2.5076E-14	2.8465E-16	5.0699E-13	6.5931E-14
4	24	0.8252	2.2221E-14	2.8461E-16	4.8065E-13	6.5923E-14
5	26	0.8310	1.9818E-14	2.8461E-16	4.5714E-13	6.5923E-14
6	28	0.8367	1.7783E-14	2.8461E-16	4.3599E-13	6.5923E-14
7	30	0.8422	1.6048E-14	2.8461E-16	4.1690E-13	6.5923E-14
8	32	0.8475	1.4559E-14	2.8461E-16	3.9957E-13	6.5922E-14
9	34	0.8525	1.3273E-14	2.8461E-16	3.8379E-13	6.5922E-14
10	36	0.8573	1.2155E-14	2.8461E-16	3.6934E-13	6.5923E-14
11	38	0.8618	1.1178E-14	2.8461E-16	3.5605E-13	6.5923E-14
12	40	0.8662	1.0317E-14	2.8461E-16	3.4379E-13	6.5922E-14

Table 4.6: *Study 2: PE values by increasing the number of CPs.*

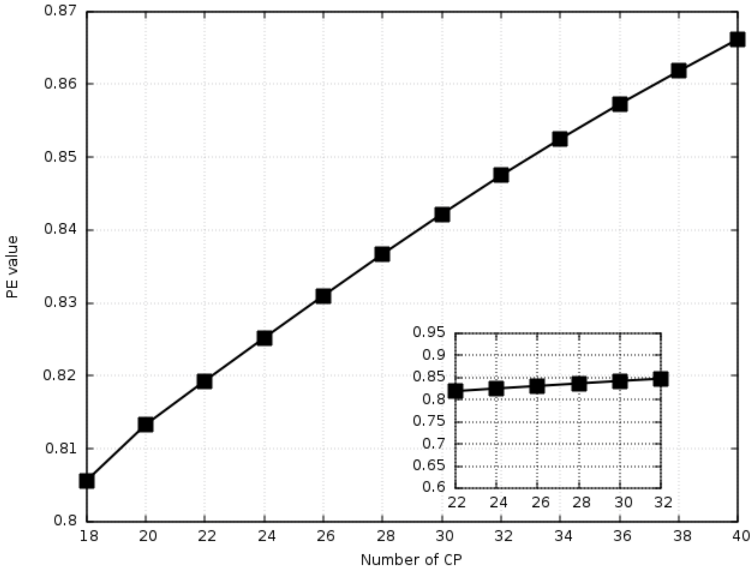

Figure 4.13: *Study 2: Results of PE values w.r.t. the number of CPs.*

From Figure 4.13, it is observed that the PE value increases simultaneously with the increase in CPs number, reaching a maximum PE value for the highest number of CPs. Moreover, the curves of Figure 4.12 and Figure 4.13, have a similar form, while the PE values in the second one, are slightly higher.

Study 3

For demonstration purposes, the IPE values of the design variables of Case 4 (24 CPs) and Case 10 (36CPs) are presented. The IPE computation follows the same approach as in Study 4 of section 4.1. The results are presented in Table 4.7, where each row refers to a certain CP, containing the IPE values of it's x and y coordinates in separate columns. The CPs IDs range from 0 to $N_{CP} - 1$, where N_{CP} is the total number of CPs used to parameterize the S-bend section, starting from the lower side's first CP to the upper side's last CP. The first half of the CPs belong to the lower side and the other half to the upper side of the S-bend. Table 4.7 contains only the CPs the coordinates of which belong to the design space, i.e the first and last CP of each curve are excluded.

In both cases, the IPE values of the y coordinates are greater than those of x coordinates, even by one order of magnitude. Therefore, the IPE distribution over the CPs will be presented separately for x and y coordinates in Figure 4.14 and Figure 4.15 respectively. The blue/continuous lines refer to Case 4, whereas, red/dashed lines to Case 10. The horizontal axis refers to the CP's ID and the vertical axis to the IPE values. Curves of both cases follow a similar distribution(for each direction x and y), where, the peak values of Case 4 are slightly higher than the corresponding ones of Case 10. The peak IPE values of CP's x coordinates appear at the 5^{th} CP and 6^{th} CP of Cases 4 and 10 respectively, whereas the peak values of CP's y coordinates appear at the 3^{rd} and 5^{th} CP of the aforementioned.

Finally, a comparison of the IPE values and the normalized absolute values of sensitivity derivatives in case 4 can be made through figures (4.16) and (4.17) which refer to x and y coordinates of CPs respectively. Due to their very small values, sensitivity derivatives are normalized with their maximum values in order to be presented in the same plot as the IPE values. The blue/continuous lines refer to the normalized CAD sensitivity derivatives while the red/dashed lines to the IPE values. It is observed that both IPEs and sensitivity derivatives follow a similar distribution and communicate the same message regarding the inportance of each design variable.

CP's ID	IPE_x	IPE_y	CP's ID	IPE_x	IPE_y
1	2.26E-02	0.300564821	1	4.07E-03	0.215656037
2	5.63E-02	0.36582825	2	1.46E-02	0.217495718
3	8.87E-02	0.424164149	3	3.47E-02	0.266548017
4	9.72E-02	0.396143389	4	6.05E-02	0.332494794
5	7.60E-02	0.281908078	5	8.29E-02	0.375507912
6	4.11E-02	0.145990014	6	9.14E-02	0.365226005
7	1.30E-02	5.17E-02	7	8.17E-02	0.299282537
8	2.04E-04	2.33E-02	8	5.88E-02	0.202717974
9	2.18E-03	5.75E-02	9	3.27E-02	0.1091514
10	5.46E-04	0.14484628	10	1.20E-02	4.14E-02
13	6.64E-03	0.28068006	11	2.33E-04	5.34E-03
14	1.24E-02	0.188967354	12	3.96E-03	2.92E-03
15	2.08E-02	0.135964591	13	3.70E-03	1.16E-02
16	3.42E-02	0.127125692	14	1.80E-03	4.63E-02
17	5.17E-02	0.163693114	15	7.36E-06	9.95E-02
18	6.76E-02	0.231709648	16	2.34E-03	0.169066168
19	7.31E-02	0.297563726	19	2.62E-03	0.274282574
20	6.32E-02	0.321235302	20	5.50E-03	0.207819218
21	4.21E-02	0.285847989	21	7.85E-03	0.154790293
22	2.02E-02	0.219828774	22	1.07E-02	0.114410032
-	-	-	23	1.51E-02	8.85E-02
-	-	-	24	2.19E-02	7.99E-02
-	-	-	25	3.15E-02	9.08E-02
-	-	-	26	4.33E-02	0.121572416
-	-	-	27	5.49E-02	0.16805587
-	-	-	28	6.28E-02	0.219744791
-	-	-	29	6.35E-02	0.260924045
-	-	-	30	5.61E-02	0.276495322
-	-	-	32	2.73E-02	0.218248082
-	-	-	33	1.49E-02	0.169854355
-	-	-	34	6.23E-03	0.138483567

Table 4.7: *Study 3: PE values of the design variables of Cases 4 and 10 of Study 2 (see Table 4.6).*

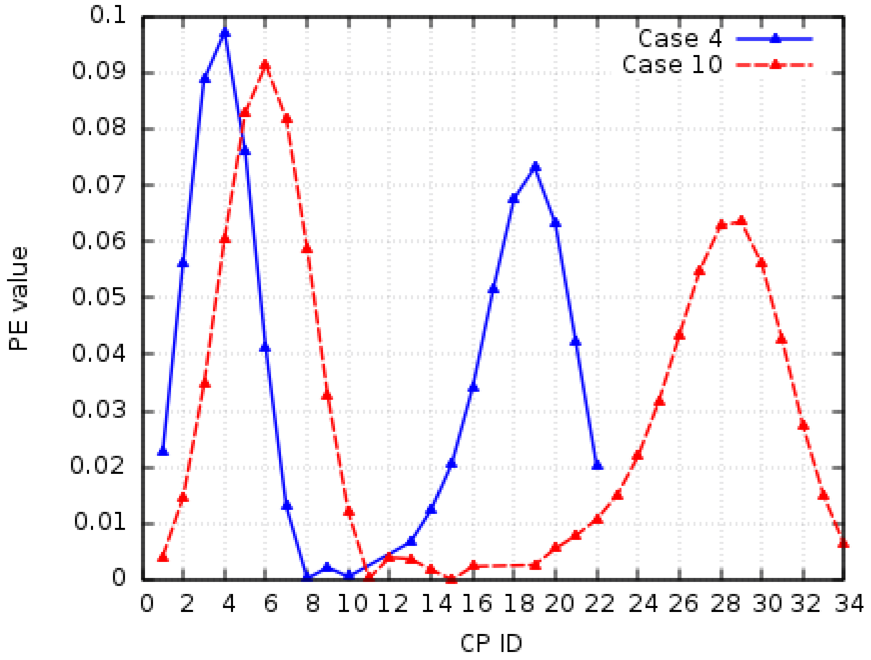

Figure 4.14: *Study 3: IPE values of each CP's x coordinate of Cases 4 and 10 of Study 2.*

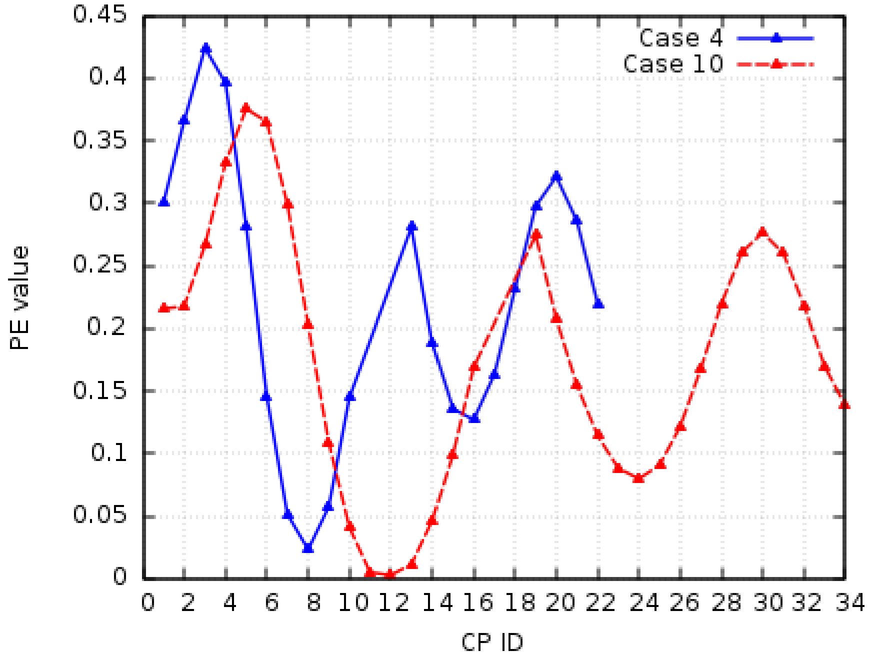

Figure 4.15: *Study 3: IPE values of each CP's y coordinate of Cases 4 and 10 of Study 2.*

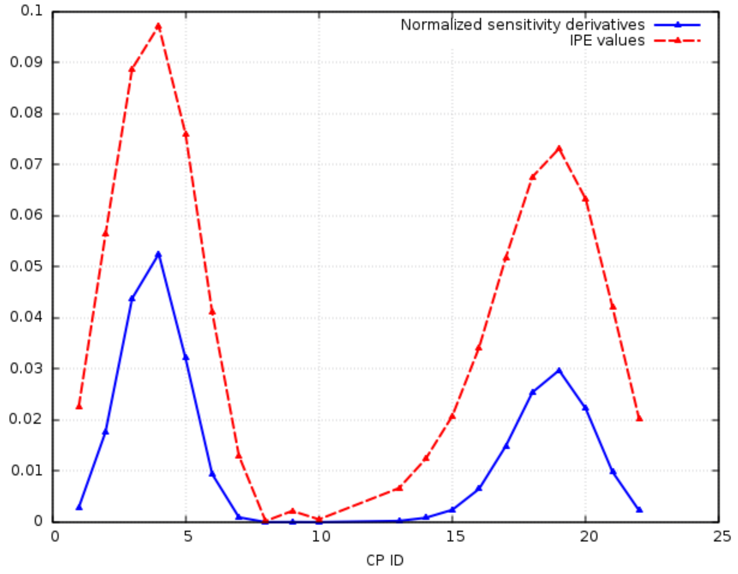

Figure 4.16: *Study 3: Comparison of IPE values of CP's x coordinates in Case 4 with the normalized absolute values of the corresponding sensitivity derivatives.*

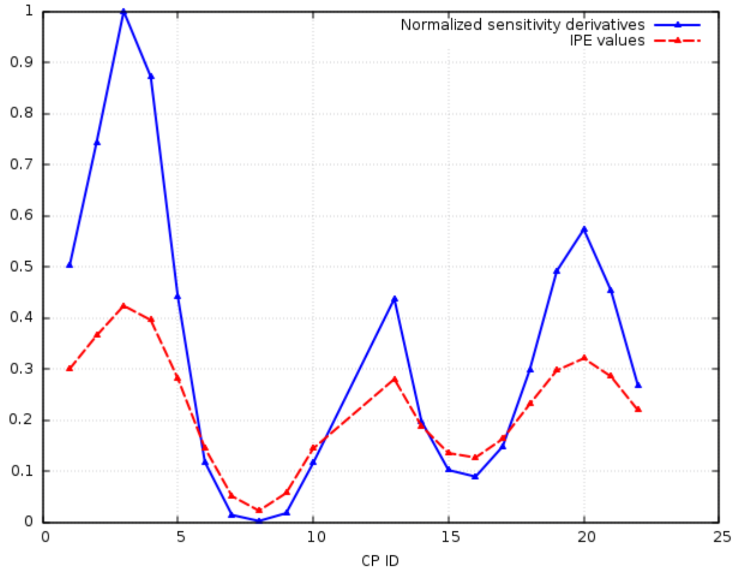

Figure 4.17: *Study 3: Comparison of IPE values of CP's y coordinates in Case 4 with the normalized absolute values of the corresponding sensitivity derivatives.*

Study 4

In this study, the distribution of volumetric B-splines CPs in the x direction varies, whereas keeping the distribution of CPs in y direction fixed. The results are presented in Table 4.8 and Figure 4.18. Each row of Table 4.8

refers to the exact same geometry, thus Terms 2 and 4 remain constant in all cases. In each case, different values of parametric coordinates are assigned at the nodes of each case, when a different number of CPs is used. It must be noted that the basis function's degree equals to 3 for both x and y directions. The PE behaviour seems to be similar with the previous studies regarding the increase in the PE value as the CPs number increases. However the increase rate of PE fluctuates as parameterization becomes richer .

Case ID	CPs No	PE	Term1	Term2	Term3	Term4
1	25	0.7262	6.6607E-17	2.8459E-16	2.3155E-14	6.5911E-14
2	30	0.7889	2.6519E-16	2.8459E-16	5.0196E-14	6.5911E-14
3	35	0.8072	3.3975E-16	2.8459E-16	5.8130E-14	6.5911E-14
4	40	0.8495	3.5171E-16	2.8459E-16	6.2245E-14	6.5911E-14
5	45	0.8545	3.2563E-16	2.8459E-16	6.0244E-14	6.5911E-14

Table 4.8: *Study 4: PE values by increasing the number of volumetric B-splines CPs.*

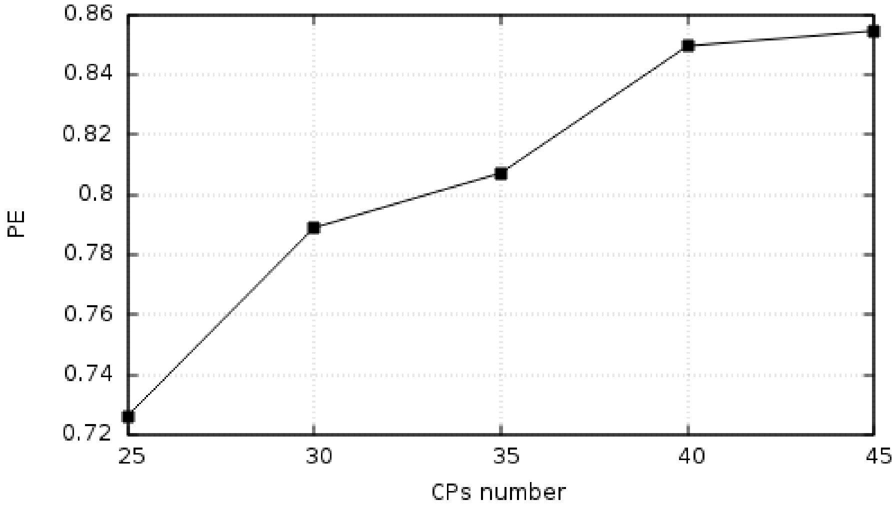

Figure 4.18: *Study 4: Results of PE values w.r.t. the number of volumetric B-splines CPs.*

Study 5

This study is the same as the previous one, however the number of CPs in the y direction is altered in each case. The results of this study are presented in Table 4.9 and Figure 4.19. Each case of this study corresponds to the same exact shape of the duct. Moreover, the parametric coordinates of each node vary between the different cases. The results of this study confirm the increase in PE as parameterization becomes richer. The PE behaviour is similar to that of Study 2 which is also confirmed by the form of the curve in Figure 4.19. It must be noted that the PE values, in most of this study's cases, are greater than the corresponding values of Study 4. Moreover, the curve of Figure 4.19, unlike the PE curve of Figure 4.18, does not seem to have turning points.

Case ID	CPs No	PE	Term1	Term2	Term3	Term4
1	25	0.7262	6.6607E-17	2.8459E-16	2.3155E-14	6.5911E-14
2	30	0.7779	6.4696E-17	2.8459E-16	2.4447E-14	6.5911E-14
3	35	0.8191	5.9531E-17	2.8459E-16	2.4694E-14	6.5911E-14
4	40	0.8586	5.5708E-17	2.8459E-16	2.5039E-14	6.5911E-14
5	45	0.8852	5.1503E-17	2.8459E-16	2.4819E-14	6.5911E-14

Table 4.9: *Study 5: PE values by increasing the number of volumetric B-splines CPs.*

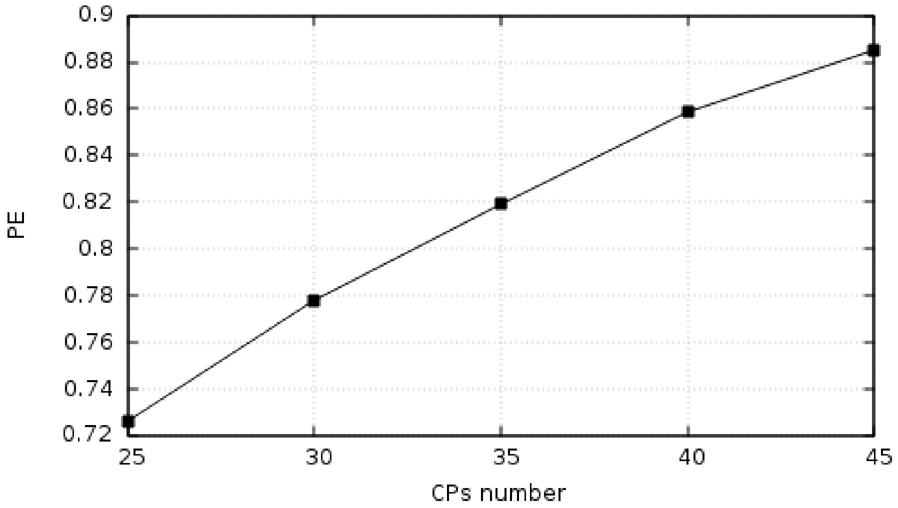

Figure 4.19: *Study 5: Results of PE values w.r.t. the number of volumetric B-splines CPs.*

4.3 The 2D compressor cascade case

In this case, the geometry to be optimized is a section of a 2D compressor cascade. Only the section of a single blade airfoil is utilized alongside proper periodic boundary conditions to properly simulate the flow. The objective function is the total pressure losses between the inlet and the outlet of the domain as explained in section 4.2.

Unlike the previous applications, here the flow is turbulent with a Reynolds number of 7.17×10^5. The inlet velocity is $48m/s$ with an inlet flow angle of −42 deg. More information regarding the CFD setup and results can be found in section B.3.

In this application, the airfoil's geometry is parameterized using NURBS curves based on the pre-designed airfoil, which will be referred as the "reference" airfoil for the rest of this section. The reference airfoil's pressure and suction sides are parameterized separately by the best-fit algorithm where the first two and last two CPs of each side are kept fixed. The latter is implemented to maintain the continuity of the curve's shape and its gradient. More details regarding the parameterization of the airfoil can be found in Appendix A.

The design variables are the x,y coordinates (axial and peripheral direction respectively) of the CPs that are allowed to be displaced (excluding the first and last two CPs of each side), resulting to a total number of design variables equal to $N_b = 2N_{CP} - 16$, where, N_{CP} is the total number of CPs. In all the studies of this application, for each different case, a different best-fit is performed resulting to slightly different geometries. An example of the blade's parameterization is presented in Figure 4.20.

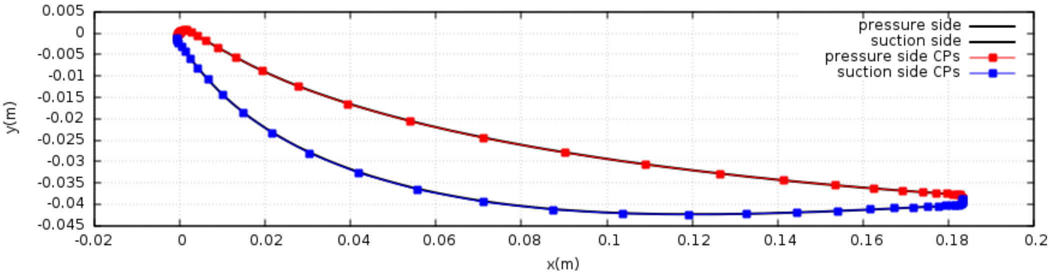

Figure 4.20: *NURBS parameterization of the blade airfoil using 50 CPs (25 on each side).*

Below four parametric studies are presented.

- **Study 1:** The PE values are computed and compared in the range of 45 to 89 CPs. In all cases of this study, the pressure side is parameterized using more CPs than the suction side (5CPs). Due to the complexity of the shape, the basis function degree is set equal to 3 in all cases for a decent representation of the airfoil.
- **Study 2:** It is the same with Study 1; though, in this study, the suction side is parameterized using more CPs (5CPs). In this study, an extra case of 95CPs is examined for better comparison with the cases of Study 1.
- **Study 3:** In this study, the PE values are computed and compared in the range of 50 to 86 CPs, using equal number of CPs to parameterize each side. Basis degree is set to 3.

- **Study 4:** It is the same study as the previous one, with basis degree equal to 5 in all cases.
- **Study 5:** The IPE values of Cases 5 and 9 of Study 1 will be computed and compared.

Study 1

The results of this study are presented in Table 4.10 and Figure 4.21. Each row of the Table 4.10, corresponds to a slightly different airfoil. In this study as a more rich parameterization is introduced in each case, the PE value increases until reaching values near 1 in the cases utilizing more than 85 CPs. It is worth mentioning that despite the fact that a large number of CPs is utilized for cases 1 to 7 the PE value remains low. Finally, as parameterization becomes richer, Term1 values are decreased, whereas Term3 values are increased, resulting to the higher PE values. However, the values of Terms 2 and 4 tend to fluctuate constantly for different number of CPs.

Case ID	CPs No	PE	Term1	Term2	Term3	Term4
1	45	0.1379	275.9931	14.3666	3.1125E+05	5.1487E+05
2	49	0.2005	219.3089	11.5526	3.4740E+05	3.9769E+05
3	53	0.3204	195.9165	12.1389	4.6126E+05	3.5832E+05
4	57	0.4561	182.2819	14.9152	6.2462E+05	3.9175E+05
5	61	0.5985	157.5966	17.5031	8.0293E+05	4.4712E+05
6	65	0.6696	156.6502	19.4599	9.6429E+05	5.0758E+05
7	69	0.7360	143.8260	20.3854	1.0627E+06	5.4361E+05
8	73	0.7997	136.3793	21.4188	1.1880E+06	5.8872E+05
9	77	0.8383	128.9954	21.7172	1.2660E+06	6.1968E+05
10	81	0.8841	121.3475	20.5264	1.2861E+06	5.9828E+05
11	85	0.9433	120.0193	19.3905	1.3341E+06	5.6850E+05
12	89	0.9721	119.9799	18.6748	1.3450E+0.6	5.4584E+05

Table 4.10: *Study 1: PE values while increasing the number of CPs.*

Study 2

This study is similar to the previous one. The only difference from the previous one is that, each case is parameterized using 5CPs extra for the suction side. The results are presented in Table 4.11 and Figure 4.22. As can be observed, a monotonic increase in PE value appears as more CPs are used to parameterize the airfoil. Particularly, when utilizing more than 90CPs the PE, tends to a value near 1. Moreover, with the increase in the CPs number, the PE terms values have a similar behaviour with the previous study.

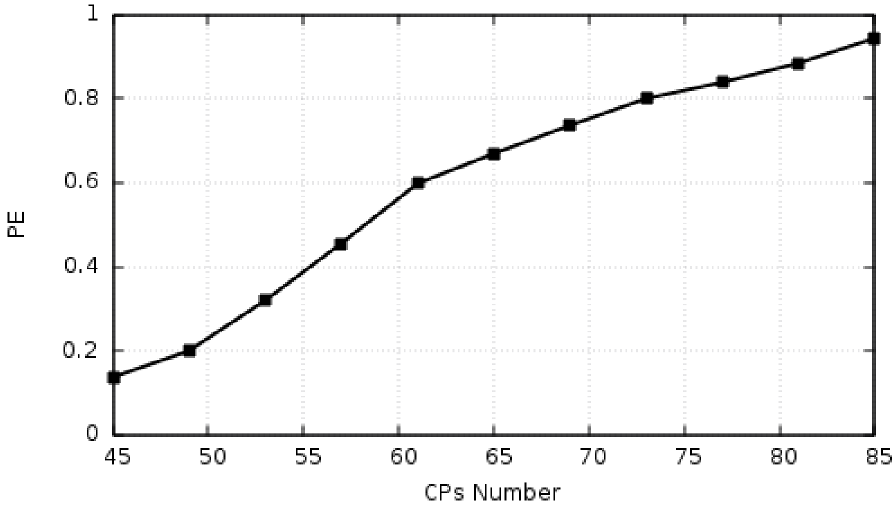

Figure 4.21: *Study 1: PE values w.r.t to the number of CPs.*

Case ID	CPs No	PE	Term1	Term2	Term3	Term4
1	45	0.2252	589.4759	13.8888	5.4680E+05	3.7266E+05
2	49	0.3052	501.5339	16.2390	7.0222E+05	4.1395E+05
3	53	0.3710	437.6374	18.2413	8.4953E+05	4.6755E+05
4	57	0.4376	382.9754	19.8402	1.0005E+06	5.2033E+05
5	61	0.4803	352.5986	21.2375	1.1252E+06	5.7492E+05
6	65	0.5157	321.7006	21.5877	1.2066E+06	6.0606E+05
7	69	0.5660	285.0782	20.9935	1.2596E+06	6.0391E+05
8	73	0.6023	277.5093	20.2117	1.3205E+06	5.9164E+05
9	77	0.6731	245.1013	18.9489	1.3391E+06	5.5318E+05
10	81	0.7624	233.0494	18.9847	1.4242E+06	5.3321E+05
11	85	0.8655	222.9479	21.8754	1.6250E+06	5.8812E+05
12	89	0.9537	204.1385	25.8147	1.8102E+06	6.7497E+05
13	95	0.9771	193.2559	29.9330	1.9476E+06	7.8447E+05

Table 4.11: *Study 2: PE values while increasing the number of CPs.*

Study 3

In each case of this study, the pressure and suction side are parameterized using equal number of CPs with a basis degree of the NURBS curves equal to 3. The results of this study are presented in Table 4.12 and Figure 4.23.Likely the previous studies, each row of Table 4.12 corresponds to a slightly different blade's shape. Each shape is parameterized with the same number of CPs for its pressure and suction side using a basis degree for NURBS curves equal to 3.

In this study, the behaviour of the PE is similar to that of the previous two

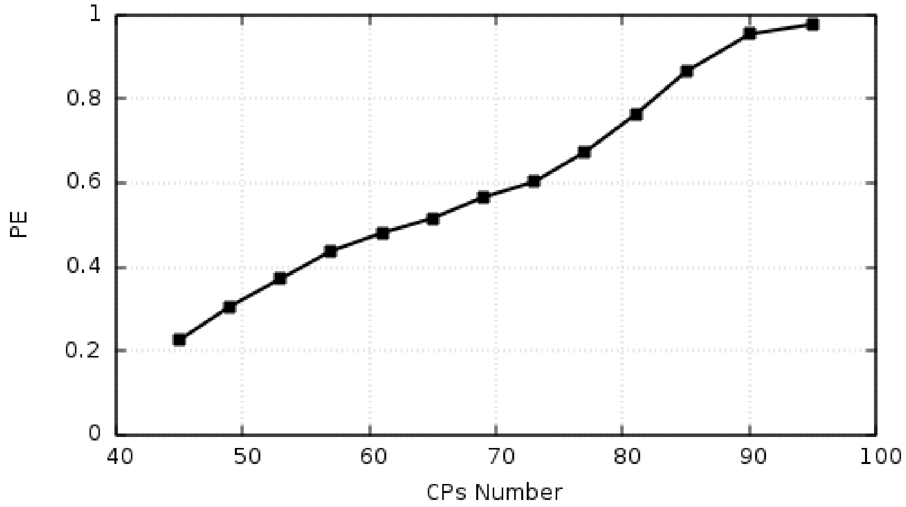

Figure 4.22: *Study 2: PE values w.r.t to the number of CPs.*

cases, reconfirming thus the increase in PE values w.r.t. the CPs number. Thus, the curve of Figure 4.23 has a similar shape with those of figures Figure 4.21 and Figure 4.22.

Case ID	CPs No	PE	Term1	Term2	Term3	Term4
1	50	0.3407	254.8337	13.8157	5.4468E+05	3.7220E+05
2	58	0.5390	214.5645	18.5156	8.7399E+05	4.7636E+05
3	66	0.6614	191.0240	21.0249	1.1321E+06	5.6786E+05
4	74	0.7088	180.9139	21.0261	1.2604E+06	6.0620E+05
5	82	0.8235	167.1745	19.1705	1.3611E+06	5.5970E+05
6	86	0.9101	162.7588	19.0623	1.4282E+06	5.3706E+05

Table 4.12: *Study 3: PE values while increasing the number of CPs.*

Study 4

All the airfoils of this study are parameterized using equal number of CPs in both sides. The only difference compared to the previous study is the fact that the basis degree of NURBS curves equals to 5. Table 4.13 and Figure 4.24 include the study's results. Unlike all the previous studies regarding this application, the PE curve of Figure 4.24, does not increase monotonically as CPs number increases. In fact, when the CPs number exceeds 74, PE values are slightly reduced tending to a value of 0.6. All the aforementioned are mainly due to the fact that the basis degree used for the NURBS curves, equals to 5, which increase the complexity of the problem as more CPs may affect each node of blade, limiting the values of PE when a large CPs number is used.

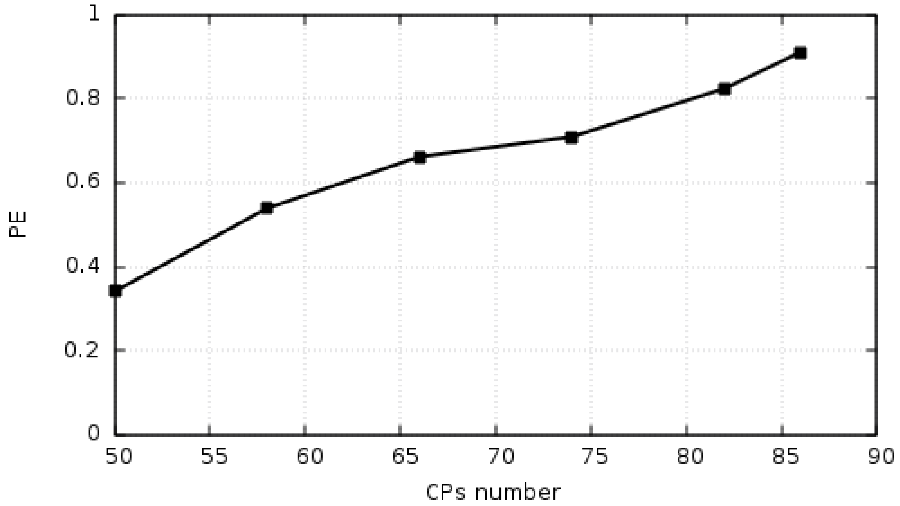

Figure 4.23: *Study 3: PE values w.r.t to the number of CPs.*

Case ID	CPs No	PE	Term1	Term2	Term3	Term4
1	50	0.3210	229.8595	21.8510	6.8486E+05	6.5783E+05
2	58	0.4617	193.2732	18.1136	7.8214E+05	5.1859E+05
3	66	0.5591	171.9396	17.7068	8.5944E+05	4.9329E+05
4	74	0.6335	155.4414	22.7134	9.9746E+05	6.0189E+05
5	82	0.6242	139.7784	27.9312	1.0936E+06	7.8313E+05
6	86	0.6258	131.9050	28.4894	1.1106E+06	8.2477E+05

Table 4.13: *Study 4: PE values while increasing the number of CPs.*

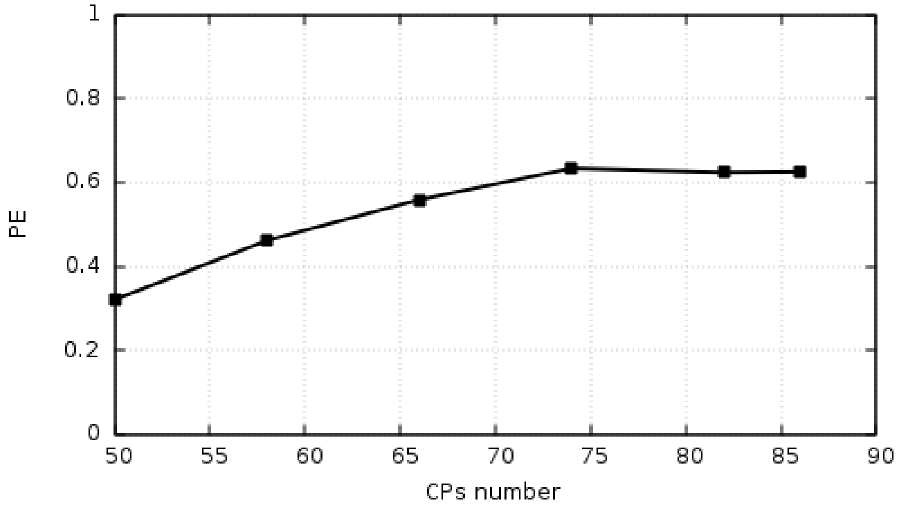

Figure 4.24: *Study 4: PE values w.r.t to the number of CPs.*

In Figure 4.25, the PE curves of Studies 1 and 2 are compared. The blue/continuous line refer to Study 1, whereas the red/dashed line to Study 2. First of all, the curves do not have a similar form. In addition, for the parameterizations utilizing 57 CPs and more, the PE values of Study 1 are generally greater compared to the corresponding cases of Study 2. The opposite applies for the parameterizations with less than 57 CPs.

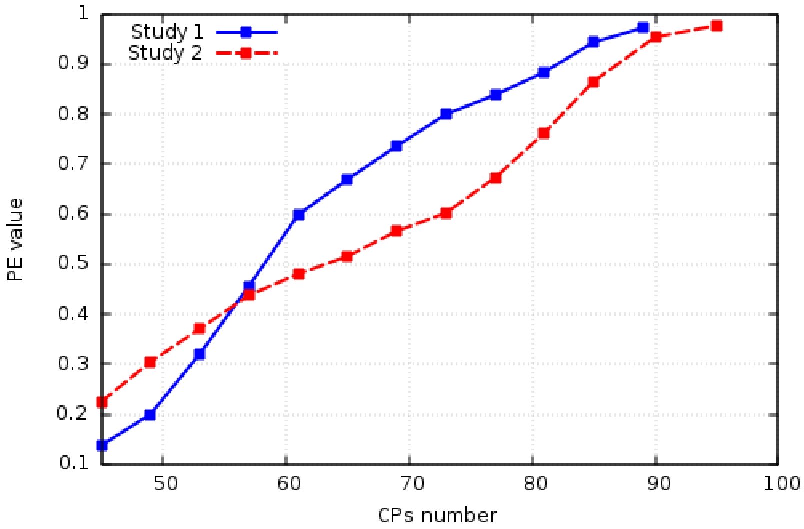

Figure 4.25: *Comparison of PE values of Studies 1 & 2.*

In Figure 4.26, the PE curves of Studies 3 and 4 are compared. The blue/-continuous line refers to Study 3, whereas, the red/dashed line to Study 4. As it can be observed from Figure 4.26 all PE values of Study 3 are greater than those of Study 4. The latter is due to the fact that, in all cases of Study 4, more CPs have impact at each node of the geometry, which limits its PE value.

Study 5

In this study, the IPE values are presented for Cases 5(61CPs) and 11(85Cps) of Study 1. It is reminded that, the pressure side is parameterized using 5 more CPs than the suction side. The CP IDs range from 0 to $N_{CP}-1$, where N_{CP} is the total number of control points. For Case 5, the CPs whose IDs range from 0 to 27 refer to the pressure side while the CPs IDs ranging from 28 to 60 refer to the suction side. In Case 11, CPs from 0 to 44 refer to the pressure side whereas 45 to 84 refer to the suction side. The IPE values corresponding to the x and y coordinates of the CPs that are allowed to be displaced are plotted separately.

The IPE w.r.t. the x and y coordinates are presented in Figure 4.27 and

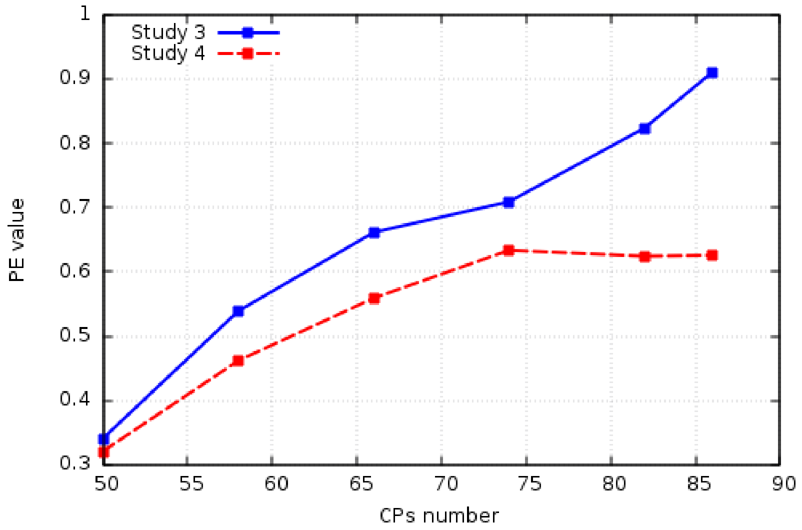

Figure 4.26: *Comparison of PE values of Studies 3 & 4.*

Figure 4.28 respectively. It is worth mentioning that, unlike the previous applications, the peak IPE values of the x coordinates are greater that the peak values of y coordinates in both cases. The peak value of Case 5 in Figure 4.27 can be found at the 35^{th} CP which is the 8^{th} CP of the suction side corresponding to $(x, y) = (0.0139, -0.0179)$. The peak value of Case 11 in Figure 4.27 can be found at the 47^{th} CP which is the 3^{rd} CP of the suction side corresponding to $(x, y) = (-0.000472, 0.00176)$. The peak value of Case 5 in Figure 4.28 is at the 9^{th} CP of its suction side corresponding to $(x, y) = (0.0241, -0.025)$, whereas the peak value of Case 11 can be found at the 3^{rd} CP of its suction side.

The CPs with the greatest impact on the optimization potential of the two cases are located at different coordinates, which means that they affect different regions of the airfoil. As a conclusion, the PE value and the optimization potential in this application relies heavily on the distribution of CPs around the airfoil.

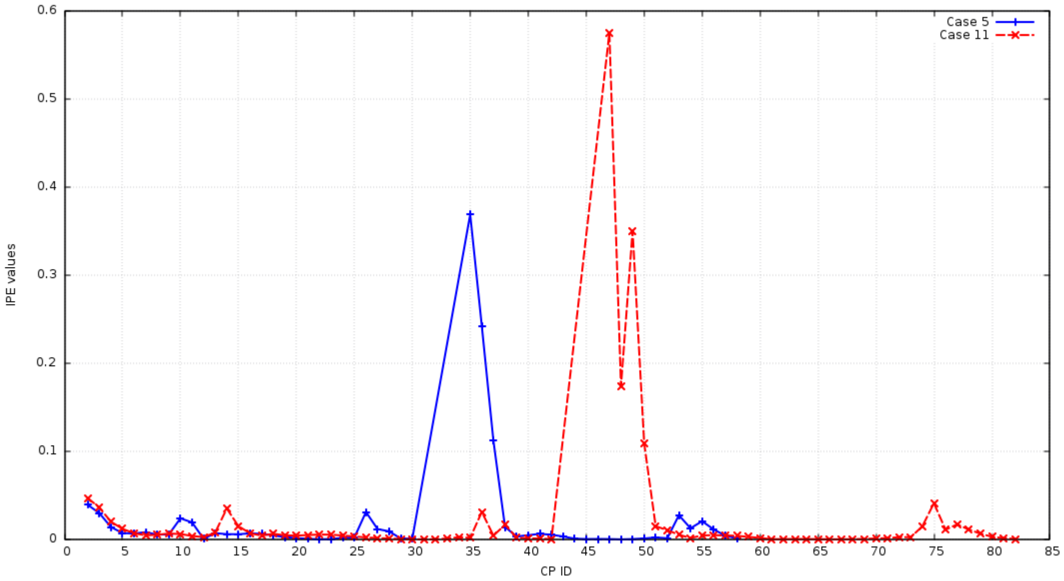

Figure 4.27: *IPE values of Cases 5 & 11 CP's x coordinates.*

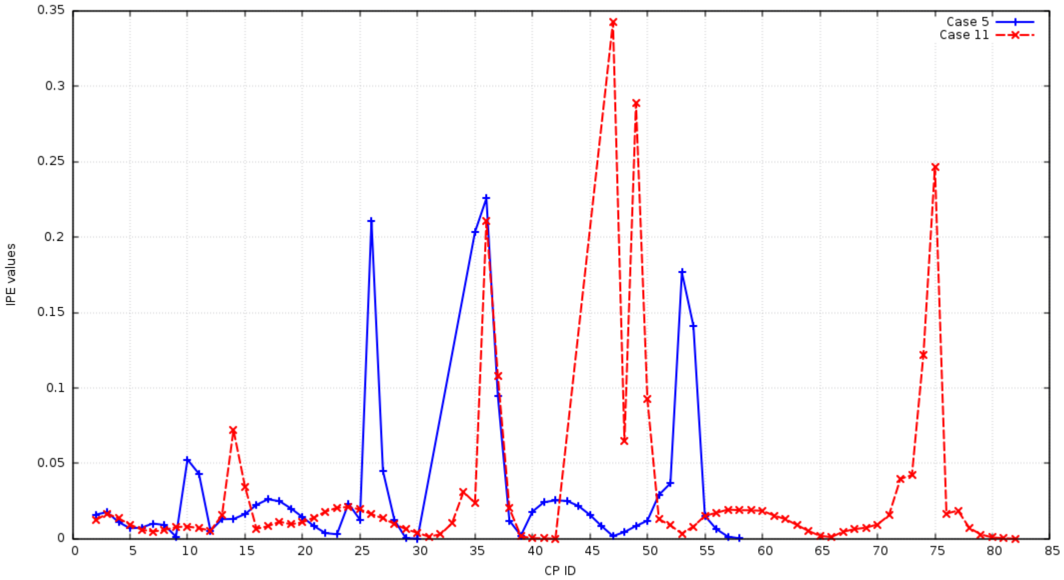

Figure 4.28: *IPE values of Cases 5 & 11 CP's y coordinates.*

Chapter 5

The PE into the optimization loop

In this chapter, the PE will be studied from the perspective of the optimization, based on the results of chapter 4. Various optimization loops are conducted for all three applications, the results of which are compared by also considering the corresponding PE values. Furthermore, the evolution of PE during the optimization loops of each application of chapter 4 is studied and presented too.

5.1 Optimization of the isolated airfoil

Aerodynamic shape optimization loops are performed for different parameterizations of the isolated airfoil as introduced in section 4.1. The evolution of PE during the optimization loop is recorded. Finally, optimization loops using different combinations of design variables based on their IPE values are performed.

5.1.1 Optimization using different parameterizations

Three cases are presented and compared, the geometries of which are parameterized using NURBS curves with a different PE value each. The objective function for all cases is the drag coefficient (C_D). More details regarding the objective function and the flow characteristics can be found in section 4.1.

The airfoils of Cases 1 and 2 are parameterized by performing a different best-fit, based on the reference airfoil (section 4.1), using 14 and 20 CPs respectively, where the differences in the reconstructed shapes are minor. Moreover, the airfoil of Case 3 is produced through enrichment of the parameterization of the airfoil of Case 1 i.e. with 20 CPs in total. As a result, the geometries of Cases 1 and 3 are identical.

Prior to running the optimization loop, it is important to introduce some constraints in order to obtain a feasible solution regarding the airfoil's shape and avoid a potential termination of the optimization procedure due to the overlapping of the pressure and suction sides of the airfoil or the grid's nodes due to their displacement. It must be noted that, these are applied in all cases of this section.
The constraints are listed below:

- The maximum reduction in the airfoil's surface area, compared to the reference one, is set to 15%.
- The maximum allowed difference in lift coefficient (C_L) from the initial value is set to ± 0.0001.
- The moment coefficient (C_m) value is bounded to $\pm 1 \times 10^{-4}$, so that the optimized airfoil is also trimmed.
- The first and last two CP's over both sides of the airfoil remain fixed during the entire optimization loop, in order to enforce C1 continuity of the leading edge and avoid the overlapping of the pressure and suction sides at the trailing edge.

The design variables are the x,y coordinates of the CPs which are not fixed, resulting to the total number of design variables to be $N_b = 2N_{CP} - 16$, where N_{CP} is the total number of CPs used to parameterize the airfoil.

The results are presented in Table 5.1 and Figure 5.1. Each row of Table 5.1 contains the total number of CPs used to parameterize the airfoil (N_{CP}), the total number of design variables (N_b), the initial & final values of the objective function(J_{intial},J_{final}), the normalized final value(J_{final}^{normal}), and finally the associated PE value (of the initial geometry) of each case.

In Figure 5.1, the minor differences in the initial shape of Cases 1 and 2 airfoils reflect on their initial $J\left(C_D\right)$ values as well. Moreover, since this chapter focuses on the optimization potential of each case, Figure 5.1 presents the normalized objective function values of each.

What can be seen from Table 5.1 and Figure 5.1, is that, as the PE increases, the optimization potential of the airfoil is increasing too. However the differences in the objective function between the optimized airfoils are minor due to the constraints applied in each case (which were necessary in order to avoid the overlapping of the two sides). The same applies for each optimized airfoil and their corresponding initial ones. As a result, the maximum reduction in the objective function (that of Case 2) is about 3.6% and the relative difference between Case 1& 2 optimized airfoils is about 0.1%. In addition, the optimization loop of each case, practically converges in the first four cycles, which is due to the strict constraints applied in this application. Especially, in Case 3, the objective function and the constraints are all converging by the end of the 4^{th} optimization cycle. In Cases 1 and 2, the differences in the objective function after the 4^{th} cycle are minor and the next optimization cycles are needed only in order to meet the constraint.

Case No	NCP	Nb	J_{init}	J_{final}	J_{final}^{normal}	$PE_{initial}$
Case 1	14	12	0.060280	0.058166	0.96492	0.67100
Case 2	20	24	0.060290	0.058118	0.96397	0.72542
Case 3	20	24	0.060280	0.058122	0.96420	0.71485

Table 5.1: *Isolated airfoil optimization: Optimization results of Cases 1,2 and 3.*

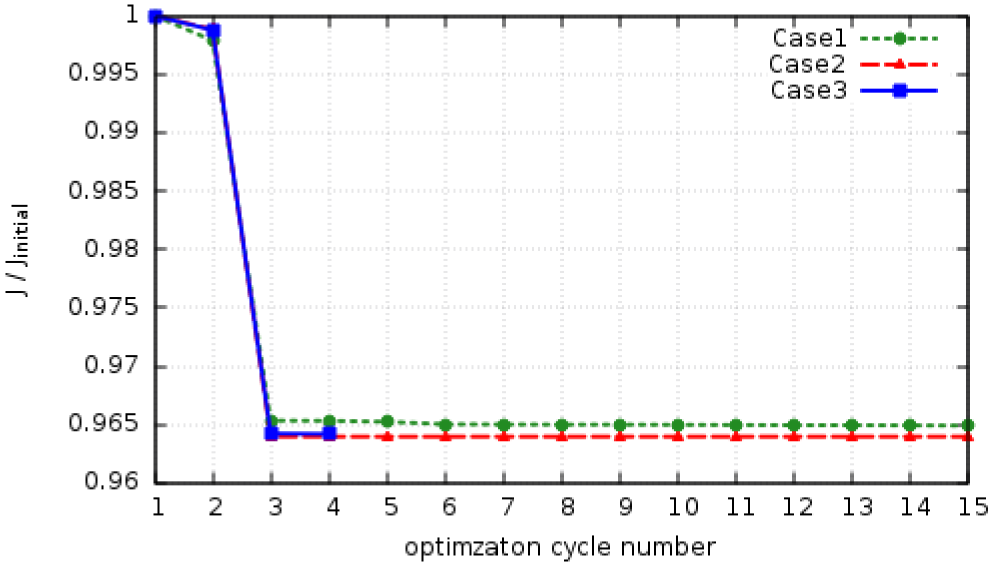

Figure 5.1: *Isolated airfoil optimization: Normalized objective function values during the optimization procedure of Cases 1,2 and 3.*

During the previous chapters, all cases where associated with a single PE value (the initial one). However during the optimization loop, as the airfoil's shape changes and the design variables are updated in each cycle, the PE values are changed too. Therefore, PE values are computed for certain cycles of each case. In Cases 1 & 2, PE is computed for optimization cycles: 1,3,6 and 10, whereas in Case 3 for cycles: 1, 3 and 4. The evolution of the PE during the optimization procedure is presented in Figure 5.2. It is observed that, during the optimization, the PE values are reduced by up to 36%, while the PE curves are similar in all cases. Case 2 curve maintains the highest value, followed by that of Case 3 and finally by the curve of Case 1.

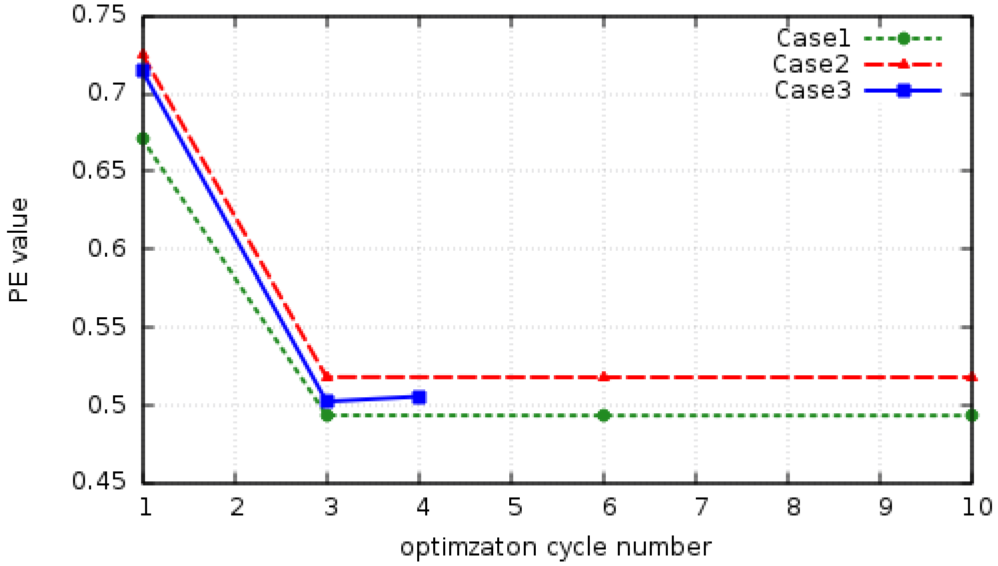

Figure 5.2: *Isolated airfoil optimization: Evolution of the PE values during the optimization.*

The optimized geometries of each case are presented in Figure 5.3. Each sub-figure contains the optimized shape drawn with continuous lines, and the initial shape of each case with the dashed lines.

The flow fields (velocity's magnitude and kinematic pressure) of each case are presented in figures 5.4 to 5.6 for Cases 1,2 and 3, respectively. Each figure presents the flow fields of the optimized geometry (bottom), accompanied by the flow fields of their initial airfoil (top). Velocity fields are placed on the left, whereas the pressure fields are placed on the right of each figure. As it can be seen, in all cases the wake of the optimized geometries is slightly reduced compared to that of their initial shape. Moreover the low pressure area at the airfoils suction side is also reduced, resulting to a reduction of the pressure drag (as the airfoil is placed at a 2 deg angle to the far-field velocity according to section 4.1). Finally, the area around the leading edge(stagnation point) of the airfoil is limited in the optimized geometries fields, leading to a further decrease in drag. All the optimized shapes induce similar aerodynamic phenomena as their shapes differences are minor which also validates the minor differences in the results of the optimization.

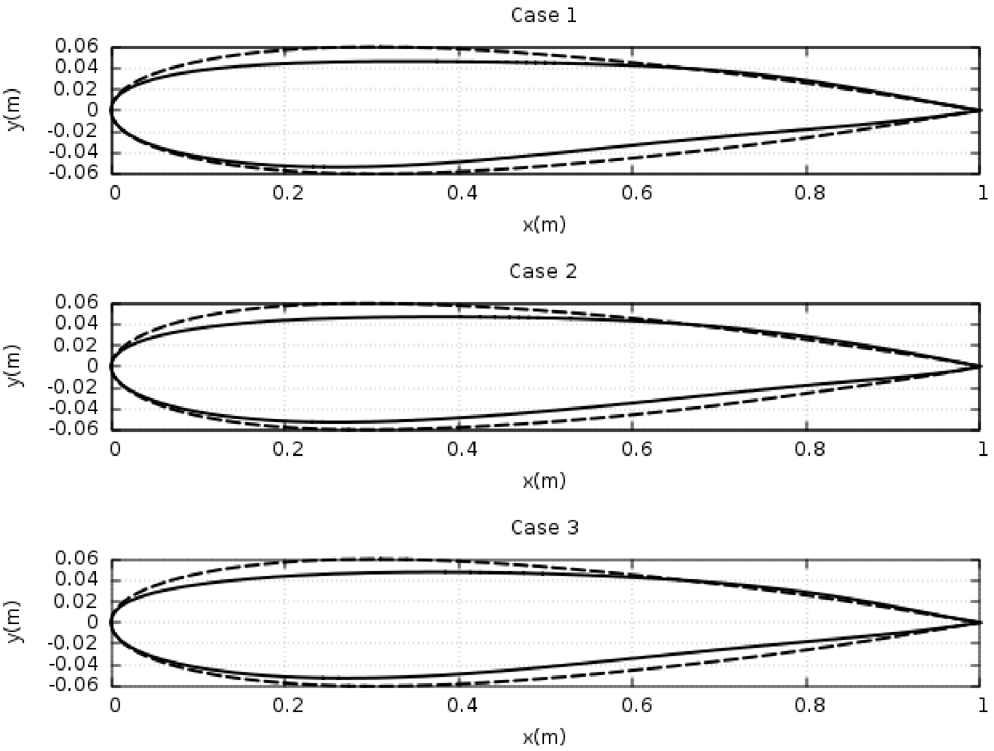

Figure 5.3: *Isolated airfoil optimization: The shape of the optimized airfoil of each case compared its corresponding initial one.*

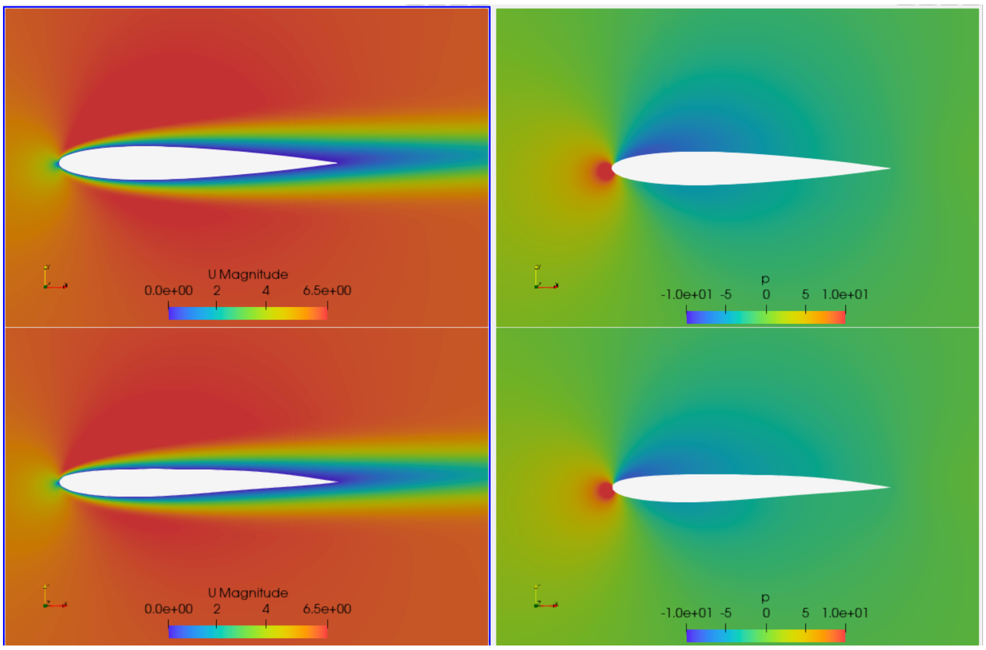

Figure 5.4: *Isolated airfoil optimization: Flow fields around Case 1 initial(top) and final(bottom) geometry.*

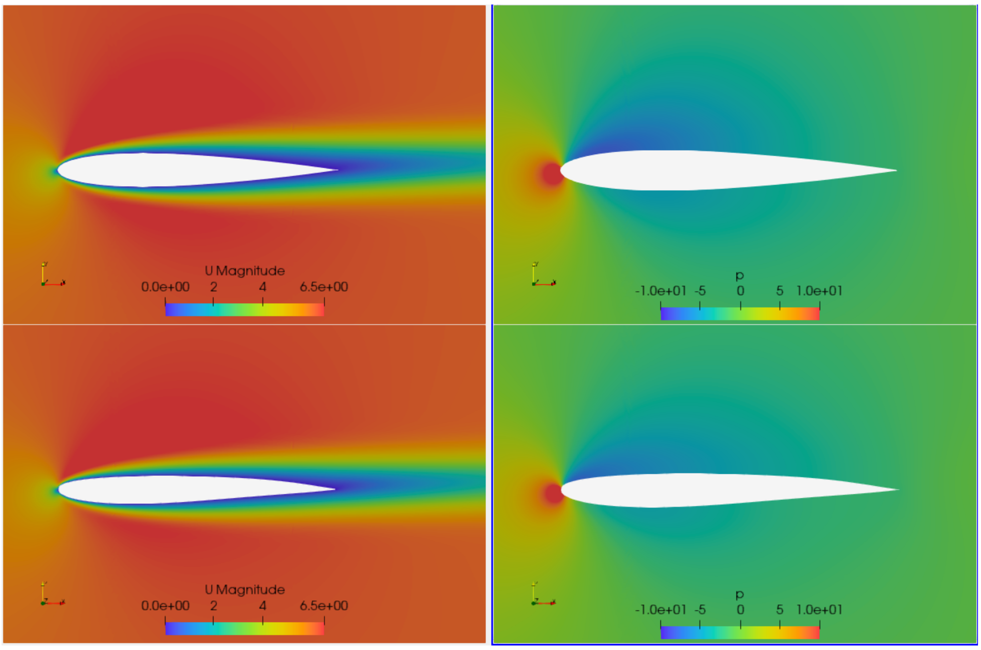

Figure 5.5: *Isolated airfoil optimization: Flow fields around Case 2 initial(top) and final(bottom) geometry.*

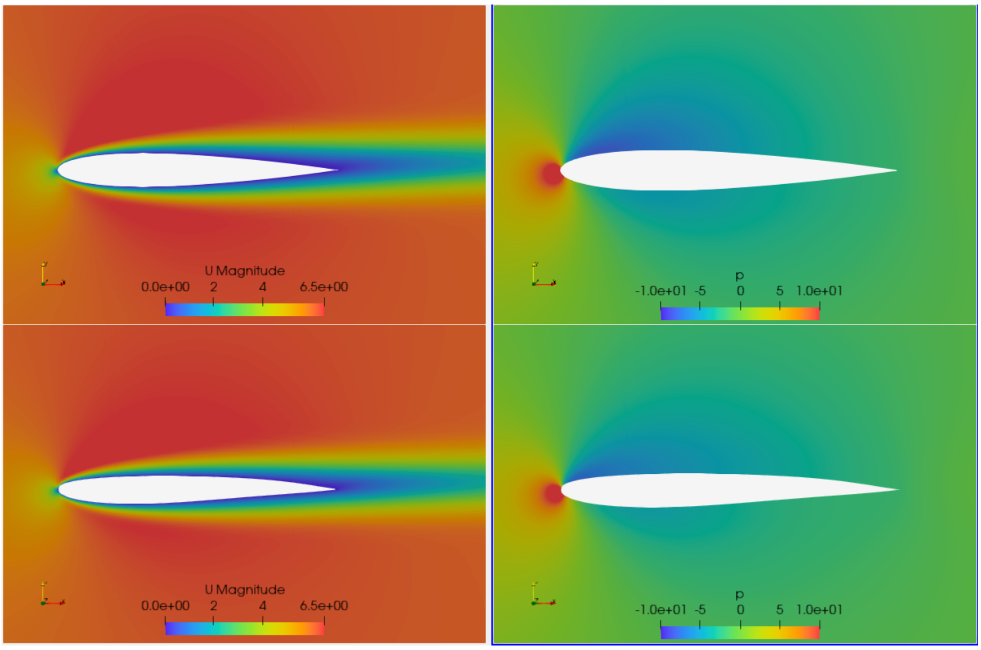

Figure 5.6: *Isolated airfoil optimization: Flow fields around Case 3 initial(top) and final(bottom) geometry.*

5.1.2 Optimization using selected design variables

The airfoils of Cases 1 and 2, are optimized by selecting only the five most effective design variables from the IPE values of the aforementioned cases. The design variables with the highest optimization potential in each case are:

- **Case 1:** The y coordinates of the $2^{nd}, 3^{rd}, 4^{th}, 9th$ and 10^{th} CP.
- **Case 2:** The y coordinates of the $7^{th}, 12^{th}, 13^{th}, 14^{th}$ and 15^{th} CP.

It is reminded that CPs IDs range from 0 to $N_{CP} - 1$, where the first half refer to pressure side and the second half to the suction side.

The importance of each design variable is shown in Figure 5.7 which is formed by the IPE values of each case. Each part of the pie-chart figure corresponds to a single design variable, the size of which is proportional to its IPE value. The most important design variables are marked with red colour, and as it can be seen in both cases they occupy more than half of each pie-chart's area.

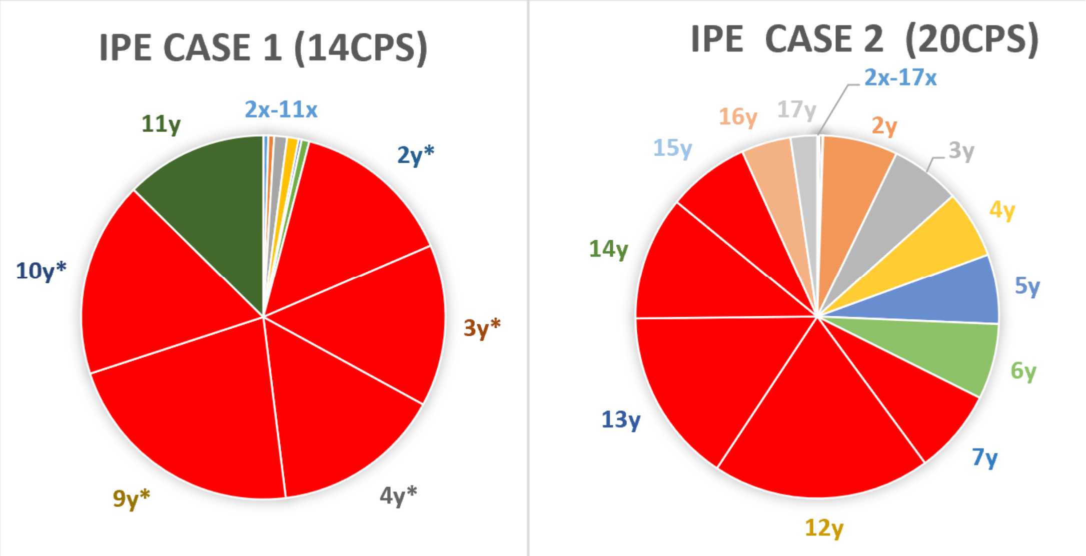
IPE CASE 1 (14CPS)

IPE CASE 2 (20CPS)

Figure 5.7: *Isolated airfoil optimization: Comparison of the design variables importance of Cases 1 and 2.*

The results are presented in Table 5.2 and Figure 5.8. In Table 5.2, the optimization results of each case when using all design variables are denoted by J_a, whereas the results of using only the most effective design variables of each case as J_i. The blue/continuous line of Figure 5.8 refers to Case 1, whereas the red/dashed line to Case 2. As it can be observed, the most important design variables of Case 1 result to a lower objective function value compared to those of Case 2. The result is verified through Figure 5.7, where the IPE values of Case 1 most important design variables occupy a larger area in their pie-chart than these of Case 2. In addition to it's better solution, Case 1 converges significantly faster as it reaches it's final value by the end of the 7^{th} cycle compared to Case 2 which convergences after 15 optimization cycles. Also, the final solution of Case 1 J_i, is also better compared to its J_a. The latter is maybe due to the fact that the gradient base optimization when all the CPs (that are allowed to move) are used as design variables the solution may converge to a local minimum resulting to a slightly increased value of drag. On the contrary the last does not happen in Case 2, where the optimization using only the most important parameters converges to a higher value of drag. The aforementioned can be observed also from Figure 5.9.

Case ID	$J_{initial}$	$J_{a_{final}}$	$J^{normal}_{a_{final}}$	$J_{i_{final}}$	$J^{normal}_{i_{final}}$
Case 1	0.06029	0.05817	0.96499	0.05817	0.96476
Case 2	0.06029	0.05812	0.96397	0.05833	0.96755

Table 5.2: *Isolated airfoil optimization: Optimization results of the Case 1 &2 airfoils using only the 5 most effective design variables in optimization.*

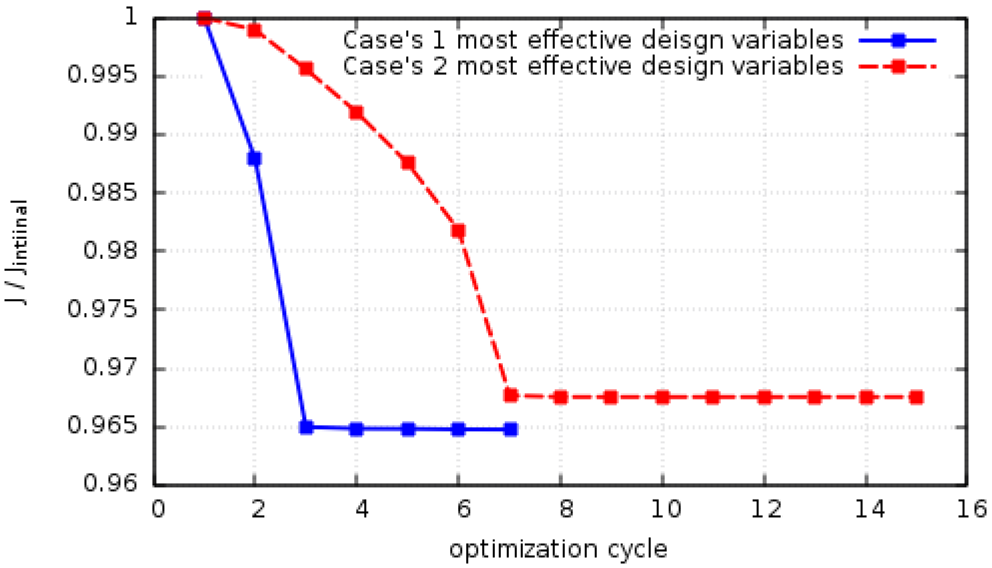

Figure 5.8: *Isolated airfoil optimization: Objective function values during the optimization of the Case 1 &2 airfoils using only the 5 most effective design variables.*

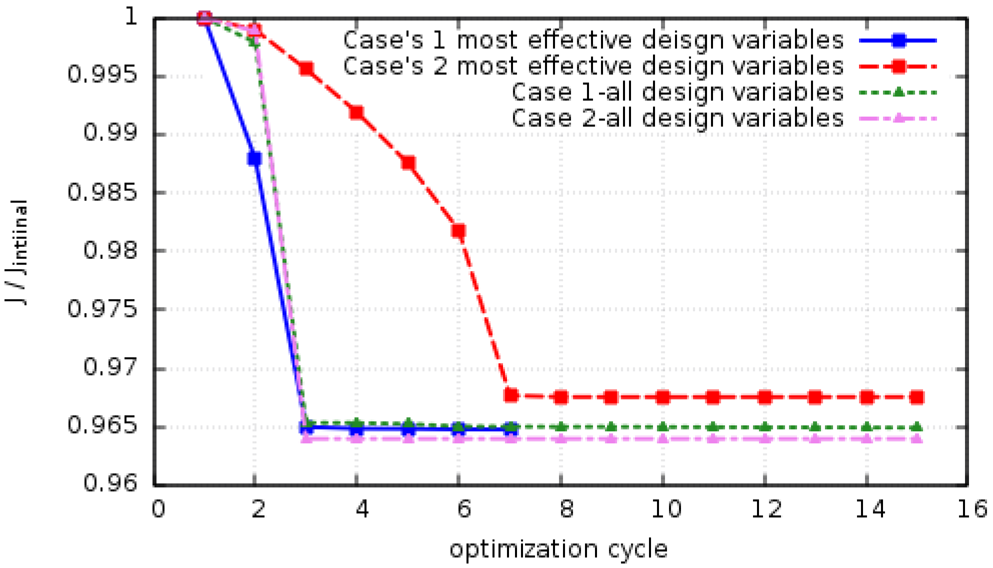

Figure 5.9: *Isolated airfoil optimization: Comparison of Cases 1 & 2 when the most important design variables are used with that of Cases 1 & 2 with all the design variables.*

5.1.3 Optimization using only the x or y coordinates

The figures 4.7 and 4.8 of section 4.1, indicated that the IPE values of the y coordinates are significantly greater that those of the x coordinates in both cases of figures 4.7 and 4.8. Due to the latter, two cases are introduced (Case 4 and Case 5), where two optimization loops will be performed. Both cases utilize the same airfoil, that of Case 2 in subsection 5.1.1 and all the constraints mentioned above. The design variables in Case 4 are considered to be only the x coordinates of the CPs which are allowed to displace, whereas Case 5 utilizes only their y coordinates. The results of each case alongside those of Case 2, are presented and compared in Table 5.3 and Figure 5.10, where only the normalized final values of objective function will be included as the initial geometry is identical.

Case ID	J_{final}^{normal}
Case 2	0.9639707
Case 4	0.9629773
Case 5	0.9645456

Table 5.3: *Isolated airfoil optimization: Comparison of optimization results of Cases 2 and 4(x coordinates) and 5 (y coordinates).*

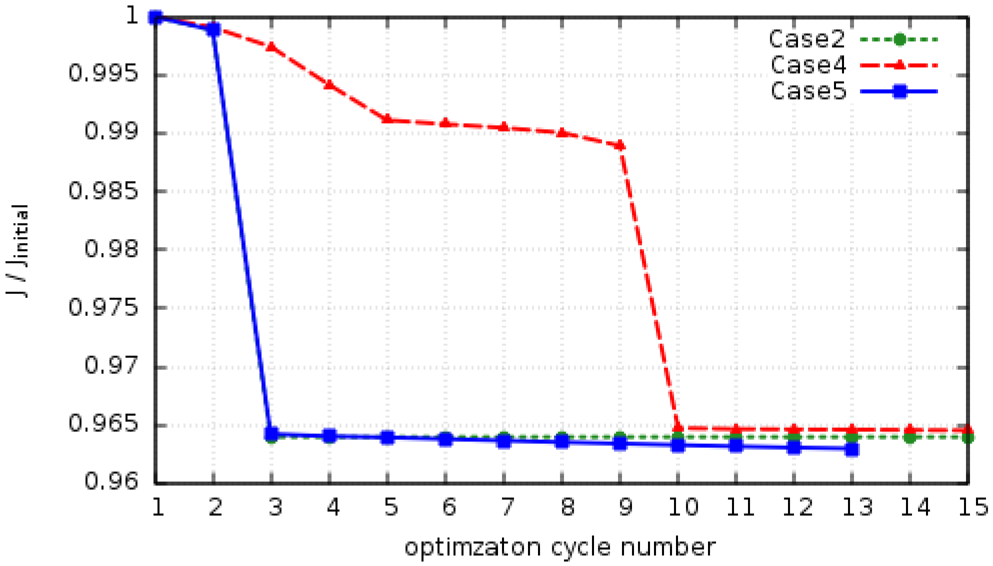

Figure 5.10: *Isolated airfoil optimization: Comparison of objective function values of Cases 2, and Cases 4(x coordinates) & 5 (y coordinates).*

5.1.4 The impact of the C_m constraint

In Figure 5.11 the results of the optimization loop with and without the C_m constraint are compared. The blue/continuous line refers to the Case 2 optimization(with C_m) and the red/dashed line to Case 2 (C_m is not used). As can be seen the introduction of the constraint reduces the objective function and reduces the convergence time too. However, after the third cycle, it seems that the optimization is restrictive in terms of further drag reduction, as the latter practically remains the same until the convergence of the constraints in the 15^{th} cycle.

5.2 Optimization of the S-bend duct

The S-bend duct introduced in the previous chapter is optimized using two different parameterization methods, Bezier curves and volumetric B-splines. Firstly, various optimizations are performed using Bezier curves in order to identify the relation of PE and the optimization potential of the duct's shape. Moreover, four optimizations are conducted using different parameterizations (Bezier and volumetric B-splines) which are associated with different PE values. Finally, an optimization case using the x and y coordinates separately as design variables is conducted to study the importance of each in an optimization loop, see of Figure 4.14 and Figure 4.15.

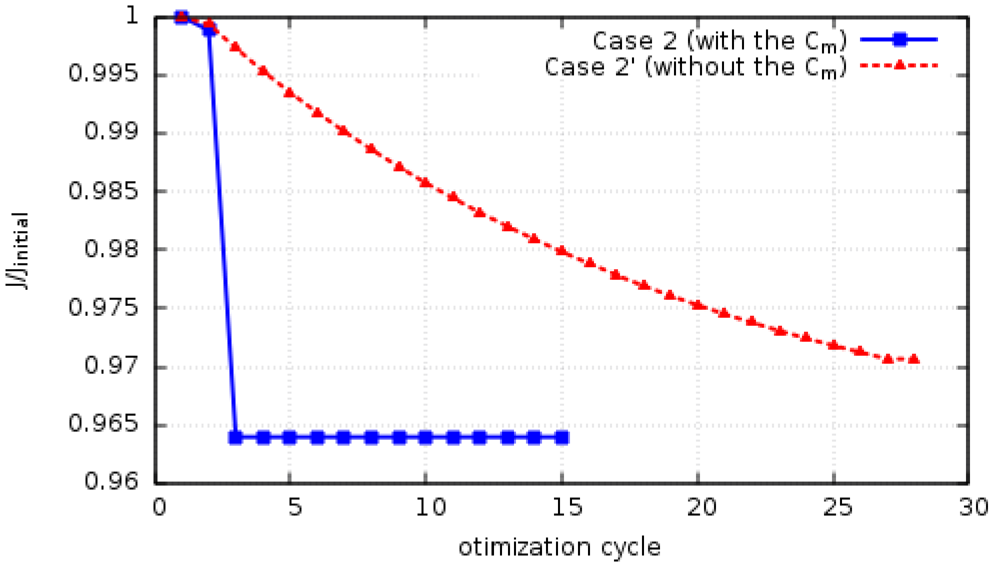

Figure 5.11: *Isolated airfoil optimization: Comparison of Case 2 results with and without the C_m constraint.*

In this application, the only constraint imposed is that the first and last two CPs of each side of the S-bend section, are fixed during the optimization when Bezier parameterization is used, in order to maintain continuity of the shape, and the derivative of each sides's curve at their first and last node. Similarly, the first two and last two lines of the morphing box, in the x-direction are kept fixed.

5.2.1 Relation of PE and duct's optimization potential

A parametric study is presented regarding the relation of PE with the optimization potential of each parameterization. For that reason, various optimization loops are performed using Bezier curves with different number of CPs. The CPs number ranges from 20 to 40 CPs, where in each case, a different best-fit is executed, resulting to slightly different duct geometries.

The results of this study are presented in Figure 5.12. As the focus of this study is on the optimization gains of each parameterization, only the normalized values of the objective function are presented. The x-axis refers to the CPs number used to parameterize each airfoil while the left y-axis refers to the optimization results of each case and the right y-axis to the corresponding PE value of each case(initial PE value). Figure 5.12 indicates that as the parameterization becomes richer and the PE value increases, the optimization results become better. As a result, it confirms that parameterizations with higher PE values provide a better optimization results. It must be noted that the aforementioned is mainly due to the minor differences of the S-bend duct geometry.

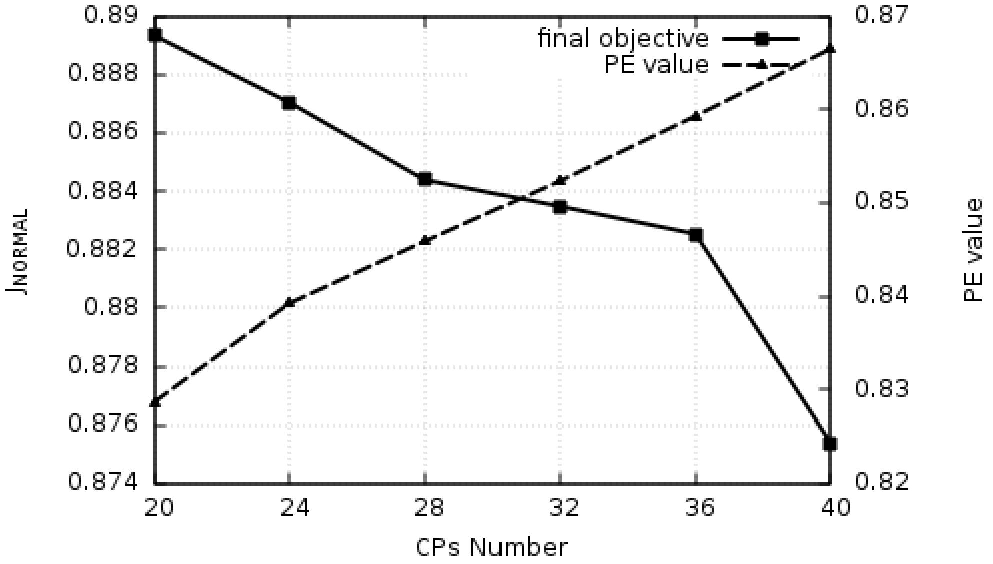

Figure 5.12: *S-bend duct optimization: Parametric study of the optimization solution and PE value w.r.t. the number of CPs.*

5.2.2 Comparison of Bezier curves and volumetric B-splines optimization potential

Four optimization cases are conducted utilizing Bezier curves for Cases 1 and 2 and volumetric B-splines for Cases 3 and 4. Cases 1 and 2 are parameterized by a different best-fit, based on the reference duct, using 20 and 40 CPs respectively. The total number of design variables in each case (1&2) equals to $N_b = 2N_{CP} - 16$. Moreover, Cases 3 and 4 are parameterized using volumetric B-splines using 135 and 90 CPs respectively with a basis degree equal to 3 for both x and y direction. The total number of design variables in Cases 3 and 4 equals to 25 and 10, respectively. It must be noted that both geometries are identical; however, in each shape, the parametric coordinates of its nodes are different.

The results of each case are presented in Table 5.4 and Figure 5.13. Although the geometries of Cases 1 and 2 are different between them and with that of Cases 3 and 4, their differences are not significant. Therefore, the normalized values of objective functions will be used to represent the objective function's value in each optimization cycle.

Firstly, as it can be observed, the solution of Case 2 is better compared to that of Case 1. Also Case 3 solution is better than Case 4. The final results of each study indicate that, despite the fact that different methods of parameterization are used in this study, as the initial PE value becomes higher, the objective function is further reduced. Therefore, the initial PE value in this application provides an indication of the optimization potential of each case.

Case ID	N_{CP}	N_b	$J_{initial}$	J_{final}	J_{final}^{normal}	PE
Case 1	20	24	7.1768E-07	6.382E-07	0.88704	0.8287
Case 2	40	64	7.1768E-07	6.270E-07	0.87372	0.8665
Case 3	45	25	7.1768E-07	6.355E-07	0.88553	0.8545
Case 4	30	10	7.1768E-07	6.377E-07	0.88853	0.7889

Table 5.4: *S-bend duct optimization: Comparison of the optimization results of Bezier and volumetric B-splines parameterizations w.r.t. their initial PE value.*

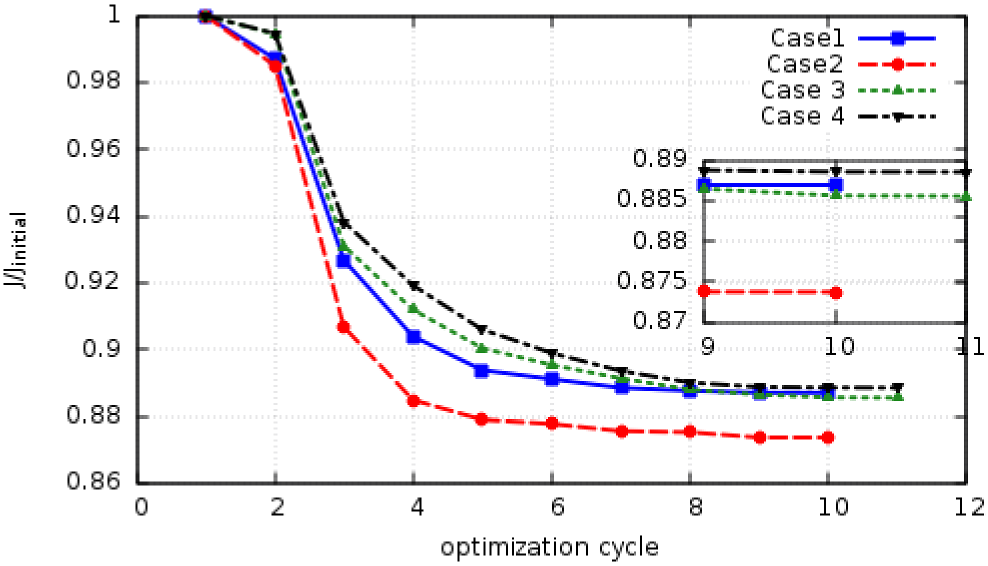

Figure 5.13: *S-bend duct optimization: Comparison of the objective function's values during the optimization procedure for Bezier and volumetric B-splines parameterizations.*

In order to study the PE of each case during the optimization, the PE values are computed for certain cycles of each case's optimization loop. In Cases 1 & 2, PE is computed after the execution of cycles: 1,2,3,6 and 10, and in Cases 3 & 4 after cycles: 1,3,6 and 10. The evolution of PE during the optimization for all cases is presented and compared in Figure 5.14. In Cases 1 & 2, PE is further increased by the end of the 2^{nd} cycle. Furthermore, as optimization goes on, it is reduced constantly reaching a final value lower than 0.05 in both cases. On the contrary, in Cases 3 & 4, the PE value is reduced constantly in the first six cycles. However, after the 10^{th} optimization cycle, the PE values of Cases 3 and 4 are both increased, obtaining the values of 0.697 and 0.870 respectively. Worth mentioning is that, the final PE value of Case 4 (after the 10^{th} cycle), is greater compared to its initial value and also grater than the corresponding of Case 3. The latter does not mean that the objective function of Case 4 should be lower compared to Case 3, it does only indicate that the optimization potential of the Case 4 parmeterization is closer to that of the nodal (which may be very low at that step of the optimization), for duct's geometry as formed by the optimization loop in the 10^{th} cycle.

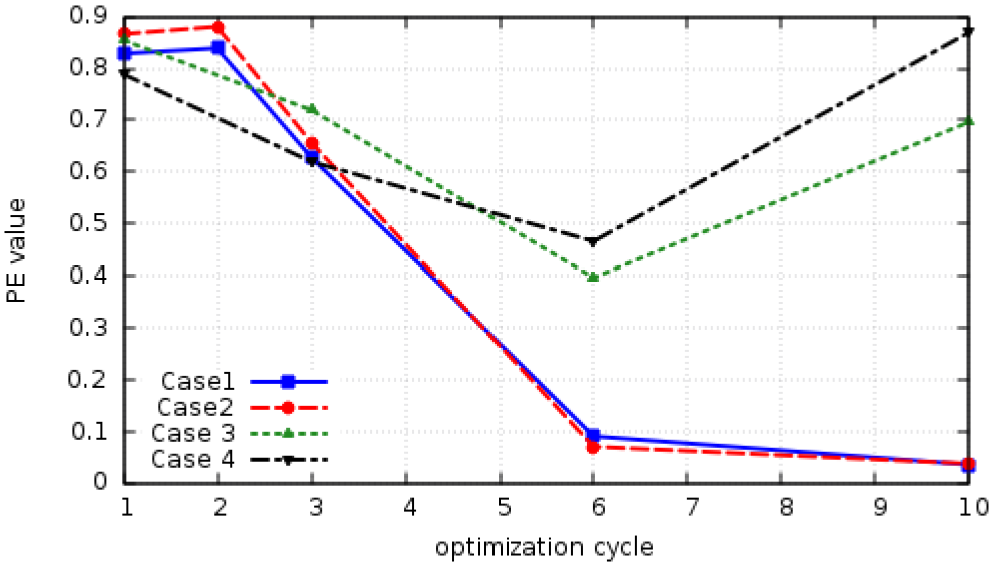

Figure 5.14: *S-bend duct optimization: Evolution of the PE values during the optimization.*

For demonstration purposes, only the velocity field of Case 2 optimized shape is presented and compared to this of it's initial shape in figure 5.15. The fields which refer to the initial shape are presented at the top, whereas the fields of the final shape at the bottom plot of each figure. Firstly, in Figure 5.15, the cross-section of the duct's curved section is increased, creating some valleys at various locations. These valleys induce vortices that do not interrupt the flow in the middle section of the duct, in fact they assist the flow to maintain its velocity, unlike the initial shape of the duct, in which the flow is forced to accelerate at the end of the curved section (due to a vortex existence as observed in Figure 5.15). The increase in flow velocity increases the total pressure losses as well. Therefore, the final geometry maintains a lower mean value of the velocity which leads to lower total pressure losses. Finally, although the vortices, in general, induce energy losses, in that case are located into the valleys without affecting the mean flow heading towards the outlet, resulting to generally lower total pressure losses.

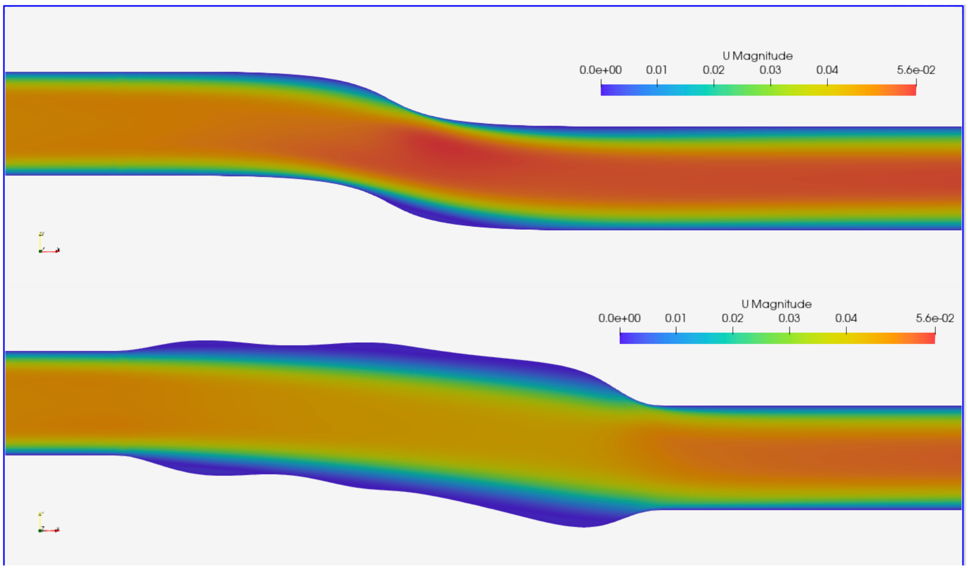

Figure 5.15: *S-bend duct optimization: Case 2 velocity field of the initial and optimized shape.*

5.2.3 Optimization using only the x and y coordinates

From the IPE values of Case 1 design variables (see Figure 4.14 and Figure 4.15 blue/continuous curve), it was found that the IPE values of the y coordinates are significantly larger than those of the x coordinates. Two optimization cases are performed (Case 5 and Case 6) using only the x coordinates and the y coordinates of the CPs which are allowed to be displaced. The results of each case are presented in Table 5.5 and Figure 5.16. As the duct shapes in both cases are identical, only the normalized final values of objective function are presented. It is observed that the result of Case 6 is very close to that of Case 1 with a relative difference of about 0.2%. On the contrary, the result of Case 5 is far from the previous two results with a relative difference w.r.t. Case 1 equal to 7.9%. Also the difference in the objective function for Case 5 compared to it's initial value is relatively small as well. From the above, it is concluded that, the utilization of only the CP's y coordinates as design variables may provide similar results to that of using both the x and y coordinates.

The optimized shapes of the S-bend's curved section are presented in figures Figure 5.16 and Figure 5.17 for Cases 5 and 6 respectively. The continuous lines represent the optimized geometry in each case, whereas the dashed lines represent the initial shape of the S-bend curved section. As can be observed, the shape of Case 5 is not modified significantly compared to that of Case 6 due to the lower IPE values of x coordinated.

The flow fields are present for both cases 5 and 6 in Figure 5.18. Each

Case ID	N_{CP}	N_b	J_{norm}	PE
Case 1	40	64	0.87607	0.8665
Case 5	40	32	0.94537	0.8356
Case 6	40	32	0.88720	0.6974

Table 5.5: *S-bend duct optimization: Optimization of the duct using the parameterization of Case 1, considering the x and the y coordinates as design variables in Cases 5 & 6.*

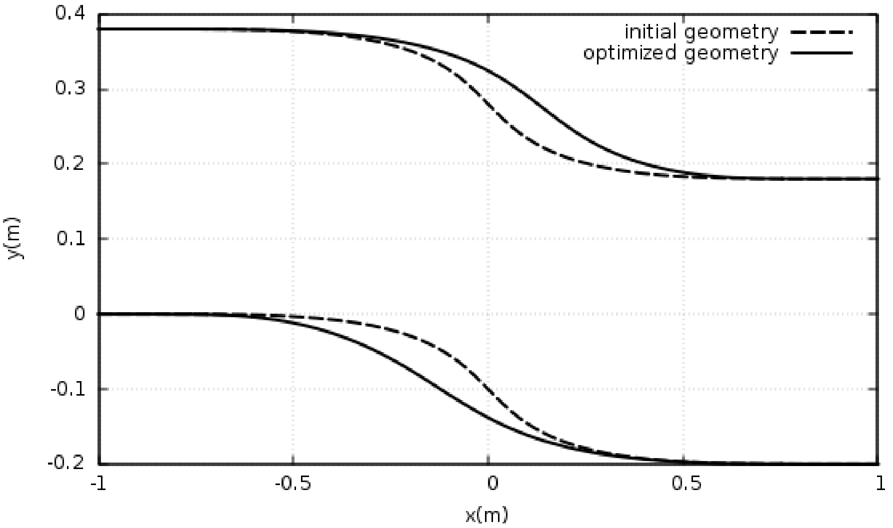

Figure 5.16: *S-bend duct optimization: Comparison of the optimized and initial geometry of Case 5.*

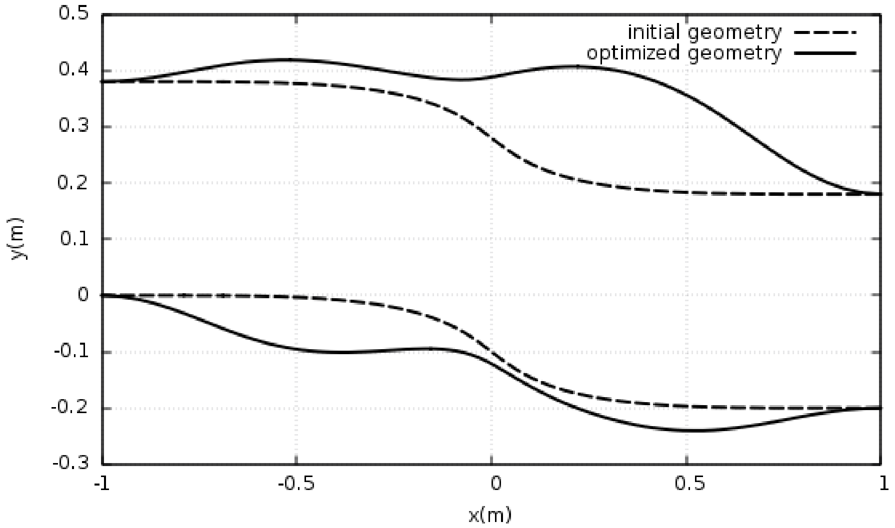

Figure 5.17: *S-bend duct optimization: Comparison of the optimized and initial geometry of Case 6.*

figure contains the initial geometries field at the top and the final-optimized geometries field an the bottom. For each figure, the left plots refer to Case 5 and the right plots to Case 6. The results of both figures indicate that, both optimizations opt to eliminate the low pressure areas at the curved section of each duct. However, Case 6 is able to create the convex bumps, which induce the effects described above in Case 2 resulted flow fields. The latter validates the indications of IPE values and the importance of the y coordinates compared to the x coordinates in the optimization loop.

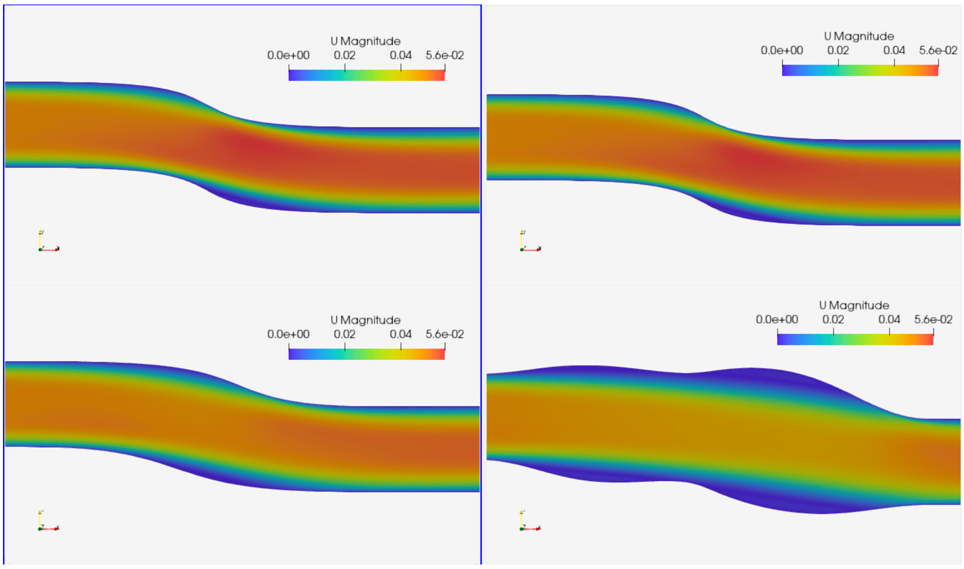

Figure 5.18: *S-bend duct optimization: Cases 5 and 6 velocity (magnitude) fields.*

5.3 Optimization of the 2D compressor cascade

In this section, the airfoil of the 2D compressor cascade as presented in section 4.3 is optimized using NURBS curves parameterization. In this section, two optimization cases are presented and compared. Case 1 is parameterized using 61 CPs whereas Case 2 using 69 CPs in total, in order to reconfirm the increase in PE value as CPs number increases, and its impact in the optimization of the compressor airfoil. One may observe that the difference in CPs number is relatively small. However due to the large deformation of the airfoil during the optimization loop which causes the overlapping of the CPs near the leading and trailing edges, various CPs affecting these regions must be fixed. The two parameterizations are selected so that the same CPs are fixed in each case, leading to a more fair comparison.

The constraints applied in this application is the conservation of the airfoil's total surface area and keeping fixed the first and last four CPs of each side in order to maintain the desired shape continuity between the pressure and the suction side. Moreover in order to maintain the turning of the airflow between the leading and the trailing edge of the compressor airfoil (thus the static pressure increase), more CPs are kept fixed in those regions. Specifically, the first ten and last eight CPs of the pressure side alongside the first four and last nine CPs of the suction side are kept fixed during the optimization. Considering that the fixed CPs have the greatest IPE values, the resulted PE value of each case is expected to be significantly reduced compared to those presented in section 4.3.

The results of both cases are presented in Table 5.6 and Figure 5.19. Firstly, it can be seen that due to the constraints applied, the initial PE values of both cases are significantly reduced. Furthermore,it is observed that, the total pressure losses in Case 2 are lower compared to Case 1 by almost $0.09m^2/s^2$, which is only about 1%. Moreover, the reduction in the objective function in Case 2 is greater compared to that of Case 1 (as Case 2 initial J value is higher). The above results, indicate that the optimization of Case 2 is more effective compared to that of Case 1.

Case No	N_{CP}	N_b	J_{init}	J_{final}	J_{normal}	PE
Case 1	61	60	9.77798	9.59732	0.98152	0.05826
Case 2	69	76	9.78580	9.50924	0.97174	0.12675

Table 5.6: *Compressor cascade optimization: Results of Cases 1 & 2.*

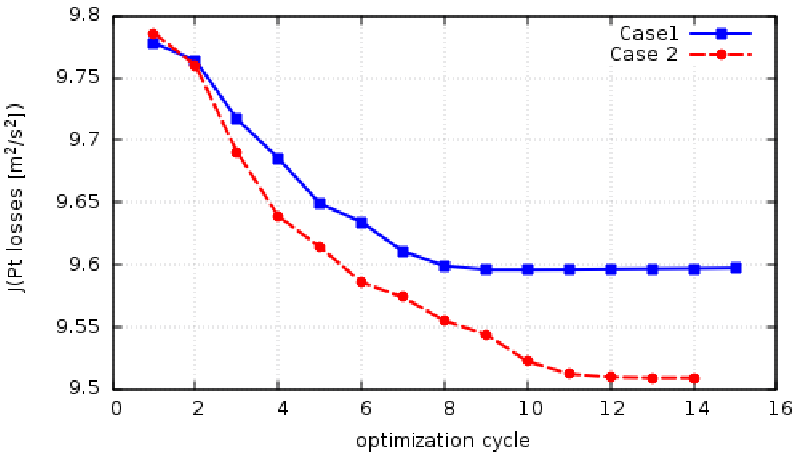

Figure 5.19: *Compressor cascade optimization: Objective function's values during the optimization procedure of the blade airfoil.*

The evolution of PE values during the optimization in both cases is presented in Figure 5.20. PE values are computed for the 1^{st}, 3^{rd}, 6^{th} and 10^{th} optimization cycles. It is observed that the PE value of Case 2 remains higher during the entire optimization. Moreover, in both cases the PE value is reduced until the 6^{th} cycle, where the PE of Case 1 continues to decrease whereas, the PE value of Case 2 has a minor improvement by the end of the 10^{th} cycle.

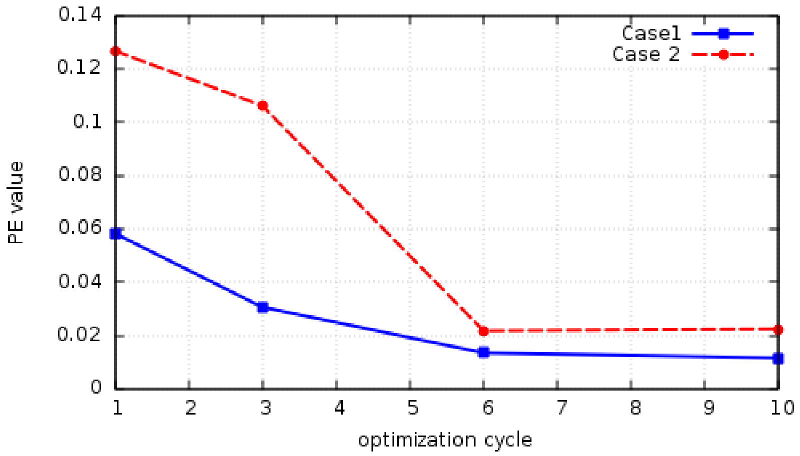

Figure 5.20: *Compressor cascade Optimization: Evolution of PE during the optimization loop.*

A comparison of the initial and optimized geometry of each case's compressor airfoil is presented in figure Figure 5.21. The blue/continues line refers to the optimized geometries whereas the red/dashed line to the initial shape of each case's airfoil. As it can be seen, the differences of the initial and optimized shapes in both cases are minor.

The flow fields of each case's initial(top) and final(bottom) geometry are presented in Figure 5.22. In each figure, the plots on the left refer to Case 1, whereas the plots on the right to Case 2.

The only observable difference between each cases initial and final fields is the reduction of the area around the leading edge's where velocity is zero, which may contribute to the reduction in total pressure losses for each case. Furthermore, from Figure 5.22, the aforementioned area (of high pressure) around the leading edge, it is observed that, it expands on the pressure side of each of the optimized airfoils. The latter may also contribute to the reduction of total pressure losses. To conclude, the geometrical differences between the optimized airfoils of Cases 1 and 2 are very small, which reflects also on their flow fields differences as well.

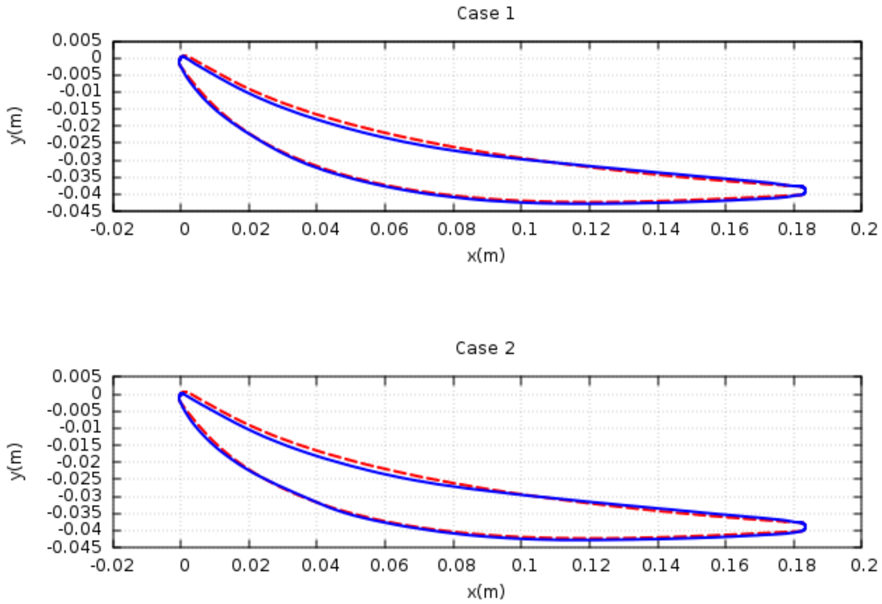

Figure 5.21: *Compressor cascade Optimization: Comparison of the optimized and the initial shape of each blade airfoil.*

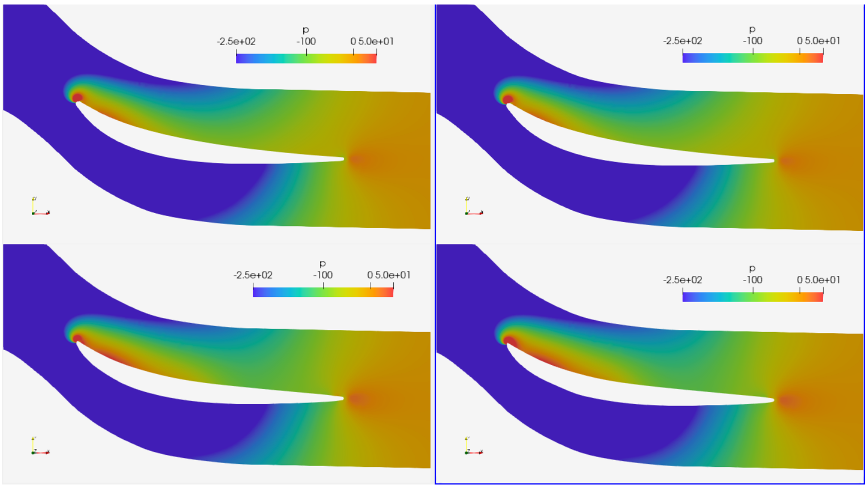

Figure 5.22: *Compressor cascade Optimization: Pressure fields of Cases 1(left) and 2(right).*

Chapter 6

Summary-Conclusions

6.1 Summary

The purpose of this diploma thesis was the formulation, implementation and study of the PE as a metric to rate the optimization potential of a CAD parameterization. Also, to investigate ways of implementing PE (in various forms) in shape optimization, based in gradient-based methods, in CFD.

In this diploma thesis, the geometries were parameterized using, NURBS curves, Bezier-Bernstein and volumetric B-splines parameterizations. NURBS and Bezier-Bernstein curves parameterize only the contours of the geometry to be optimized using a best-fit, that produces slightly different geometries compared to the original. On the contrary, volumetric B-splines parameterize, the contours and the internal grid as well(enclosed within the morphing box boundaries), producing the exact same shape as the original. These parameterizations are all formulated by analytic mathematical expressions that produce smooth shapes by definition. Thus, no smoothing algorithm is required.

Initially, the PE was defined as the ratio of the CAD parameterization's performance gains w.r.t. that of the NODAL's (this abbreviation stands for the case the optimization controls all surface nodes one-by-one). The performance gains expressions, are derived from the steepest descent definition. For a fair comparison between the CAD and NODAL parameterization in each case, an appropriate condition for the ratio of steepest descent steps (η_{CAD}, η_{NODAL}) is introduced.

For the PE study, three applications were introduced, an isolated airfoil, an S-bend type duct and a 2D compressor cascade (optimization of a single blade airfoil using periodic BC). The objective in the isolated airfoil case was drag, whereas for the other problems total pressure losses. The isolated airfoil and the compressor blade airfoil were parameterized using NURBS curves, whereas the S-bend duct using both Bezier-Bernstein curves and volumetric B-splines.

The investigation of the PE behaviour was conducted through the studies of chapter 4, where the PE value is computed for different number of CPs and different parameterization methods.

The PE results were assessed by the optimization results through various optimization loops for each application. During these loops, the PE was computed for certain cycles in order to investigate its evolution during the optimization. The optimization cases of the isolated airfoil were all constrained to retain the C_L and the volume within in predefined bounds compared to the initial one, and the produced airfoil to be trimmed($C_m \approx 0$). The optimization runs include cases using different parameterizations and cases utilizing only certain parameters as design variables. In addition, a parametric study was conducted using different numbers of Bezier CPs to compute the PE values and optimize the S-bend duct, aiming to identify the relationship of the PE with the optimization results. Moreover, in order to compare the two parameterization methods used in the S-bend duct, four optimization runs were carried out, each associated with different PE values. Also, two optimization runs were performed using only the x and y coordinates of a certain parameterization. The optimization of the blade's airfoil was done by utilizing two cases, parameterized with different number of CPs, falling under the same constraints. The most important constraint was to maintain the turning angle of the velocity from the leading to the trailing edge, in order to maintain pressure rise. Also the volume of the blade's airfoil was maintained the same during the entire optimization loop of each case.

6.2 Results-Conclusions

Firstly, all parametric studies regarding the dependence of the PE value on the number of CPs indicated that, as the CAD parameterization becomes richer, the PE value is monotonically increasing, converging asymptotically to a maximum value. Moreover, it is proved that, as the PE value increases, optimization results are better.

The comparison of Bezier and volumetric B-splines parameterization of the S-bend duct, proved that parameterizations with higher PE values provide better optimization results, irrespective of the utilized parameterization.

Furthermore, the PE values during the optimization for NURBS and Bezier parameterizations are reduced as optimization goes on. On the contrary, for the volumetric B-splines parameterizations, the PE values do not have a monotonic behaviour.

Moreover, it can be concluded that the IPEs of the design variables can be used to select the most effective design variables in an optimization run which may produce a solution close to that obtained by using all the design variables. However, by selecting a predefined number of parameters based only on their IPE values, the resulted solution may differ significantly from that of the initial parameterization. Thus, prior to the design variables selection, the impact of a single design variable must be investigated by using the percentage of its IPE value w.r.t. the IPE values sum.

To conclude, the PE can be used to assist designers to select appropriate parameterizations prior to an optimization cycle. Also, it may be used to compare the optimization potential between different parameterizatios. Low values of PE indicate that enrichment or even a re-parameterization may be needed in order to achieve a decent optimization potential. However, in certain cases where strict constraints are applied, and a significant amount of CPs are fixed, the PE values may obtain very small values, even when large amount of CPs are used.

6.3 Future Work

- So far, in the presented parametric studies, the PE was controlled manually (by stopping the optimization loop, checking the value of the PE, making some decision on how to continue etc). Findings of the work should lead to some automatic actions within the optimization loop. So, future work can be focused on when (within the optimization loop) PE should be recomputed, how this piece of information can be used to improve the loop, etc.
- It will be extremely interesting the notion of the PE and the way this affects the reduction in the number of design variables to be used in a population-based stochastic optimization method, such as the EA. The optimization cost when using the EA is proportional to the number of design variables and their combinations. As a result, the reduction in potential combinations may reduce the number of (CFD) evaluations needed until reaching the optimized solution.

Appendix A

Geometry and parameterization generation

In this diploma-thesis, the geometries are parameterzed using NURBS curves and volumetric B-splines on the pregenerated 2D grids of each application. Prior to any elaboration in the parameterization procedure, a short reference regarding the 2D grids used in this diploma thesis is considered to be useful.

A.1 NURBS curves parameterization

NURBS curves are defined as:

$$\vec{r_i} = \sum_{k=0}^{N} B_{k,p}\left(u_i\right) \vec{R_k} \tag{A.1}$$

$$B_{k,p}(u_i) = \frac{N_{k,p}(u_i) w_k}{\sum_{k=0}^{N} N_{k,p}(u_i) w_k} \tag{A.2}$$

Where:

$\vec{r_i}$ is the i^{th} node's x,y coordinates vector, $i = 1, \dots, N_s$,

$\vec{R_k}$ is the k^{th} CP's, x,y coordinates vector, $k = 0, \dots, N$,

$N_{k,p}$ are the p^{th} degree B-splines basis functions,

w_k is the k^{th} CP's weight,

u_i is the parametric coordinate of the i^{th} node, $u, \in [0, 1]$.

The parameterization is applied based on the selected patches, i.e. the pressure and suction side of the airfoils or the upper and lower side of the duct. Initially each curve is parameterized by the implementation of a best-fit algorithm, given the desired number of CPs, the basis functions degree, the weights of each CP, the Cartesian and parametric coordinates of each curve.

Prior to the CP coordinates approximation, the basis functions values are computed for each node based on its parametric coordinate. Then, by using the basis functions values and the Cartesian coordinates of each node, a mathematical system is formulated based on eq.(A.1), which is solved using the Newton-Raphson method to compute the CP's coordinates.

In general, the curves generated by the computed CP's coordinates, provide an approximation to the original geometry. Thus, a grid displacement procedure is performed to displace the internal grid nodes and make them match those produced by the NURBS curves. As a result, the simulated geometry is modified compared to the original. However, for an adequate number of CPs, the parameterized geometry approaches the original geometry with a satisfactory accuracy.

A comparison between the parameterized and the original geometry of the isolated airfoil can be made through Figure A.1 and Figure A.2. In both figures, only the suction side of the airfoil is displayed in a scale that makes differences between the parameterized and the original airfoil visible. The blue/continuous lines refer to the parameterized (fitted) curves, whereas the red/dashed lines to the original curve. The curve of Figure A.1 is parameterized using 6 CPs whereas that of Figure A.2 using 8 CPs. In Figure A.1 the differences between the two curves are clear. On the contrary, this does not happen in Figure A.2, where the parameterized geometry reproduces the original with a decent accuracy.

The distribution of CPs for both parameterizations(6 CPs and 8 CPs) is demonstrated in Figure A.3, with the blue/continuous lines representing the 6 CP and the red/dashed lines the 8 CP parameterization. One may observe that the x coordinates of the first and second CPs of the 6CPs parameterization are different, which implicates that, in the airfoil application the leading edge of the parameterized airfoil will not have a C1 continuity.

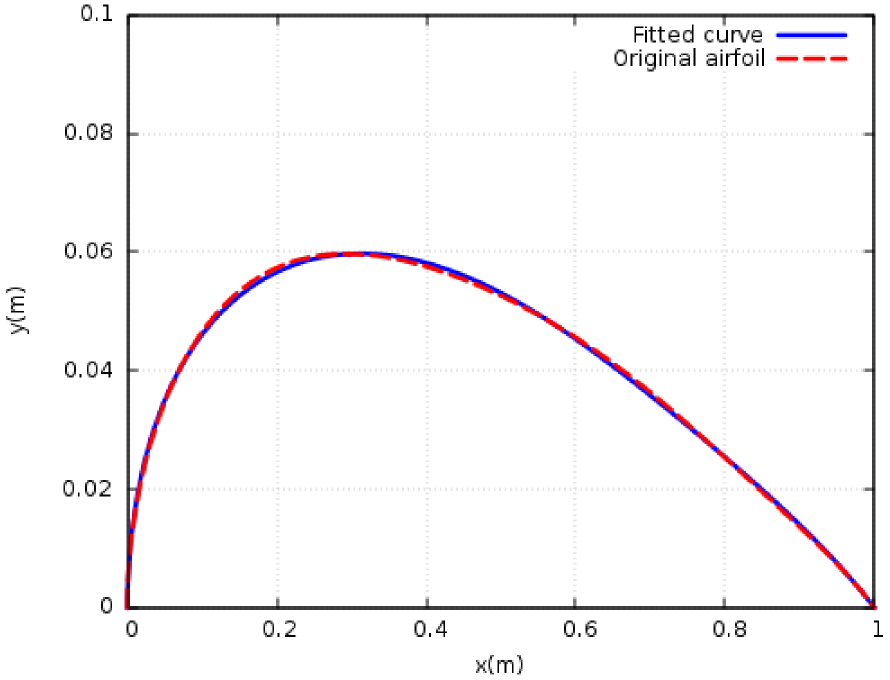

Figure A.1: *Comparison of the NURBS curve (produced by the best-fit) using 6CPs with the original curve.*

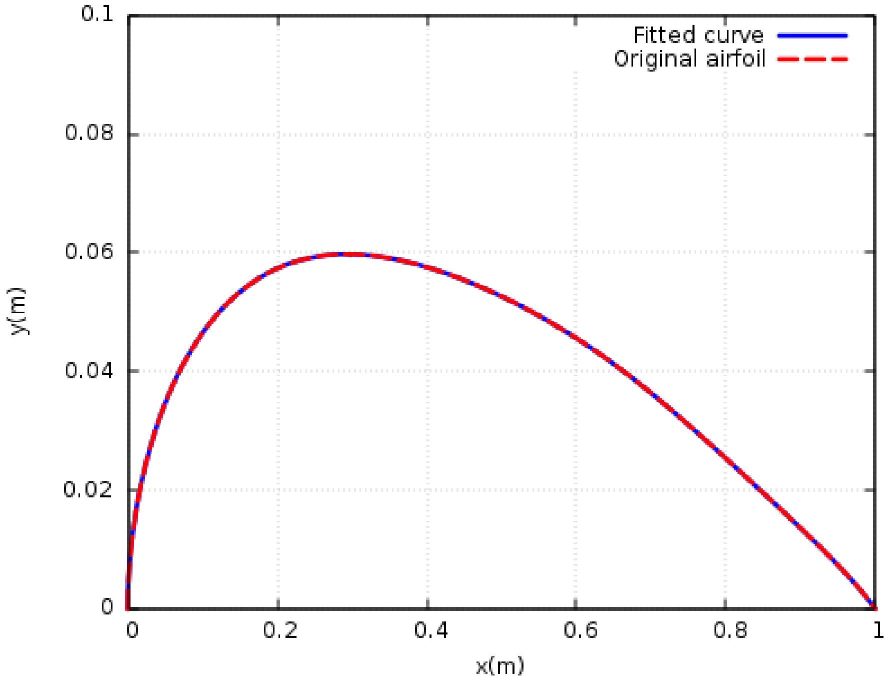

Figure A.2: *Comparison of the NURBS curve (produced by the best-fit) using 8CPs with the original curve.*

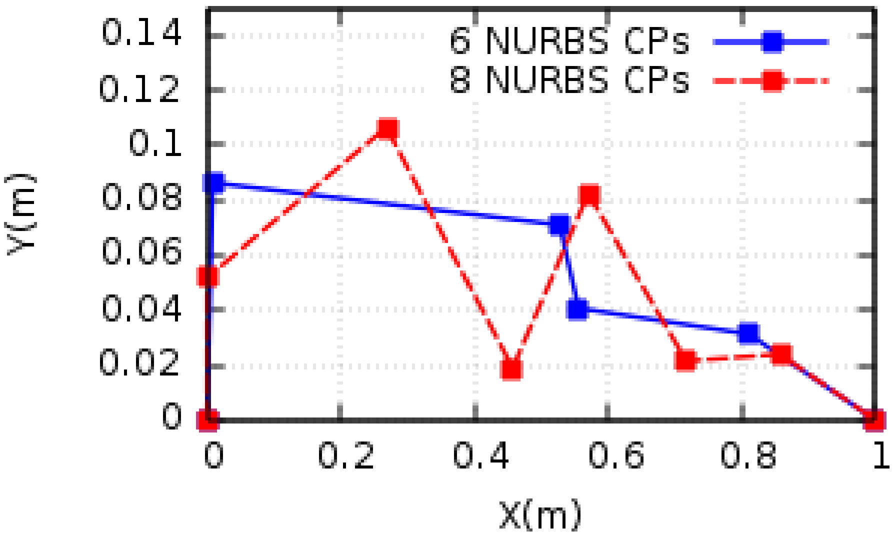

Figure A.3: *CPs distribution of the two NURBS parameterizations using 6CPs and 8CPs.*

A.2 Bezier parameterization

The Bezier curves form a specific expression of the NURBS when all the CPs weights equal to 1 and the basis functions degree equal to N, where $N+1$ is the total number of CPs. For completeness purposes the mathematical derivation of Bezier is presented in this section. Bezier curves are given by the following formulas([14]) in vectorial form:

$$\overrightarrow{r(u_i)} = \sum_{i=0}^{N} \hat{\vec{r}}_k B_k^N(u_i) \tag{A.3}$$

$$B_k^N(u_i) = \binom{N}{k} u_i^k (1-u_i)^{N-k} \tag{A.4}$$

$$\binom{N}{k} = \frac{N!}{k!(N-k)!} \tag{A.5}$$

where:

$\hat{\vec{r}}_k$ is the vector containing the x, y, coordinates of the k^{th} CP, $k = 0, \ldots, N$,

u_i is the i^{th} node's parametric coordinate,

$r(\vec{u_i})$ is the vector containing the x, y coordinates of the i^{th} node.

An example of the Bezier parameterization is presented in Figure A.4, where the upper side of the S-bend duct's curved section is parameterized using 14 CPs.

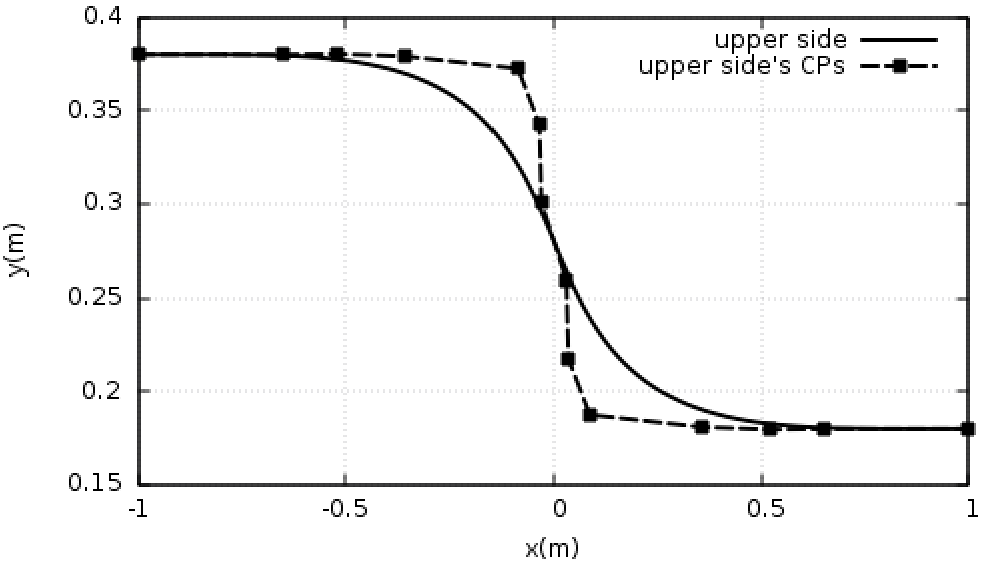

Figure A.4: *Bezier parameterization of the S-bend ducts upper side.*

A.2.1 Enrichment of Bezier curves

When the enrichment algorithm is implemented, the number of CPs used to parameterize each curve is increased by one, producing the exact same geometry(identical surface nodes). If more CP insertions are desired, the enrichment algorithm must be implemented sequentially until reaching the desired number of CPs. Obviously, the degree of basis function's polynomial is also increased by one.

The enrichment is implemented using the equations given by [1], can be written as follows:

$$\vec{R_0} = \vec{r_0} \tag{A.6}$$

$$\vec{R_n} = \frac{n}{N+1}\vec{r_{n-1}} + (1 - \frac{n}{N+1})\vec{r_n}, \quad \text{for} \qquad 1 \leq n \leq N, \tag{A.7}$$

$$\vec{R_{N+1}} = \vec{r_N} \tag{A.8}$$

where:

n is a counter that takes values: $n = 0, \ldots, N+1$

$N+1$ is the total CPs number if the intial parameterization,

$\vec{R_n}$ is the coordinates vector of the enriched parameterization's n^{th} CP,

$\vec{r_n}$ is the coordinates vector of the initial parameterization's n^{th} CP.

Two examples of the parameterization enrichment are presented in figures A.5 and A.6. In the first example (S-bend duct's upper side), the initial parameterization consist of 7CPs. When the enrichment algorithm is implemented, the same curve is reproduced using 8CPs. In the second example (airfoil's suction side), the initial parameterization consists of 9 CPs. After the execution of the enrichment algorithm the exact same geometry is parameterized using 10CPs.

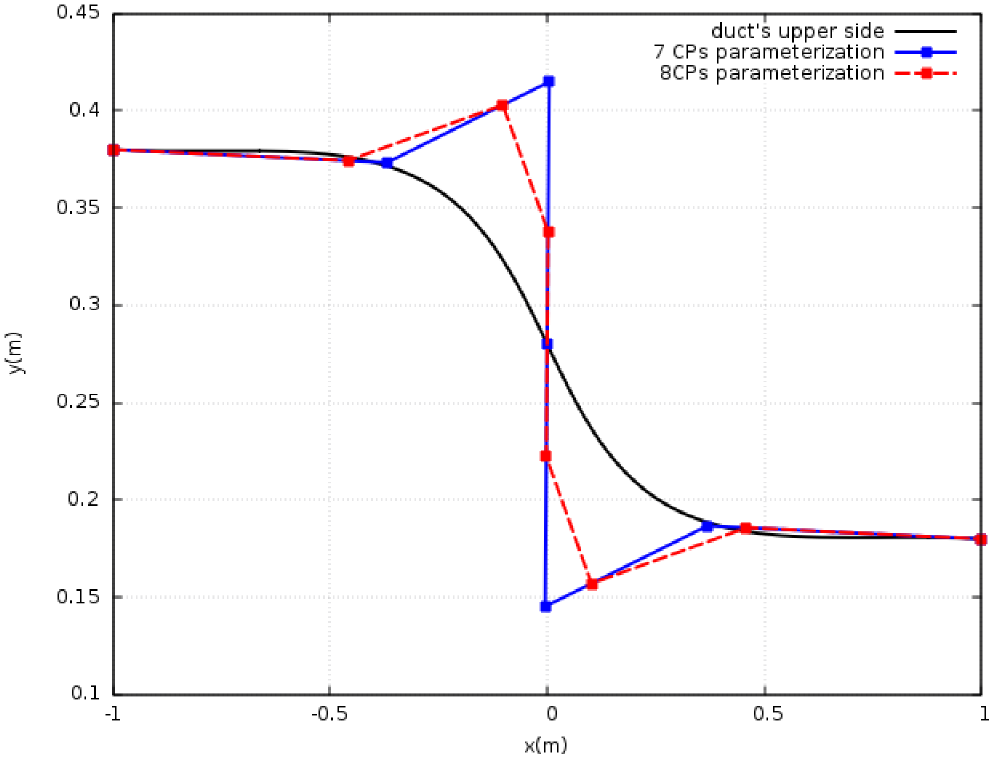

Figure A.5: *Enrichment of the parameterization for the S-bend's upper side.*

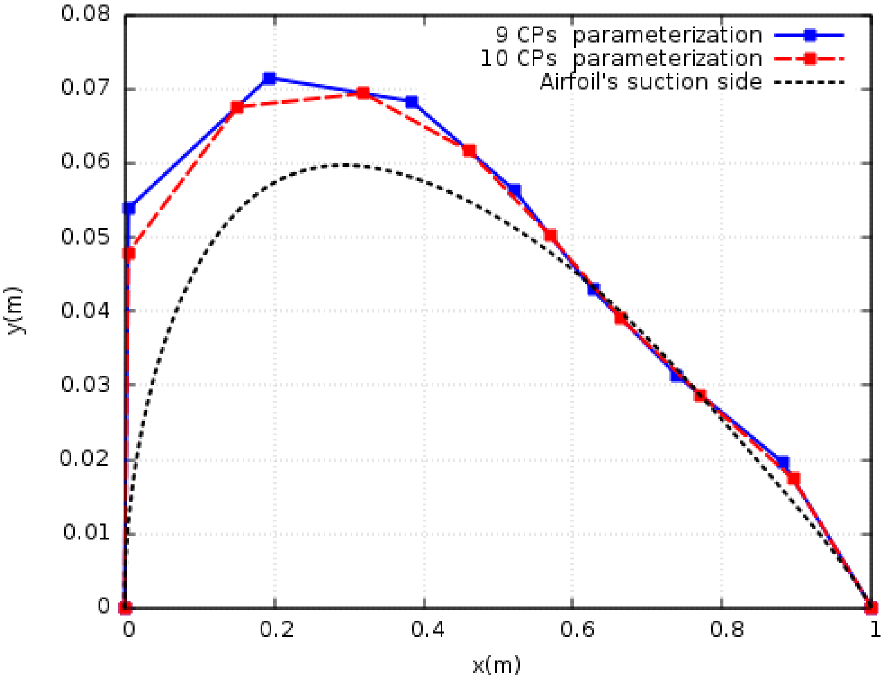

Figure A.6: *Enrichment of the parameterization for the airfoil's suction side.*

A.3 Volumetric B-splines parameterization

In this diploma thesis, volumetric B-splines parameterization method is used only in the S-bend duct's application. A morphing box is introduced which is composed by the CPs grid, enclosing the boundaries of the geometry to be optimized. The morphing box's CPs are distributed in x,y directions using $I+1, J+1$ CPs respectively, equally spaced in each direction. The mathematical derivation of the Volumetric B-splines as given by [15] is derived as follows:

$$\vec{x}_m\left(u,v,w\right)=\sum_{i=0}^{I}\sum_{j=0}^{J}U_{i,pu}(u)V_{j,pv}(v)P^{ij} \tag{A.9}$$

where:

$\vec{x}_m(u,v)$ is the Cartesian coordinates vector of the m^{th} node,

$\vec{P}^{ij}$ is the ij^{th} CP's Cartesian coordinates vector,

u, v, are the parametric coordinates of the grid nodes,

U, V are the B-splines basis functions (for x, y directions),

pu, pv are the basis functions degree for U, V basis functions respectively.

Unlike the NURBS parameterization, the volumetric b-splines parameterize all the internal grid's nodes located within the boundaries of the morphing box where a direct relation exist between the (x, y) and (u, v) coordinates of each node. Therefore, given the CPs and contour nodal coordinates and the basis functions degrees, the parametric coordinates can be computed with machine accuracy. Then, a non-linear system of two equations is formulated for each node and solved with Newton-Raphson, which involves the actual m^{th} node's coordinates with those given by Equation A.9 as:

$$\vec{R}_m = \vec{x}_m(u, v) - \vec{x}_{m,r} \tag{A.10}$$

Where:

$\vec{R}_m$ is the residual of the equations (x, y) for each node,

$\vec{x}_m(u, v)$ is the volumetric b-splines equation of the m^{th} node,

$\vec{x}_{m,r}$ is the (x_r, y_r) coordinates vector of the m^{th} node.

Appendix B

CFD results of the three applications

In this appendix, basic information regarding the CFD setup and results of each application are presented. The primal problem in all applications of this diploma thesis is considered to be incompressible and described from RANS (Reynolds Averaged Navier Stokes) equations. For both primal and adjoint fields computation as well as sensitivity derivatives extraction, the OpenFOAM software is used.

B.1 Isolated airfoil CFD setup and results

Case's grid is a C-type structured grid and composed of 189 × 208 nodes (39312 total nodes and 37800 cells). Figure B.1, provides an image of the grid at the airfoil's near region where grid's structure and layering can be observed in more detail. Moving outwards from the airfoil, cells height is expanded constantly towards domain's boundaries.

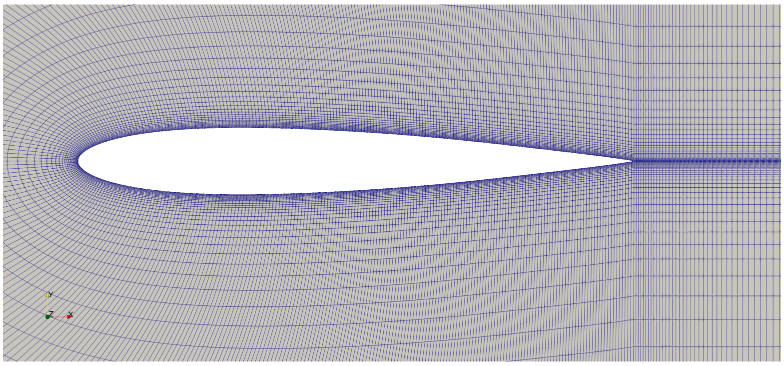

Figure B.1: *Airfoil's C-Type structured grid for primal and adjoint fields computation and PE evaluation.*

The origin is the airfoil's front-most point. The total length of the chord-wise direction is 30 airfoil chords which also applies in the vertical direction.

Below some basic information regarding the flow conditions are presented:

- Laminar flow
- Reynolds number: $R_e = 1000$.
- Far field flow angle of 2 deg

Boundary conditions are constant velocity inlet and constant pressure outlet. The airfoil is simulated as a no-slip wall. Neumann condition on the pressure is applied normal to all the domain's boundary patches and the airfoil except from the outlet.

The velocity flow field is given in Figure B.2, and kinematic pressure field is given in Figure B.3. The adjoint velocity field is given in Figure B.4 whereas the adjoint pressure field in Figure B.5.

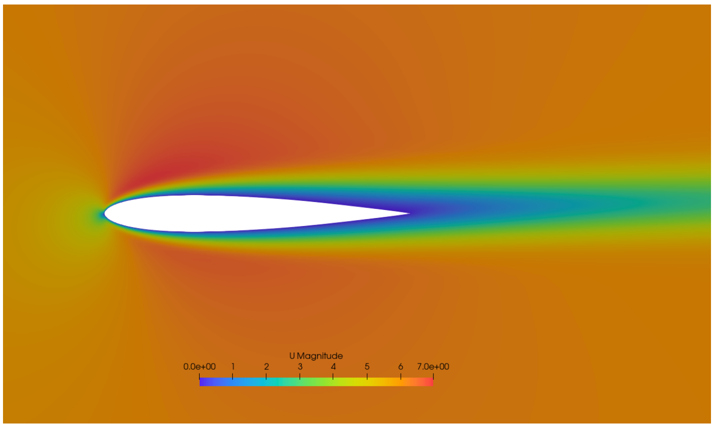

Figure B.2: *Isolated airfoil: Velocity field of the reference airfoil.*

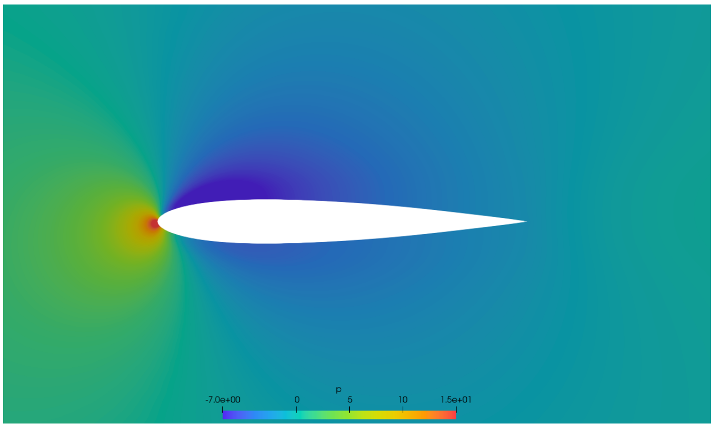

Figure B.3: *Isolated airfoil: Pressure field (of the reference problem) for the simulated airfoil.*

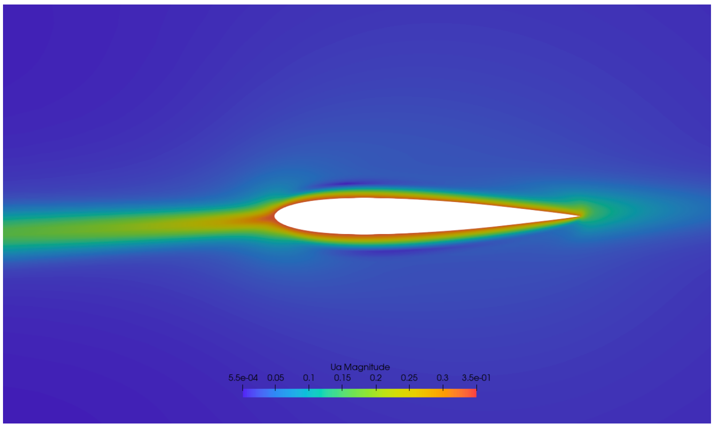

Figure B.4: *Isolated airfoil: Adjoint velocity field of the reference airfoil.*

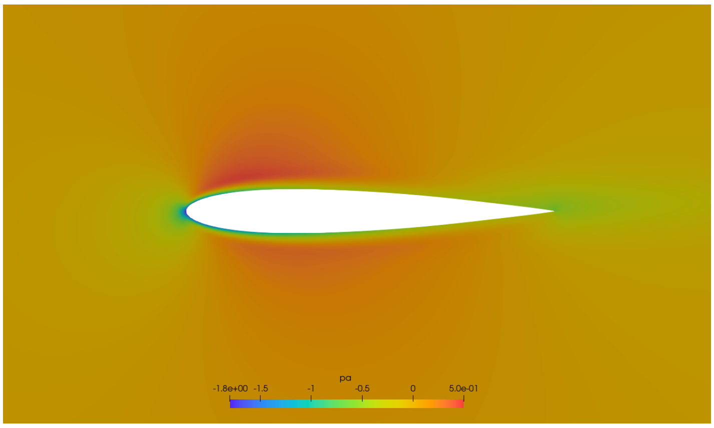

Figure B.5: *Isolated airfoil: Adjoint pressure field of the reference airfoil.*

B.2 S-bend type duct CFD setup and results

The application's geometry and grid are presented in Figure B.6 and a Figure B.7, respectively, where the first also presents the dimensions of the duct. The second figure is provided for better representation of the structured grid which consist of 201 × 121 nodes (24321 total nodes and 24000 cells).

The boundary conditions regarding the inlet and the outlet as well as the walls are the same with the corresponding of the isolated airfoil.

Basic information regarding the flow conditions:

- The flow is laminar
- Reynolds number: $R_e = 1000$

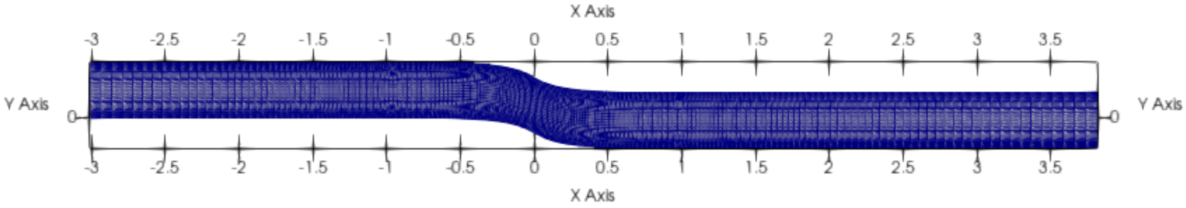

Figure B.6: *S-bend duct: Grid of the reference duct.*

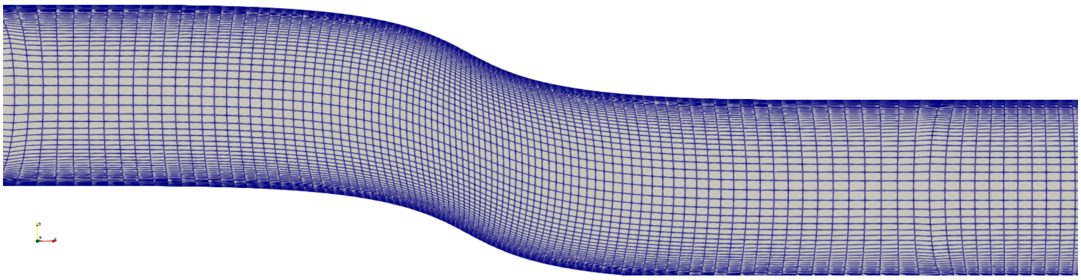

Figure B.7: *S-bend duct: Grid of the reference duct.*

The flow fields of the reference duct are presented in figures B.8 to B.11.

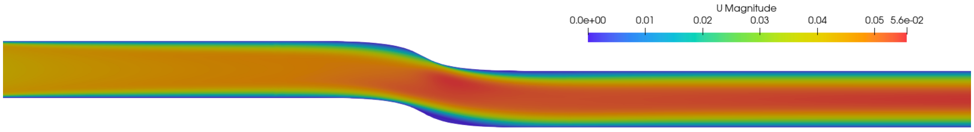

Figure B.8: *S-bend duct: Velocity field of the reference duct.*

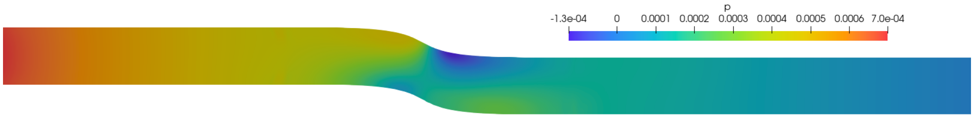

Figure B.9: *S-bend duct: Pressure (kinematic) field of the reference duct.*

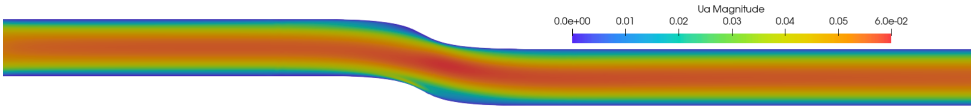

Figure B.10: *S-bend duct: Adjoint velocity field of the reference duct.*

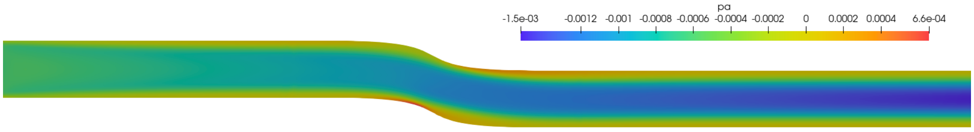

Figure B.11: *S-bend duct: Adjoint pressure field of the reference duct.*

B.3 2D Compressor cascade CFD setup and results

This application grid is presented in Figure B.12 and Figure B.13, which is composed by 63332 cells an 97132 nodes. As it can be seen, the grid is unstructured, however certain areas i.e. the airfoil's near region, and the wake area, have structured-like layers.

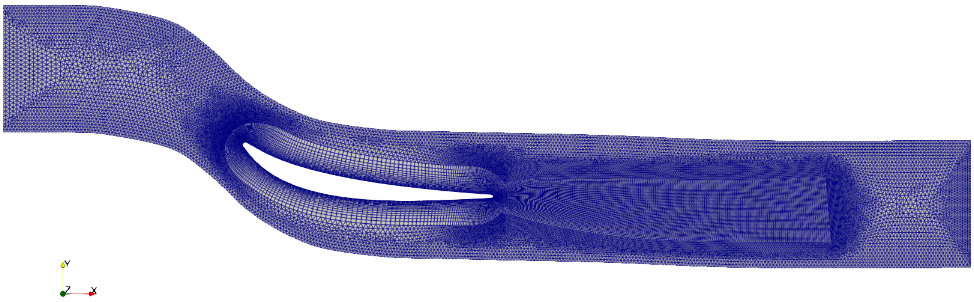

Figure B.12: *Compressors 2D cascade: Reference compressor's airfoil grid.*

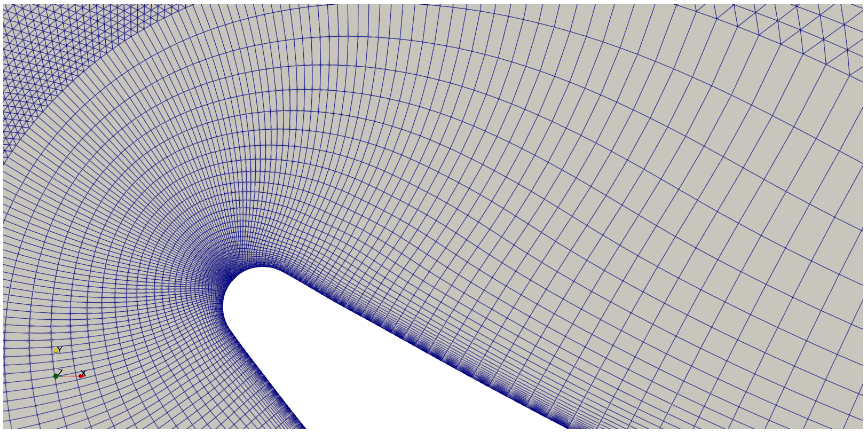

Figure B.13: *Compressors 2D cascade: Reference compressor's airfoil grid near the leading edge region.*

Information regarding the flow conditions:

- The flow is turbulent, modeled using the low-Reynolds Spallart-Almaras turbulence model
- Inlet velocity: $48m/s$ at an angle of $-42°$ to the horizontal axis of the domain
- Kinematic viscosity:$1.339 \times 10^{-5} m^2/s$

Finally, the primal and adjoint fields are presented in figures B.14 to B.17:

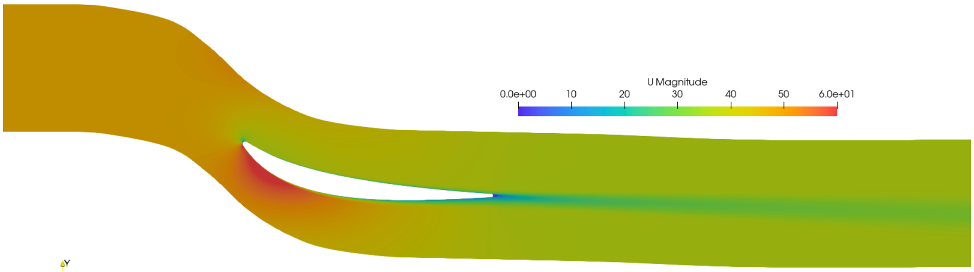

Figure B.14: *Compressor's 2D cascade: Velocity field of the reference compressor's airfoil.*

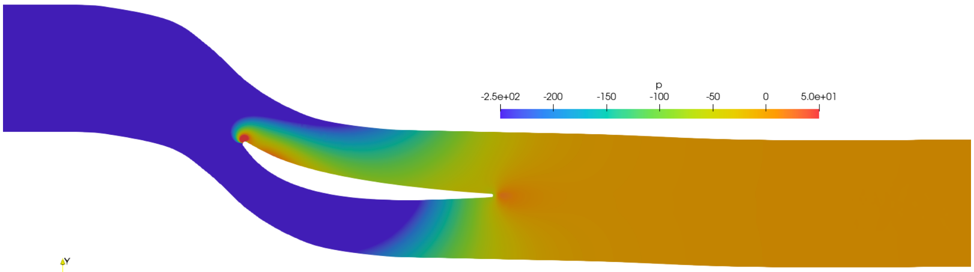

Figure B.15: *Compressor's 2D cascade: Kinematic pressure field of the reference compressor's airfoil.*

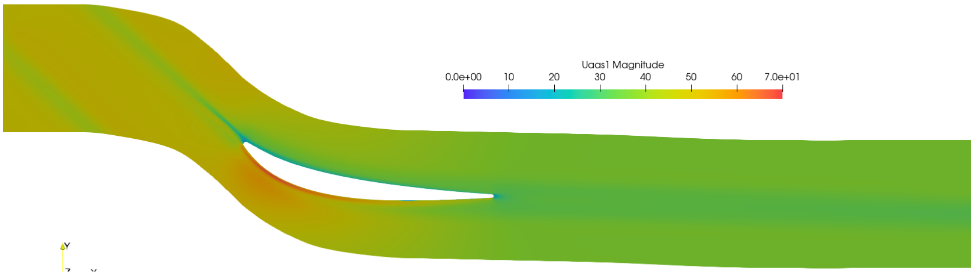

Figure B.16: *Compressor's 2D cascade: Adjoint velocity field of the reference compressor's airfoil.*

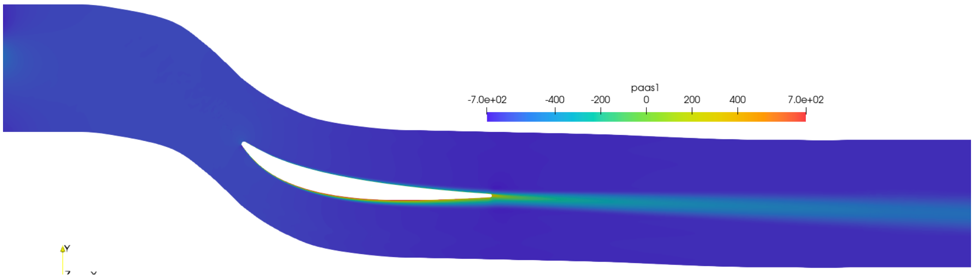

Figure B.17: *Compressor's 2D cascade: Adjoint pressure field of the reference compressor's airfoil.*

Appendix C

PE code test in a simple application

This appendix, refers to a 2D case built only to study the PE theory and its evaluation. It does not refer to an industrial or realistic application but its purpose is only to evaluate the software used in PE computation. The case simulates a duct with a bump in its middle section, which is the geometry to be optimized. PE is computed, using the same number of nodes and CPs. The flow is considered to be incompressible and laminar, where objective function of this application is the minimization of total pressure's losses between inlet and outlet of the duct.

The goal of this case is to compute the PE in a case where the geometry to be optimized is parameterized using equal number of CPs and surface nodes, in order to identify whether the PE value equals to 1 when the CAD parameterization is as rich as the nodal. The bump's geometry is parameterized using NURBS curves with all weights set equal to 1 and the basis functions degree equal to $N_{CP} - 1$, where N_{CP} is the number of CPs. The geometry is parameterized by performing the best fit algorithm of Appendix A, where in this case, since the number of CPs equals to the number of surface nodes, the best fit algorithm computes the exact CPs coordinates. As a result the parmeterized and the original geometry are the same. Also, since the CPs and surface nodes have the same number, the PE value should be equal to 1.

Case's grid

In order to minimize the computational cost, a coarse grid composed of 4018 cells was introduced, since the only interest is in the PE computation. The bump geometry is composed by 10 nodes, thus 10 CPs are used for its parameterization. A representation of the grid is provided in figure C.1.

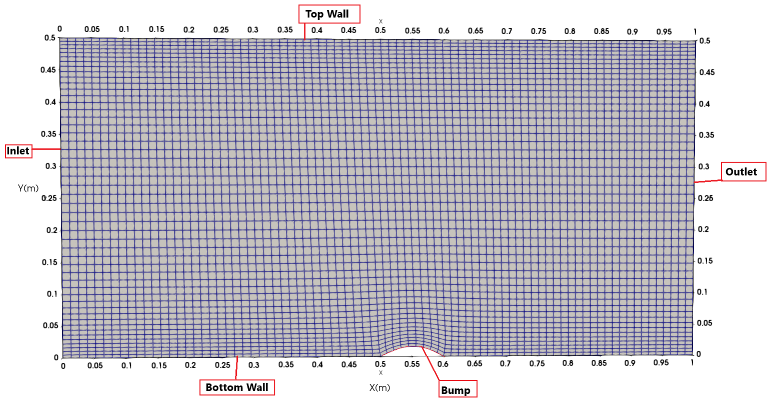

Figure C.1: *Grid of the application for PE method examination.*

Boundary conditions and flow data

Boundary conditions are constant velocity inlet and constant pressure outlet. The flow is laminar with a Reynolds number $R_e = 40$, inlet velocity $U_{in} = 0.48 m/s$, kinematic viscosity $\nu = 6 \times 10^{-3} m^2/s$. The top wall and the bottom wall are no-slip walls with Neumann condition on the pressure for all the patches except from the outlet. The adjoint velocity is set to zero along every patch of the domain and adjoint pressure boundary conditions are the same as those of the primal problem.

PE Computation

In this application, PE is computed for two cases that in order to determine whether PE equals to 1. Case 1 uses all the surface nodes of the bump(including the first and last) and all the CPs of the parameterization, whereas in Case 2 the boundary nodes and the first and last CPs are confined. Both cases utilize the same number of CPs and nodes (10 and 8 respectively), thus, are expected to provide PE values that are practically equal to 1. Table C.1 exhibits the results of the two cases. It can be seen that the PE values of both cases are very close to 1, where their minor errors are probably due to machine accuracy errors during the PE Terms computation. To conclude, the theory of PE is compliant with the developed evaluation tools since the optimization potential of CAD parameterizations when it is as rich as the nodal parameterization, has a PE value that in practice equals to 1.

Case ID	CPs No	Nodes No	PE
Case 1	10	10	0.9969
Case 2	8	8	0.9751

Table C.1: *Comparison of PE values of Cases 1 & 2.*

Bibliography

[1] Γιαννάκογλου, Κ.Χ.: *Μέθοδοι Βελτιστοποίησης στην Αεροδυναμική.* ΜΠΥΡ & Β, 2006.

[2] *Test case 3: Tu berlin turbolab stator.* `https://www.aboutflow.sems.qmul.ac.uk/events/munich2016/benchmark/testcase3/#`.

[3] Robinson, T.T., Armstrong, C.G., and Chua, H.S.: *Determining the parametric effectiveness of a CAD model.* Engineering with Computers, 29(1):111–126, 2013.

[4] Agarwal, D., Kapellos, C., Robinson, T.T., and Armstrong, C.G.: *Using parametric effectiveness for efficient cad-based adjoint optimization.* Computer-Aided Design and Applications, 16(4):703–719, 2019.

[5] Γιαννάκογλου, Κ.Χ.: *Συνεκτικές Ροές στις Στροβιλομηχανές.* Εργαστήριο Θερμικών Στροβιλομηχανών ΕΜΠ, 1997.

[6] Τσαγγάρης, Σ.: *Μηχανική των Πευστών θεωρία και Ασκήσεις.* Εκδόσεις Τσότρας, Αθήνα, δεύτερη έκδοση, 2016.

[7] Παπουτσής-Κιαχαγιάς, Ε.: *Συζυγείς μέθοδοι χαμηλού υπολογιστικού κόστους για τυρβώδεις ροές, στην αεροδυναμική βελτιστοποίηση.* Διδακτορική διατριβή, Εργαστήριο Θερμικών Στροβιλομηχανών, Ε.Μ.Π., Αθήνα, 2013.

[8] Mukallet, F., Mangani, L., and Darwish, M.: *The Finite Volume Method in Computational Fluid Dynamics. An Advanced Introduction with OpenFOAM and Matlab.* Springer International Publishing Switzerland 2016, 2015.

[9] Versteeg, H. K. and Malalasekera, W.: *An introduction to computational fluid dynamics. The finite volume method.* Addison–Wesley, 1996.

[10] Giannakoglou, K.C., Papoutsis-Kiachagias, E.M., and Gkaragkounis, K.T.: *adjointOptimizationFoam, OpenFOAM-based optimization tool.* 2020.

[11] *OpenFOAM, webpage.* `https://www.openfoam.com/`.

[12] Spalart, P. and Allmaras, S.: *A one-equation turbulence model for aerodynamic flows.* AIAA Paper 1992-439, 30th Aerospace Sciences Meeting and Exhibit, Reno, Nevada, USA, January 6–9 1992.

[13] Spalding, D. B.: *A single formula for the law of the wall.* Journal of Applied Mechanics, 28:455–457, 1961.

[14] Γιαννάκογλου, Κ.Χ., Αναγνωστόπουλος, Ι., και Μπεργελές, Γ.: *Αριθμητική Ανάλυση για Μηχανικούς*. Πανεπιστημιακές εκδόσεις ΕΜΠ, τρίτη έκδοση, 2003.

[15] OpenCFDLimited: *OpenFOAM The OpenSource CFD Toolbox, User Guide*. v2112 edition, 2021.

Εθνικό Μετσόβιο Πολυτεχνείο
Σχολή Μηχανολόγων Μηχανικών
Τομέας Ρευστών
Εργαστήριο Θερμικών Στροβιλομηχανών
Μονάδα Παράλληλης Υπολογιστικής Ρευστοδυναμικής
& Βελτιστοποίησης

Η Παραμετρική Αποδοτικότητα και ο Ρόλος της στην Αεροδυναμική Βελτιστοποίηση Μορφής

Εκτενής Περίληψη Διπλωματικής Εργασίας
Κλεάνθης Κλεάνθους

Επιβλέπων: Κυριάκος Χ. Γιαννάκογλου, Καθηγητής ΕΜΠ

Αθήνα, Φεβρουάριος 2023

Εισαγωγή

Η βελτιστοποίηση μορφής σε εφαρμογές εσωτερικής και εξωτερικής αεροδυναμικής, με τη χρήση μοντέλων CAD (CAD-parameterization), οι παράμετροι των οποίων αποτελούν τις μεταβλητές σχεδιασμού $\vec{b} \in \mathbb{R}^n$, απαντάται συχνά σε βιομηχανικές εφαρμογές, έναντι της ελεύθερης μετακίνησης των κόμβων της γεωμετρίας (NODAL parameterization). Οι CAD παραμετροποιήσεις που χρησιμοποιούνται στην παρούσα εργασία είναι καμπύλες NURBS και Bezier-Bernstein αλλά και Volumetric B-splines. Αξίζει να αναφερθεί ότι οι πρώτες δύο μέθοδοι παραμετροποίησης καθορίζουν μόνο τις καμπύλες της γεωμετρίας ενώ η τελευταία καθορίζει, τόσο την εξωτερική γεωμετρία όσο και το πλέγμα (εντός του "morphing box").

Το πλεονέκτημα της χρήσης των παραμετροποιήσεων CAD οφείλεται στο γεγονός ότι οι παραγόμενες γεωμετρίες είναι εξ ορισμού συνεχείς και ομαλές, εν αντιθέσει με την NODAL της οποίας η χρήση απαιτεί την ένταξη αλγορίθμων εξομάλυνσης της γεωμετρίας κατά τη διάρκεια της διαδικασίας βελτιστοποίησης. Παρόλα αυτά, ο ορισμός και η μαθηματική διατύπωση των CAD παραμετροποιήσεων, επάγει περιορισμούς στην πολυπλοκότητα των σχημάτων. Για τον λόγον αυτό εισάγεται η έννοια της 'Παραμετρικής αποτελεσματικότητας' (PE) για την αξιολόγηση της δυναμικής της παραμετροποίησης στη βελτιστοποίηση μορφής.

Σκοπός της διπλωματικής εργασίας είναι ο ορισμός, η ανάπτυξη της μεθόδου υπολογισμού της PE, η μελέτη της συμπεριφορά της και η εξέταση και επικύρωση των αποτελεσμάτων της μέσω διαφόρων εφαρμογών βελτιστοποίησης. Η μελέτη της PE γίνεται μέσω τριών 2Δ εφαρμογών εσωτερικής και εξωτερικής αεροδυναμικής, μιας μεμονωμένης αεροτομής, ενός αγωγού με διαμόρφωση τύπου S και μίας πτερύγωσης αξονικού συμπιεστή([2]).

Το πρωτεύον και Συζυγές Πρόβλημα

Οι εφαρμογές που παρουσιάζονται στην διπλωμτική εργασια αφορούν 2Δ ασυμπίεστη ροή. Οι εφαρμογές της μεμονωμένης αεροτομής και του αγωγού προσομοιώνονται ως στρωτές ροές, ενώ η εφαρμογή του συμπιεστή ως τυρβώδης με τη χρήση του μοντέλου τύρβης Spalart-Allmaras.

Οι εξισώσεις που διέπουν το πρωτεύον και συζυγές πρόβλημα παρουσιάζονται ενδεικτικά για τυρβώδεις ροές στο Κεφάλαιο 2 .

Ορισμός της PE

Η PE ορίζεται ως ο λόγος της βελτίωσης της αεροδυναμικής απόδοσης με τη χρήση CAD παραμετροποίησης, προς τη μέγιστη βελτίωση, η οποία μπορεί να επιτευχθεί μεσω της NODAL παραμετροποησης ως:

$$PE = \frac{\Delta J^{CAD}}{\Delta J^{NODAL}}$$

όπου:

J η συνάρτηση κόστους,

ΔJ^{CAD} το αναμενόμενο κέρδος με τη χρήση παραμετροποίησης CAD,

ΔJ^{NODAL} το αναμενόμενο κέρδος με τη χρήση παραμετροποίησης NODAL.

Στη παρούσα εργασία και χωρίς απώλεια της γενικότητας, γίνεται η υπόθεση ότι η βελτιστοποίηση γίνεται με τη μέθοδο της απότομης καθόδου. Επιπλέον, η βελτίωση της συνάρτησης κόστους μπορεί να εκφραστεί με τη χρήση των γραμμικών όρων ενός αναπτύγματος Taylor με αποτέλεσμα τα κέρδη να εκφράζονται ως:

$$\Delta J^{CAD} = \frac{dJ}{d\vec{b}}\Delta\vec{b}, \quad \Delta J^{NODAL} = \frac{dJ}{d\vec{X}_s}\Delta\vec{X}_s \tag{C.1}$$

όπου, $\vec{b}$ είναι το διάνυσμα των μεταβλητών κατάστασης της παραμετροποίησης CAD, $\vec{X}_s$ το διάνυσμα που εμπεριέχει τις συντεταγμένες των κόμβων του σχήματος, $\Delta\vec{b}$ η αλλαγή των μεταβλητών σχεδιασμού μετά από ένα κύκλο βελτιστοποίησης με χρήση παραμετροποίησης CAD και $\Delta\vec{X}_s$ η μετατόπιση των κόμβων της επιφάνειας του σχήματος μετά από ένα κύκλο βελτιστοποίησης με χρήση NODAL παραμετροποίησης.

Οι ποσότητες $\Delta\vec{b}$ & $\Delta\vec{X}_s$, υπολογίζονται μέσω της απότομης καθόδου σε ένα πρόβλημα ελαχιστοποίησης ως:

$$\Delta\vec{b} = -\eta_{CAD}\left(\frac{dJ}{d\vec{b}}\right)^T, \quad \Delta\vec{X}_s = -\eta_{NODAL}\left(\frac{dJ}{d\vec{X}_s}\right)^T$$

οπου, η_i, είναι το βήμα της απότομης καθόδου.

Αξίζει να αναφερθεί ότι η χρήση της μεθόδου απότοτμης καθόδου, δεν σημαίνει απαραίτητα και τη χρήση της στη βελτιστοποίηση, αλλά προσφέρει ένα εύκολο τρόπο ορισμού και υπολογισμού της PE.

Το βήμα της απότομης καθόδου καθορίζεται απο την τιμή των η, οι οποίες διαφέρουν εν γένει μεταξύ τους για τις δύο μεθόδους. Επομένως, εισάγεται η συνθήκη 'δίκαιης σύγκρισης' για την έκφραση του λόγου μεταξύ των δύο. Η συνθήκη αυτή απαιτεί η συνολική μετατόπιση των κόμβων της γεωμετρίας να είναι ίση για τις δύο μεθόδους και εκφράζεται ως:

$$\int_S \eta^2_{NODAL}\left(\frac{dJ}{d\vec{X}_S}\cdot\vec{n}\right)^2_{NODAL} dS = \int_S \eta^2_{CAD}\left(\frac{d\vec{X}_s}{d\vec{b}}\frac{dJ^T}{d\vec{b}}\cdot\vec{n}\right)^2_{CAD} dS \qquad (C.2)$$

όπου $\vec{n}$ το μοναδιαίο διάνυσμα που κατευθύνεται απο το στερεό προς το ρευστό και $\Delta\vec{X}_s^{\,i}$ η συνολική μεταβολή της γεωμετρίας για τις δύο μεθόδους. Η τελική έκφραση της PE μπορεί να γραφτεί ως:

$$PE = \sqrt{\frac{\int_s\left(\frac{dJ}{d\vec{X}_s}\cdot\vec{n}\right)^2_{NODAL} dS}{\int_s\left(\frac{d\vec{X}_s}{d\vec{b}}\frac{dJ}{d\vec{b}}^T\cdot\vec{n}\right)^2_{CAD} dS}\;\frac{\left(\frac{dJ}{d\vec{b}}\right)^2_{CAD}}{\left(\frac{dJ}{d\vec{X}_s}\right)^2_{NODAL}}}$$

Η σχέση υπολογισμού της PE μπορεί να προσαρμοστεί κατάλληλα για τον υπολογισμό της IPE. Η IPE αφορά την τιμή της PE της κάθε μεταβλητής σχεδιασμού και υπολογίζεται ως:

$$IPE_k = \sqrt{\frac{\int_s\left(\frac{dJ}{d\vec{X}_s}\cdot\vec{n}\right)^2_{NODAL} dS}{\int_s\left(\frac{d\vec{X}_s}{db_k}\frac{dJ}{db_k}\right)^2_{CAD} dS}\;\frac{\left(\frac{dJ}{db_k}\right)^2_{CAD}}{\left(\frac{dJ}{d\vec{X}_s}\right)^2_{NODAL}}}$$

όπου το k συμβολίζει την εκάστοτε μεταβλητή σχεδιασμού.

Κατανόηση της PE

Η συμπεριφορά της PE σε σχέση με την εκάστοτε παραμετροποίηση μελετάται μέσω τριών εφαρμογών. Μίας μεμονωμένης αεροτομής, ενός αγωγού με διαμόρφωση S και μίας 2Δ πτερύγωσης συμπιεστή. Η συνάρτηση κόστους για την μεμονωμένη αεροτομή είναι η ελαχιστοποίηση του συντελεστή αεροδυναμικής αντίστασης ενώ για τις υπόλοιπες δύο η ελαχιστοποίηση των απωλειών ολικής πίεσης (βλ. κεφάλαιο 4).

Μελέτες στη Μεμονωμένη Αεροτομή

Για τον σκοπό της μελέτης, επιλέγεται μία συμμετρική αεροτομή χωρίς απώλεια της γενικότητας. Η γεωμετρία της αεροτομής παραμετροποιείται με τη χρήση καμπυλών NURBS με δύο ταυτόσημες καμπύλες για τις πλευρές υπερπίεσης και υποπίεσης. Η παραμετροποίηση βασίζεται σε μία γεωμετρία αναφοράς, όπου η παραμετροποιημένη γεωμετρία είναι ελαφρώς διαφορετική. Η ροή μοντελοποιείται ως ασυμπίεστη με αριθμό $R_e = 1000$ με τη γωνία της επ άπειρον ροής ίση με 2^o. Οι μεταβλητές σχεδιασμού σε κάθε μελέτη είναι οι συντεταγμένες x,y κάθε σημείου ελέγχου εκτός του πρώτου και τελευταίου σημείου ελέγχου της κάθε καμπύλης.

Στην Μελέτη 1, οι τιμές της PE υπολογίζονται για την ίδια γεωμετρία η οποία παραμετροποιείται με: 14-24 σημεία ελέγχου. Ο αριθμός τους αυξάνει με την χρήση εμπλόυτισμού διατηρώντας το σχήμα της αεροτομής αμετάβλητο. Η Μελέτη 2 είναι ίδια με την Μελέτη 1, με τη διαφορά ότι το πρωτεύον και συζυγές πεδίο υπολογίζονται στην αεροτομή αναφοράς. Η αξία της συγκεκριμένης μελέτης έγκειται στην αποφυγή των μεθόδων πραραμόρφωσης του πλέγματος, ώστε να συμπίπτει με την παραμετροποιημένη αεροτομή. Στην 3η Μελέτη, κάθε αεροτομή παραμετροποιείται με διαφορετική προσαρμογή (best-fit) για 12-24 σημεία ελέγχου, με αποτέλεσμα όλες οι αεροτομές να διαφέρουν ελαφρώς. Οι τιμές IPE όλων των παραμέτρων σχεδιασμού για τυχαίες παραμετροποιήσεις υπολογίζονται και παρουσιάζονται στη Μελέτη 4, για τη διερεύνηση της σημαντικότητας κάθε παραμέτρου.

Τα αποτελέσματα των πρώτων τριών μελετών παρουσιάζονται στο διάγραμμα 2. Και στις τρείς μελέτες, οι τιμές της PE αυξάνουν μονότονα και τείνουν ασυμπτωτικά σε μία μέγστη τιμή της PE. Με μπλέ χρώμα παρουσιάζεται η καμπύλη της Μελέτης 1, με πράσινο της Μελέτης 2 και με κόκκινο της Μελέτης 3. Αξίζει να σημειωθεί ότι στο μεγαλύτερο τους μέρος, οι καμπύλες των δύο τελευταίων σχεδόν συμπίπτουν.

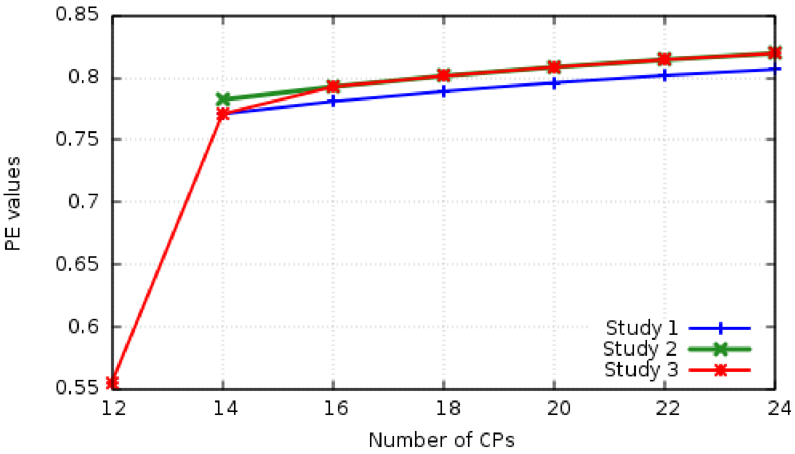

Σχήμα: 2: *Μεμονωμένη αεροτομή: PE ως προς τον αριθμό των σημείων ελέγχου για τις Μελέτες 1 έως 3.*

Τα αποτελέσματα της 4ης μελέτης παρουσιάζονται στα διαγράμματα 3α και 3β για τις παραμετροποιήσεις με χρήση 16 και 20 σημείων ελέγχου της Μελέτης 3. Οι τιμές της IPE των y συντεταγμένων είναι μεγαλύτερες από τις αντίστοιχες των x κατά μία τάξη μεγέθους. Επομένως, η παραμόρφωση της γεωμετρίας κατά το πάχος της αεροτομής έχει μεγαλύτερη επίδραση στην μείωση της συνάρτησης στόχου σε σχέση με την οριζόντια μετατόπιση των σημείων ελέγχου.

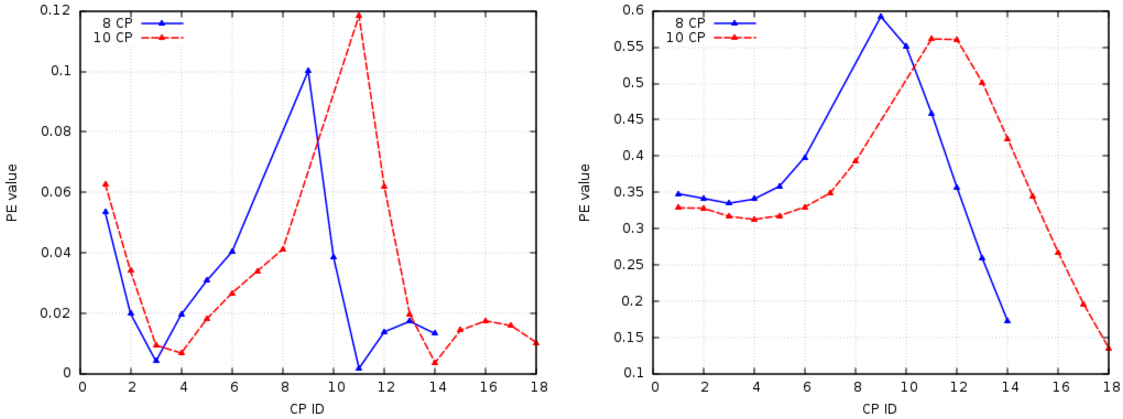

(a) *Τιμές IPE για τις x συντεταγμένες* **(b)** *Τιμές IPE για τις y συντεταγμένες*

Σχήμα: 3: *Μεμονωμένη αεροτομή: Αποτελέσματα Μελέτης 4. Τιμές IPE για τις x,y συντεταγμένες των παραμετροποιήσεων 16 και 20 σημείων ελέγχου της Μελέτης 3.*

Μελέτες στον αγωγό με διαμόρφωση S

Για την παραμετροποίηση της γεωμετρίας του αγωγού χρησιμοποιούνται δύο μέθοδοι παραμετροποίησης, οι καμπύλες Bezier-Bernstein και volumetric B-splines. Η ροή προσομοιώνεται ως στρωτή με αριθμό $R_e = 1000$. Οι συντεταγμένες x,y αποτελούν τις μεταβλητές σχεδιασμού κάθε μελέτης. Στις παραμετροποιήσεις με τη χρήση Bezier-Bernstein, τα πρώτα και τελευταία σημεία ελέγχου κάθε καμπύλης του αγωγού θεωρούνται σταθερά. Οι μεταβλητές σχεδιασμού ισούνται με $N_b = 2N_{CP} - 8$, όπου N_{CP} είναι ο συνολικός αριθμός των σημείων ελέγχου της κάθε παραμετροποίησης. Όταν ο αγωγός παραμετροποιείται με volumetric B-splines, τα σημεία ελέγχου που ανήκουν στις πρώτες και τελευταίες δύο στήλες του πλέγματος ελέγχου κατά τη x κατεύθυνση θεωρούνται σταθερά. Ο αριθμός των μεταβλητών σχεδιασμού ισούται με: $N_b = 2N_y(N_x - 4)$, όπου N_x και N_y είναι το πλήθος των σημείων ελέγχου που βρίσκονται σε κάθε στήλη και κάθε γραμμή του πλέγματος ελέγχου αντίστοιχα (control grid).

Στις Μελέτες 1 και 2 οι γεωμετρίες παραμετροποιούνται με τη χρήση καμπυλών Bezier-Bernstein. Στην Μελέτη 1, ο αριθμός των σημείων ελέγχου αυξάνει μέσω μμύ, ενώ στην Μελέτη 2 οι αγωγοί είναι ελαφρώς διαφορετικοί μεταξύ τους καθώς παραμετροποιούνται με διαφορετική προσαρμογή. Στις Μελέτες 3 και 4 ο αγωγός παραμετροποιείται με τη χρήση volumetric B-splines, όπου ο αριθμός των σημείων ελέγχου αυξάνει κατά τη x και y κατεύθυνση αντίστοιχα. Τα αποτελέσματα των προηγούμενων παρουσιάζονται στα διαγράμματα 4α και 4β.

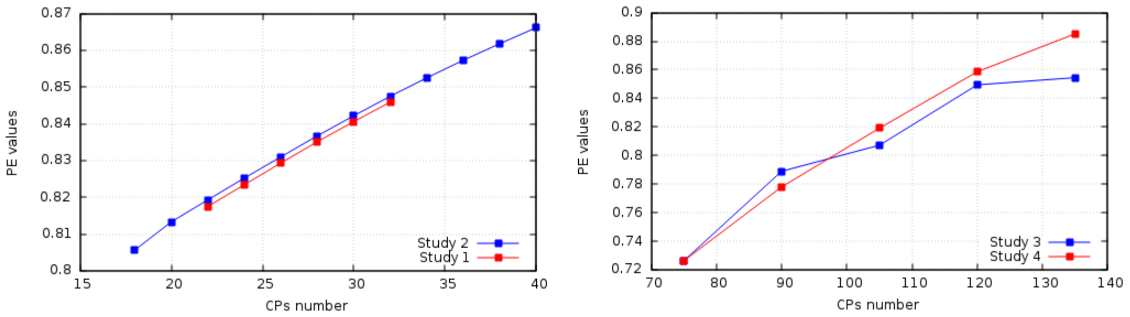

(a) *Αποτελέσματα Μελετών 1 και 2. Με κόκκινο χρώμα παρουσιάζεται η καμπύλη της Μελέτης 1 ενώ με μπλέ της Μελέτης 2.*

(b) *Αποτελέσματα Μελετών 3 και 4. Με μπλέ χρώμα παρουσιάζεται η καμπύλη της Μελέτης 3 ενώ με κόκκινο της Μελέτης 4.*

Σχήμα: 4: *Αγωγός με διαμόρφωση S : PE για διαφορετικό αριθμό σημείων ελέγχου για τις Μελέτες 1 με 4.*

Μελέτες στη 2Δ πτερύγωση συμπιεστή

Η ροή μοντελοποιείται ως τυρβώδης με αριθμό $R_e \approx 7.17 \times 10^5$ υπό γωνία -42^o. Για την προσομοίωση χρησιμοποιείται το μοντέλο τύρβης μίας ΜΔΕ, Spalart-Allmaras. Η αεροτομή παραμετροποιείται με καμπύλες NURBS. Η συμπεριφορά της PE μελετάται μέσω τεσσάρων παραμετρικών μελετών για διαφορετικό αριθμό σημείων ελέγχου και βαθμού πολυωνύμων βάσης. Στις Μελέτες 1 και 2, η αεροτομή παραμετροποιείται με 5 περισσοτέρα σημεία ελέγχου στην πλευρά υπερπίεσης και υπο πίεσης αντίστοιχα. Ο βαθμός των πολυωνύμων βάσης και στις δύο μελέτες τίθεται ίσος με 3 λόγω της πολυπλοκότητας της γεωμετρίας. Στις Μελέτες 3 και 4, η γεωμετρία παραμετροποιείται με ίδιο αριθμό σημείων ελέγχου σε κάθε πλευρά της αεροτομής. Ο βαθμός των πολυωνύμων βάσης της Μελέτης 3 είναι ίσως με 3, ενώ της Μελέτης 4 ίσος με 5. Τα αποτελέσματα των Μελετών παρουσιάζονται στα διαγράμματα 5α και 5β. Η τιμή της PE αυξάνει μονότονα με την αύξηση των παραμέτρων. Όμως στην Μελέτη 4, όπου αυξάνεται η πολυπλοκότητα παρατηρείται ότι η PE παρουσιάζει ελαφρά μείωση και σύγκλιση σε μία τιμή κοντά στο 0.6.

Βελτιστοποίηση της μεμονωμένης αεροτομής

Αρχικά, η αεροτομή βελτιστοποιείται με την χρήση τριών παραμετροποιήσεων. Στην 1η Περίπτωση παραμετροποιείται με 14 σημεία ελέγχου ενώ στις υπόλοιπες δύο με 20. Στην Περίπτωση 2 η αεροτομή παράγεται με διαφορετική προσαρμογή (ελαφρώς διαφορετική από τις υπόλοιπες δύο) ενώ στην 3η Περίπτωση μέσω μμύ (απο τα 14 σημεία ελέγχου). Επομένως, οι αεροτομές των Περιπτώσεων 1 και 3 είναι ακριβώς οι ίδιες. Οι περιορισμοί που επιβάλλονται είναι η διατήρηση σταθερών των πρώτων και τελευταίων δύο σημείων ελέγχου της κάθε πλευράς για επίτευξη συνέχειας σχήματος και παραγώγου. Επίσης, η μείωση της τιμής του συντελεστή άνωσης και της

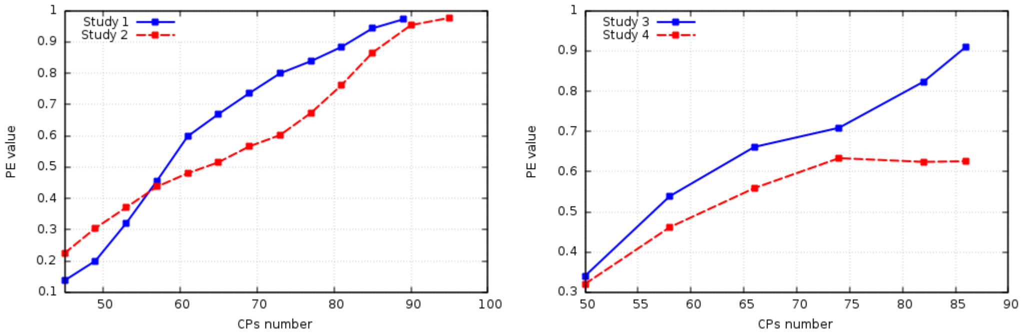

(a) *Αποτελέσματα Μελετών 1 και 2. Με μπλέ χρώμα παρουσιάζεται η καμπύλη της Μελέτης 1 ενώ με κόκκινο της Μελέτης 2.*

(b) *Αποτελέσματα Μελετών 3 και 4. Με μπλέ χρώμα παρουσιάζεται η καμπύλη της Μελέτης 3 ενώ με κόκκινο της Μελέτης 4.*

Σχήμα: 5: *2Δ πτερύγωση συμπιεστή : PE για διαφορετικό αριθμό σημείων ελέγχου και βαθμών πολυωνύμων βάσης για τις Μελέτες 1 με 4.*

επιφάνειας της αεροτομής διατηρούνται σε προκαθορισμένα πλαίσια. Τέλος, η τιμή του συντελεστή ροπής απαιτείται να είναι μηδενική. Τα αποτελέσματα καθώς και η πορεία της PE παρουσιάζονται στο Σχήμα 6. Με πράσινο χρώμα παρουσιάζονται τα αποτελέσματα της Περίπτωσης 1, με κόκκινο της Περίπτωσης 2 και με μπλε της Περίπτωσης 3.

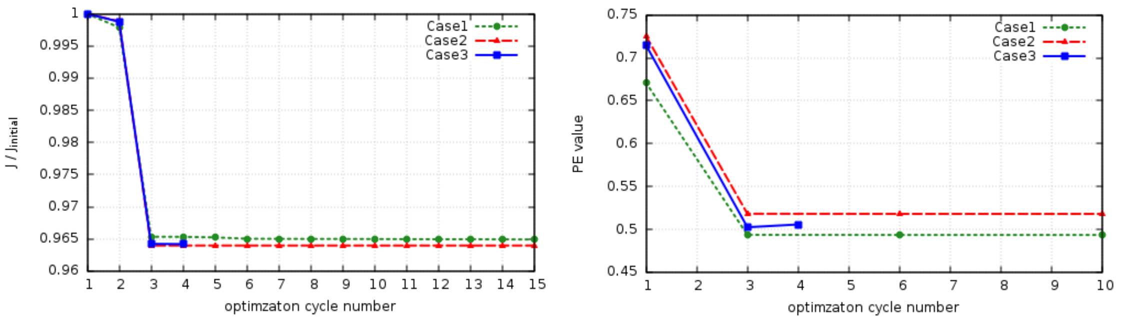

(a) *Αποτελέσματα βελτιστοποίησης.*

(b) *Η εξέλιξη της PE κατα τη βελτιστοποίηση.*

Σχήμα: 6: *Μεμονωμένη αεροτομή : Πορεία βελτιστοποίησης της μεμονωμένης αεροτομής και εξέλιξη της PE κατα την βελτιστοποίηση.*

Επιπλέον, για τις Περιπτώσεις 1 και 2, η αεροτομή βελτιστοποιείται με τη χρήση των 5 σημαντικότερων παραμέτρων σχεδιασμού. Η επιλογή των παραμέτρων που συμμετέχουν στη βελτιστοποίηση γίνεται με τη χρήση της εκάστοτε τιμής των IPE. Τα αποτελέσματα παρουσιάζονται στο Σχήμα 7. Με μπλε και κόκκινο χρώμα παρουσιάζονται τα αποτελέσματα για τις 5 σημαντικότερες παραμέτρους των Περιπτώσεων 1 και 2 αντίστοιχα. Με πράσινο και ροζ παρουσιάζεται η πορεία βελτιστοποίησης των Περιπτώσεων 1 και 2 με την χρήση όλων των παραμέτρων. Η σημαντικότητα των 5 επιλεγμένων παραμέτρων της Περίπτωσης 1 είναι μεγαλύτερη από των αντίστοιχων παραμέτρων της Περίπτωσης 2. Επίσης, στην Περίπτωση 1, οι πιο σημαντικές παράμετροι δίνουν πρακτικά ίδιο αποτέλεσμα σε σχέση με την βελτιστοποίηση όπου χρησιμοποιούνται όλες οι παραμέτροι σε αντίθεση με την Περίπτωση 2 που η τελική τιμή της συνάρτησης κόστους για τις 5 παραμέτρους έχει διαφορά περίπου 0.5% συγκριτικά με την περίπτωση οπου χρησιμοποιούνται όλες οι παράμετροι.

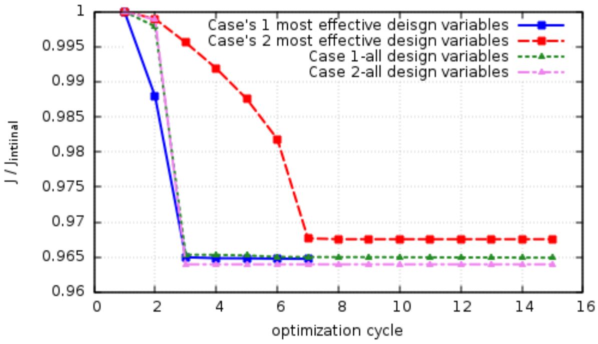

Σχήμα: 7: *Μεμονωμένη αεροτομή: Αποτελέσματα βελτιστοποίησης με χρήση των σημαντικότερων παραμέτρων στις Περιπτώσεις 1 και 2.*

Βελτιστοποίηση του αγωγού με διαμόρφωση S

Κατα τη βελτιστοποίηση του αγωγού, με παραμετροποίηση Bezier, τα πρώτα και τελευταία δύο σημεία ελέγχου κάθε καμπύλης διατηρούνται σταθερά. Αντίστοιχα το ίδιο συμβαίνει με τις πρώτες και τελευταίες δύο στήλες σημείων ελέγχου κατα x όταν ο αγωγός παραμετροποιείται με volumetric B-splines. Η επιβολή των περιορισμών γίνεται για την επίτευξη συνέχειας σχήματος και πρώτης παραγώγου στην αρχή και στο τέλος του τμήματος με τη διαμόρφωση S.

Εφαρμόζεται μια παραμετρική μελέτη κατά την οποία ο αγωγός βελτιστοποιείται για διαφορετικό αριθμό σημείων ελέγχου της παραμετροποίησης Bezier όπου ο κάθε αριθμός σημείων ελέγχου συνδέεται με διαφορετική τιμή της PE. Όπως φαίνεται στο Σχήμα 8, όσο η τιμή της PE αυξάνει, η τελική τιμή της συνάρτησης κόστους λαμβάνει μικρότερες τιμές, επιβεβαιώνοντας ότι η PE μπορεί να χρησιμοποιηθεί για τη συγκρίση παραμετροποιήσεων ως προς τη δυναμική τους στη βελτιστοποίηση.

Επιπρόσθετα, για τη σύγκριση διαφορετικών μεθόδων παραμετροποίησης, ο αγωγός βελτιστοποιείται με Bezier (Περιπτώσεις 1 και 2) και volumetric B-splines (Περιπτώσεις 3 και 4). Για κάθε μέθοδο εκτελούνται δύο βελτιστοποιήσεις, με διαφορετικό αριθμό παραμέτρων σχεδιασμού (24, 64, 25 και 10 αντίστοιχα) που συνδέεται και με διαφορετική τιμή της PE. Τα αποτελέσματα καθώς και η εξέλιξη της PE παρουσιάζονται στα διαγράμματα 9α και 9β. Οι Περιπτώσεις 1 έως 4 παρατίθενται με μπλε, κόκκινο, πράσινο και

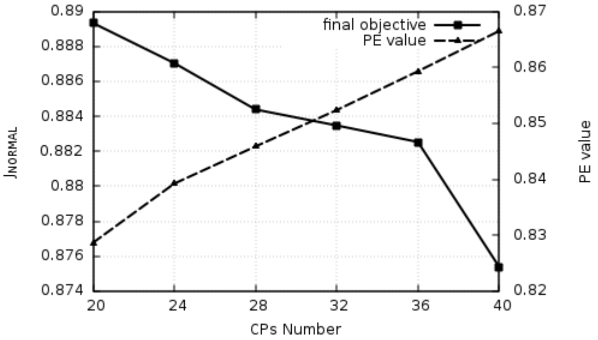

Σχήμα: 8: *Αγωγός με διαμόρφωση S: Παραμετρική μελέτη για τη συσχέτιση της PE με τις λύσεις της βελτιστοποίησησης*

.

μαύρο χρώμα αντίστοιχα. Όσο μεγαλύτερη η τιμή της PE, ανεξαρτήτως της μεθόδου παραμετροποίησης της συγκεκριμένης εφαρμογής η τελική συνάρτηση κόστους λαμβάνει μικρότερες τιμές.

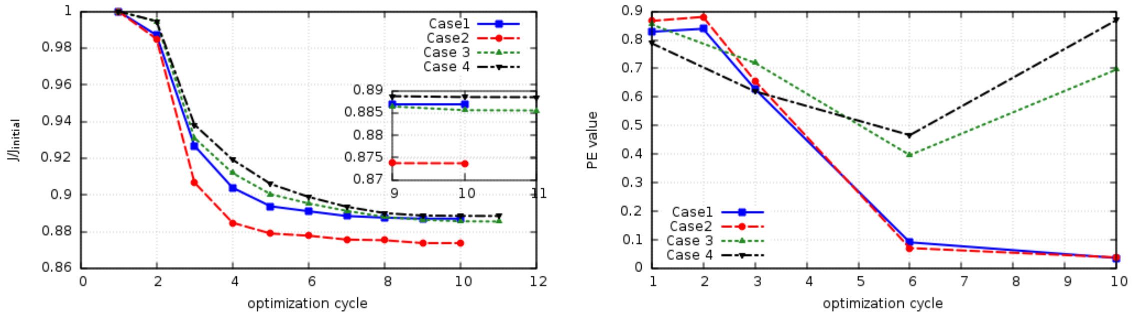

(a) *Πορεία της βελτιστοποίησης.*

(b) *Εξέλιξη της PE*

Σχήμα: 9: *Αγωγός τύπου S : Πορεία βελτιστοποίησης για διαφορετικές μεθόδους παραμετροποίησης και εξέλιξη της PE κατά την βελτιστοποίηση.*

Τέλος, παρουσιάζεται η βελτιστοποίηση της πτερύγωσης του συμπιεστή με χρήση 61 (PE=0.0583) και 69 (PE=0.1268) σημείων ελέγχου αντίστοιχα. Η βελτιστοποίηση γίνεται υπό τον περιορισμό της διατήρησης της στροφής της ροής (η οποία συσχετίζεται με την αύξηση της στατικής πίεσης) καθώς και της αρχικής επιφάνειας του πτερυγίου. Ο πρώτος περιορισμός ικανοποιείται με την διατήρηση σταθερών σημείων ελέγχου γύρω από τις περιοχές της ακμής προσβολής και εκφυγής. Λόγω της διατήρησης αρκετών σημείων ελέγχου σταθερών, στα οποία αντιστοιχούν μεγάλες παράγωγοι ευαισθησίας, οι τιμές της PE είναι αρκετά μικρές στις δύο περιπτώσεις, το οποίο αντανακλάται και στα αποτελέσματα της βελτιστοποίησης. Τα αποτελέσματα και η εξέλιξη της PE παρουσιάζονται στα διαγράμματα 10α και 10β.

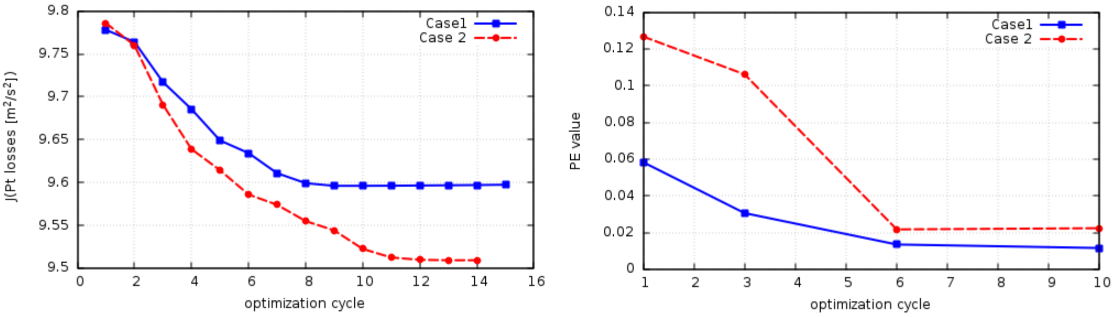

(a) *Πορεία της βελτιστοποίησης.* (b) *Εξέλιξη της PE*

Σχήμα: 10: *2Δ Πτερύγωση συμπιεστή : Πορεία βελτιστοποίησης για διαφορετικές μεθόδους παραμετροποίησης και εξέλιξη της PE κατά την βελτιστοποίηση.*

Συμπεράσματα

Αρχικά παρατηρήθηκε ότι η τιμή της PE αυξάνει όσο η παραμετροποίηση γίνεται πλουσιότερη και συγκλίνει ασυμπτωτικά στη μέγιστη τιμή. Επίσης, όσο η τιμή της PE αυξάνει, οι τελικές τιμές της συνάρτησης κόστους λαμβάνουν μικρότερες τιμές. Όπως φάνηκε και στις τρείς εφαρμογές, οι τιμές της PE για τις παραμετροποιήσεις με Bezier-Bernstein και NURBS μειώνονται συνεχώς όσο προχωρά η βελτιστοποίηση, σε αντίθεση με τις volumetric B-splines οπου η PE δεν ακολουθεί συγκεκριμένη κατανομή. Έγινε επίσης αντιληπτό ότι, η επιλογή των παραμέτρων με τις μεγαλύτερες τιμές IPE από μία υπάρχουσα παραμετροποίηση, δύναται να δώσει πολύ κοντινά αποτελέσματα κατά την βελτιστοποίηση σε σχέση με την περίπτωση που χρησιμοποιούνται όλες οι παραμέτροι ως μεταβλητές σχεδιασμού. Παρόλα αυτά για την επιλογή των παραμέτρων πρέπει να λαμβάνεται υπόψιν το ποσοστό του άθροισματος των επιμέρους IPE των επιλεγμένων παραμέτρων σε σχέση με το άθροισμα των IPE όλων των παραμέτρων. Τέλος, παρατηρήθηκε ότι, η PE μπορεί να χρησιμοποιηθεί και για τη σύγκριση μεταξύ δύο μεθόδων παραμετροποίησης για την επιλογή αυτής με τη μεγαλύτερη δυναμική κατα τη βελτιστοποίηση η οποία θα δώσει και καλύτερα αποτελέσματα.

Επομένως, για τις μεθόδους παραμετροποίησης που χρησιμοποιήθηκαν, η PE μπορεί να βοηθήσει τους σχεδιαστές να λάβουν κατάλληλες αποφάσεις για την επιλογή τόσο της μεθόδου παραμετροποίησης, όσο και του αριθμού των παραμέτρων για την επίτευξη χαμηλότερων τιμών της συνάρτησης κόστους στην βελτιστοποίηση.

Μελλοντική δουλειά

Τα αποτελέσματα και συμπεράσματα της εργασίας θα μπορούσαν να χρησιμοποιηθούν για την ανάπτυξη κάποιων διαδικασιών στη διάρκεια του βρόχου βελτιστοποίησης. Η μέθοδος θα μπορούσε να αποφασίζει σε ποιους κύκλους η PE πρέπει να υπολογισθεί ξανά και πως η πληροφορία που δίνει θα μπορούσε να βελτιώσει δυναμικά την βελτιστοποίηση. Επιπλέον, θα ήταν εξαιρετικά ενδιαφέρον, εάν η PE μπορούσε να προσαρμοστεί για μείωση των παραμέτρων σχεδιασμού στους EA, όπου το κόστος είναι ανάλογο του αριθμού των μεταβλητών σχεδιασμού. Ως αποτέλεσμα, η μείωση του πλήθους των πιθανών συνδυασμών τους θα μπορούσε να μειώσει τον αριθμών των CFD αξιολογήσεων μέχρι την εύρεση της βέλτιστης λύσης μειώνοντας σημαντικά το κόστος της βελτιστοποίησης.